2019-08-01

Characterization of Dislocation - Grain Boundary Interactions Through Electron Backscatter Diffraction

Landon Thomas Hansen
Brigham Young University

Characterization of Dislocation – Grain Boundary Interactions

Through Electron Backscatter Diffraction

Landon Thomas Hansen

A dissertation submitted to the faculty of
Brigham Young University
in partial fulfillment of the requirements for the degree of

Doctor of Philosophy

David T. Fullwood, Chair
Eric R. Homer
Oliver K. Johnson
Michael P. Miles
Tracy W. Nelson

Department of Mechanical Engineering

Brigham Young University

ABSTRACT

Characterization of Dislocation-Grain Boundary Interactions
Through Electron Backscatter Diffraction

Landon Thomas Hansen
Department of Mechanical Engineering, BYU
Doctor of Philosophy

Further understanding of dislocation-GB interactions is critical to increasing the performance of polycrystalline metals. The research contained within this dissertation aims to further dislocation-GB interaction understanding through three research studies. First, the effect of noise in EBSPs on GND calculations was evaluated in order to improve dislocation characterization via HR-EBSD. Second, the evolution of GNDs and their effects on back stress was studied through experimental and computational methods applied to tantalum oligo specimens. Third, statistical analysis was used to evaluate grain parameters and current GB transmission parameters on their correlation with dislocation accumulation.

Keywords: EBSD, HR-EBSD, GND, dislocation, grain boundaries, tantalum, transmission factor

ACKNOWLEDGEMENTS

I would like to primarily acknowledge the many hours of assistance from my advisor David Fullwood. His role in my graduate work has been paramount. He has been extremely patient and insightful in helping me improve my work and myself throughout graduate school. I also thank my committee for their insights and guidance in helping me develop conclusion for the last bit of this dissertation. Jay Carroll was a significant asset to this research and me, and I want to thank him for getting me loads of data and setting me up with the opportunity to spend some time at Sandia National Laboratories. My wife, Mary, deserves some thanks and a shout out as well. She has been super awesome in taking care of things at home so that I can spend the time needed to work on research. Finally, I would like to acknowledge the hand of God throughout my life. His many mercies and miracles have heavily dotted my time in graduate school, including the miracle to defend and submit this dissertation against impossible deadlines. This research was supported by funding from the U.S. Department of Energy (DOE), Office of Science, Basic Energy Sciences (BES), under award number DE-SC-0012587.

TABLE OF CONTENTS

LIST OF TABLES

LIST OF FIGURES

1 INTRODUCTION

Grain boundary (GB) strengthening, due to the interaction between dislocations and GBs, is an important strengthening mechanism in metals [1]. During deformation, GBs impede dislocation movement thus making deformation more difficult. This manifests in the important relationship of the Hall-Petch effect, an increase in yield strength with a decrease in grain size [2,3]. Understanding of dislocation-GB interactions can lead to increased strength and ductility by introducing new strengthening techniques similar to ones currently used in material design, e.g. solid solution strengthening, precipitation hardening, transformation hardening, and crystallographic texture modification. Interest in this topic has led to decades of research [4–8] and it continues to be a major topic of interest to this day [9–13].

Although dislocation-GB interactions have been heavily studied, there is still much that remains unknown to the scientific community. One reason these interactions are so difficult to fully characterize is the immense number of possible GB configurations; Adams calculates that there are ~133,000,000 grain boundary types assuming 1° angular resolution [14]. Due to the enormity and complexity of the knowledge base required to fully describe dislocation-GB interactions, this research aims to tackle only a few areas of research with will contribute its understanding. Three studies are discussed in this dissertation which focus on 1) the technological advances in detecting dislocations vis high angular resolution electron backscatter diffraction (HR-EBSD), 2) the evolution of GNDs and their effects on back stress through experimental and

computational methods, and 3) the statistical analysis of experimental results to characterize dislocation evolution throughout grains, GBs, and triple junctions (TJs).

In recent years, data collection rates for EBSD have exceeded 2000 points/second [15], allowing it to scan thousands of GBs in a relatively short period of time. Although high EBSD data collection rates are available, there is a significant trade-off between the amount of data that can be collected and the reliability of the GND predictions via HR-EBSD. The decrease in HR-EBSD reliability when data is collected quickly is associated with the increase in noise that occurs when SEM settings are optimized for speed. Noise can be particularly prevalent near GBs where the lattice structure is less regular and there is potential for the electron beam to interact with both sides of the GB. The relationship between HR-EBSD reliability and noise is complicated and not fully understood [16–19]. The first study in this dissertation expands the understanding of this relationship between noise and HR-EBSD results, enabling researchers to select SEM settings for efficient and reliable dislocation-GB experiments using HR-EBSD.

Knowing the effects of SEM settings on HR-EBSD results, studies relying on HR-EBSD analysis can be used to characterize GNDs, and the results can be accurately interpreted. GNDs are stored in deformation gradients — typically at barriers such as GBs — and the stresses they produce combine in an additive nature to produce elastic long-range stresses, known as back stresses. These backstresses cause strain hardening by opposing dislocation slip. Ashby demonstrated that the GNDs which produce this backstress are required in order to maintain compatibility at GBs. Furthermore, many have proposed that GNDs also occur at GBs due to their inability to transmit across the interface, and the difficulty in which a dislocation can transmit from one slip system to another slip system in a neighboring grain can be quantified via a transmission factor. The second study in this dissertation uncovers a correlation between GB transmission

factors and the accumulation of GNDs at the GB, and it describes ways that GND maps help to visualize backstress. Furthermore, backstress is quantified and the role of GNDs in producing it is explored a recently developed crystal plasticity finite element method (CP-FEM) known as the SuperDislocation (SD) model.

While the second study in this dissertation analyzes several GB transmissivity factors and their correlation with GNDs at 61 GBs, the third study greatly expands on the second studies work by analyzing the correlations between GNDs and many microstructure features of several thousand grains, GBs, and TJs. By using statistical methods to analyze large amounts of crystallographic data obtained via EBSD, relationships between the geometric properties of the microstructure and GNDs can be uncovered that would not otherwise be feasible via human observation alone. Critical microstructures parameters, including GB transmission factors, are found to have a strong effect on the accumulation of GNDs and the resulting macroscopic properties of the material. These three studies mentioned are presented in chapters 2 through 4, and are followed by a conclusion.

1.1 GND Density Calculations Using EBSD Data

Electron backscatter diffraction (EBSD), and in particular high angular resolution EBSD (HR-EBSD) also known as cross-correlation EBSD (CC-EBSD), is a well suited experimental method for investigating dislocations. The advent of HR-EBSD has transformed access to high integrity strain gradients [20–22] and related geometrically necessary dislocation (GND) fields [23–25]. HR-EBSD is capable of 20 nm spatial resolution and 0.006 degrees angular resolution [17,26–28], making it useful for investigating dislocation structures near individual GBs with very fine resolution. Traditional EBSD has the same special resolution, but can only determine

misorientation within 0.5 degrees [29]. BYU's scanning electron microscopy (SEM) facilities and vast knowledge of EBSD and HR-EBSD make it an ideal tool for characterizing dislocations.

The presence of GNDs in a crystalline sample leads to elastic strain gradients (generally assumed to be dominated by lattice orientation gradients) in the local lattice. This is most easily visualized by imagining a series of edge dislocations that are stacked above one another, for example, in a low angle grain boundary (GB); the net effect is a rotation of the lattice, required to accommodate the extra planes of atoms. The fundamental theorems of continuum dislocation theory formally relate the gradients in the lattice strain/rotation to the GND content. A mathematically convenient way to capture the GND density, ρ_{GND}, on the various slip systems, m, via the Nye tensor, α, which is defined as [30,31]:

$$\alpha_{ij} = \sum_m \rho_{GND}^m \, b_i^m v_j^m \tag{1-1}$$

where $\boldsymbol{b}$ is the Burgers vector, and $\boldsymbol{v}$ is the line vector. The Nye can also be represented in terms of the elastic distortion tensor, $\boldsymbol{\beta^e}$:

$$\alpha_{km} = \nabla \times \boldsymbol{\beta^e} = \epsilon_{jim} \beta_{kj,i}^e \tag{1-2}$$

where ϵ is the permutation tensor and $\nabla \times \boldsymbol{\beta^e}$ is the curl of $\boldsymbol{\beta^e}$. The spatial derivatives of $\boldsymbol{\beta^e}$, indicated by the subscript "$,i$", are therefore the relevant strain gradients that are required from EBSD measurements in order to establish GND content.

Such strain gradients are observed as small variations in the EBSD pattern as the scan position rasters across the sample surface. By considering relative distortions in EBSD patterns between neighboring scan positions, the associated changes in lattice structure can be detected, and the strain gradients recovered. This is the underlying idea behind HR-EBSD. An EBSD pattern

is collected from a given scan point, and a second pattern is taken from a point at a known distance in the desired direction. Regions of interest (ROIs) within the two patterns are compared using convolutions, implemented via fast Fourier transform methods. Subtle distortions in the patterns result in shifts of local features (such as bands and band intersections) that are quantified by the convolution approach. A set of relationships connecting the pattern shifts to the local lattice distortion is solved, resulting in the desired strain gradient in the chosen direction [26]:

$$\boldsymbol{\beta}^{e}_{kj,i}\big|_{\boldsymbol{p}} = \frac{\partial \boldsymbol{\beta}^{e}}{\partial \boldsymbol{x_i}}\Big|_{\boldsymbol{p}} = \frac{\boldsymbol{\beta}^{e}_{\boldsymbol{p}} - \boldsymbol{\beta}^{e}_{\boldsymbol{p}+\Delta \boldsymbol{x_i}}}{L} \tag{1-3}$$

where $\boldsymbol{p}$ is the location of the current scan point, $\Delta \boldsymbol{x_i}$ is a vector between the current scan point and a neighboring scan point in the ith direction, L the distance between scan points, and $\boldsymbol{\beta}^{e}_{\boldsymbol{p}} - \boldsymbol{\beta}^{e}_{\boldsymbol{p}+\Delta \boldsymbol{x_i}}$ is the relative elastic distortion determined by comparing the two patterns from these scan points.

Applying the cross correlation method described in the previous paragraph to equation (1-2), the Nye tensor can be calculated at every point in an EBSD scan. Equation (1-1) can then be rearranged, and the total GND density can be approximated via the L1 norm of the Nye tensor:

$$\rho_{GND} \cong \frac{1}{b}\sum_i \sum_j \left|\alpha_{ij}\right| \tag{1-4}$$

where b is the magnitude of the burgers vector. However, since EBSD scans are typically taken on a 2D surface, the derivatives required in equation (1-2) are only available in the two dimensions of the sample surface, arriving at only three fully determined and 2.5 partially determined components of the 9 Nye tensor terms. This is generally considered to be adequate for a reasonable estimate of the total GND density content via the L1 norm of the tensor [24,28].

GND calculations can also be performed by relying upon the orientations from EBSD collection software instead of relying upon cross-correlation of saved patterns. This method is referred to as "orientation based GND calculations" in this dissertation and was used when saved patterns were unavailable. Due to lower misorientation resolution of standard EBSD compared to HR-EBSD (resolution of 0.5° compared to 0.006° respectively), GND calculations without cross-correlation are expected to be less precise [17,32], and are thus used for qualitative comparisons in this paper. A test by the author showed a 17.2% increase in the standard deviation of the GND content in single-crystal silicon when using orientation based GND calculations compared to HR-EBSD.

Orientation based GND calculations are fully described by Pantleon [33] and a simplified overview is given here. The elastic distortion tensor, $\boldsymbol{\beta^e}$, in equation (1-2) is composed of the lattice rotation tensor, $\boldsymbol{\omega^e}$, and the elastic strain tensor, $\boldsymbol{\varepsilon^e}$, as follows:

$$\boldsymbol{\beta^e} = \boldsymbol{\omega^e} + \boldsymbol{\varepsilon^e} \tag{1-5}$$

By assuming the elastic strain tensor to be negligible compared to the lattice rotation tensor — a common assumption, e.g. [34–36] — we arrive at the following equation:

$$\boldsymbol{\beta^e} = \boldsymbol{\omega^e} + \boldsymbol{\varepsilon^e} \cong \boldsymbol{\omega^e} \tag{1-6}$$

Using the small angle approximation for the lattice rotation tensor and substituting equation (1-6) into equation (1-2), the following equation for estimating the Nye tensor can be obtained:

$$\alpha_{km} \cong \epsilon_{ijm}\omega^e_{ki,j} \tag{1-7}$$

where the two dimensional components of $\boldsymbol{\omega}^{\boldsymbol{e}}$ can be obtained from EBSD orientation data. As before, a reasonable estimate of the GND content can be calculated using the L1 norm of the Nye tensor components and a scaling factor.

1.2 GB Transmission Factors

Several orientation-based slip transmission factors have been proposed over the years which predict the difficulty for a dislocation to transmit from one slip system to another slip system in a neighboring grain [12–18]. In general, orientation-based slip transmission factors are based on the idea that dislocations transmit more easily across the GB to neighboring grains with closely aligned slip systems than those with unaligned slip systems [19]. The following variables (displayed in Figure 1-1) are used to define the several slip transmission factors described in this study: $\boldsymbol{n}$ is the slip plane normal, $\boldsymbol{d}$ is the slip direction, α defines a slip system in the incoming grain, and β defines a slip system in the outgoing grain.

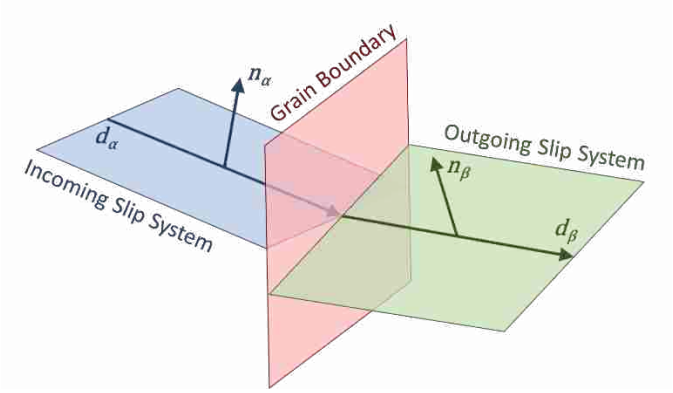

Figure 1-1: Graphical description of the variables used to define the slip transmission factors

Livingston and Chalmers were one of the first to use an orientation-based transmission factor, the N factor [15]. It is based on the slip directions and the slip plane normal of the two active slip systems, and is defined as

$$N_{\alpha\beta} = (\boldsymbol{n}_\alpha \cdot \boldsymbol{n}_\beta)(\boldsymbol{d}_\alpha \cdot \boldsymbol{d}_\beta) + (\boldsymbol{n}_\alpha \cdot \boldsymbol{d}_\beta)(\boldsymbol{n}_\beta \cdot \boldsymbol{d}_\alpha) \tag{1-8}$$

A negative value of N is obtained when a slip direction or slip plane normal is reversed; therefore, the absolute value of N is calculated when the directionality of a dislocation is not considered, such as in this study.

Shen et al. proposed a notable transmission factor which included the grain boundary orientation, and it has been widely used throughout literature [17–19]; however, this transmission factor was not explored in this study as it requires GB inclination angles, which are unavailable via surface EBSD data.

Luster and Morris proposed the compatibility factor, m', which is similar to the N factor except that the last term is dropped [13]. It is defined as

$$m'_{\alpha\beta} = (\boldsymbol{n}_\alpha \cdot \boldsymbol{n}_\beta)(\boldsymbol{d}_\alpha \cdot \boldsymbol{d}_\beta) \tag{1-9}$$

Similar to N, the absolute value of m' was calculated for this study because the directionality of a GB was not considered [20,21]. Additionally, the residual Burgers vector (RBV) is used as a metric to gauge whether slip transmission between two neighboring slip systems is likely [16,22,23]. It measures the residual Burgers vector of the transmitted dislocation left at the GB, and can be defined as

$$RBV_{\alpha\beta} = \left\| \boldsymbol{b}_\alpha - \boldsymbol{b}_\beta \right\| \tag{1-10}$$

where b is the Burgers vector expressed in a consistent coordinate frame for both grains. Both the positive and negative directions of each Burgers vector were considered, and the direction which minimized the residual Burgers vector was used in this dissertation. Many of these transmission factors have been used in exploring dislocation pileup and slip transmission at GBs, and several recent reviews are available [10–12]. While the transmission factors N, m', and RBV, describe the transmissivity of a single slip system combination at the GB, this dissertation looks at the relationship between GNDs and the GB as a whole.

One of the simplest factors in estimating a GBs ability to transmit dislocations is the misorientation angle between neighboring grains, Δg [24,25]. Also, Werner and Prantl presented a slip transmission factor, known as the slip transfer number or λ, which represents the overall propensity for a GB to allow dislocations to pass through [14]; this is in contrast to the previously mentioned factors which consider a single slip system combination at the GB, and not the GB as a whole. The slip transfer number is defined as

$$\lambda = \sum_{\alpha}\sum_{\beta} cos\left(\frac{90^{\circ}}{\psi_c} arccos(\boldsymbol{n}_{\alpha}\cdot\boldsymbol{n}_{\beta})\right) cos\left(\frac{90^{\circ}}{\kappa_c} arccos(\boldsymbol{d}_{\alpha}\cdot\boldsymbol{d}_{\beta})\right) \tag{1-11}$$

where ψ_c and κ_c are limiting angles above which dislocations are assumed not to transfer across the GB; ψ_c and κ_c are assumed to be 15° and 45° respectively, and terms that do not meet $\boldsymbol{n}_{\alpha}\cdot\boldsymbol{n}_{\beta} < \psi_c$ and $\boldsymbol{d}_{\alpha}\cdot\boldsymbol{d}_{\beta} < \kappa_c$ are set to zero [10,14].

The slip transmission factors previously described are generally used as a metric to gauge the difficulty of dislocations to pass from a particular slip system in the incoming grain to a particular slip system in the outgoing grain.

While these transmissivity factors provide significant insight of a GBs transmissivity when the active slip systems in each grain are know, it is often difficult to know which slip systems will activate before a polycrystalline material is deformed. Essentially these parameters cannot be used to determine, nor were they developed to determine, whether a GB will accumulate GNDs or not because the active slip system cannot be determined beforehand. One method for predicting the active slip systems is by looking at the Schmid factor. Carroll et al. found that although the schmid factor correlates with deformation in very large grained material, it did not have as strong of a correlation with deformation in polycrystalline material. Additionally, they found that the Taylor factor had weak correlations with both large grained and polycrystalline material [26]. Because there are so many factors affecting the stress profile within a grain, it is difficult to determine which slip systems will activate prior to deformation, and predicting the active slip systems is an unresolved problem.

Recently, Bieler et al. developed three methods which utilize the slip transmission factor m' in conjunction with the Schmid factor to determine an overall transmissivity of the GB [12,27]. Essentially, all three methods use the Schmid factor to determine which slip systems are most likely to be active, and then m' is used to determine how difficult it is for the active slip systems in neighboring grains to transmit dislocations across the GB. The first method for doing this combines the transmission factor, m', from every slip system combination into a single factor m'_m [12]. This is done by weighting each slip system combination's transmission factor by the Schmid factors associated with those slip systems, such that transmission factors for slip systems that are likely to slip are weighted higher than transmission factors for slip systems that are unlikely to slip. This is represented in the following equation

$$m'_m = \sum_\alpha \sum_\beta m' m_\alpha m_\beta / \sum_\alpha \sum_\beta m_\alpha m_\beta \tag{1-12}$$

The second method considerers the transmission factors, m', between the slip systems which are likely to be active and takes the average of the top three; this parameter will be defined as m'_3 throughout this study [12]. This method considers that slip often occurs on multiple slip systems and that the transmission can occur through multiple slip system combinations. To calculate the value for m'_3, all m' values are considered which have an m' value greater than 0.5 *and* both Schmid factors associated with the slip systems comprising m' are greater than 0.25. Out of this subset of m' values, the mean is taken of up to three m' values with the highest average Schmid factor. GBs with no m' values above the thresholds for m' and Schmid factor were excluded from analysis in this study because m'_3 could be calculated. The m' threshold value of 0.5 and the Schmid factor threshold value of 0.25 were chosen such that a very small minority of the GBs were excluded; while the threshold values in the study by Bieler et al. were 0.6 for m' and 0.35 for Schmid factor, there is not strong justification for a particular set of threshold values. A worked example of how to obtain m'_3 is presented in Figure 1-2.

m'	Incoming Grain Schmid Factors										
	0.498	0.460	0.454	0.408	0.406	0.392	0.288	0.279	0.255	0.242	0.229
Outgoing Grain Schmid Factors 0.466	**<u>0.825</u>**	0.123	**<u>0.639</u>**	**0.789**	0.226	0.014	0.282	0.378	0.320	0.269	0.335
0.430	**<u>0.601</u>**	0.290	0.272	**0.769**	0.376	0.126	0.130	0.325	0.429	0.362	0.134
0.378	**0.828**	0.078	**0.835**	**0.599**	0.015	0.149	**0.618**	0.330	0.126	0.104	0.445
0.279	0.216	0.379	0.168	**0.542**	0.426	0.232	**0.507**	0.185	0.423	0.358	0.102
0.266	0.253	**0.602**	0.211	0.226	0.208	**0.834**	0.114	0.249	0.358	0.241	0.073
0.257	0.215	0.260	0.054	0.318	0.187	**0.637**	0.121	0.290	0.260	0.584	0.242
0.252	0.088	0.079	0.105	0.047	0.043	0.094	0.094	**0.604**	**0.526**	0.005	0.521
0.247	0.157	0.029	0.168	0.104	0.028	0.023	0.134	0.536	0.375	0.019	0.553
0.205	0.222	0.782	0.312	0.073	0.547	0.807	0.318	0.142	0.360	0.166	0.115

Figure 1-2: Worked example for calculating $\boldsymbol{m'_3}$. The bolded values indicate $\boldsymbol{m'}$ parameters that meet the minimum threshold for $\boldsymbol{m'}$ and Schmid factor. The underlined parameters are the three potential $\boldsymbol{m'}$ values with the highest average Schmid factor. In this example $\boldsymbol{m'_3}$ equals .688.

The third method considers slip system combinations with both a high m' and a high Schmid factor, similar to the second method, and takes the highest m' as a representative value for the GB; this will be defined as m_1' throughout this study. m_1' is calculated by determining the slip systems in each grain with the five highest Schmid factors, calculating the m' for these 25 slip system combinations, and then taking the highest m' to be m_1'. A worked example of how to obtain m_1' is presented in Figure 1-3. This method is similar but slightly different than one presented by Bieler et al.; they looked at the max m' value from all slip system combinations where both grains had a Schmid factor greater than 0.25 [27].

m'	Incoming Grain Schmid Factors						
	0.498	0.460	0.454	0.408	0.406	0.392	0.288
Outgoing Grain Schmid Factors 0.466	0.825	0.123	0.639	0.789	0.226	0.014	0.282
0.430	0.601	0.290	0.272	0.769	0.376	0.126	0.130
0.378	0.828	0.078	**0.835**	0.599	0.015	0.149	0.618
0.279	0.216	0.379	0.168	0.542	0.426	0.232	0.507
0.266	0.253	0.602	0.211	0.226	0.208	0.834	0.114
0.257	0.215	0.260	0.054	0.318	0.187	0.637	0.121
0.252	0.088	0.079	0.105	0.047	0.043	0.094	0.094

Figure 1-3: Worked example for calculating $\boldsymbol{m_1'}$. The bolded and underlined value has the highest $\boldsymbol{m'}$ parameter that meets the Schmid factor cut off limits, and it is the value of $\boldsymbol{m_1'}$.

This study takes these three methods by Bieler et. al and applies them to N and RBV. These transmissivity factors are presented as N_m, N_3, N_1, RBV_m, RBV_3, and RBV_1. Equations for N_m and RBV_m are as follows:

$$N_m = \sum_\alpha \sum_\beta N m_\alpha m_\beta / \sum_\alpha \sum_\beta m_\alpha m_\beta \tag{1-13}$$

$$RBV_m = \sum_\alpha \sum_\beta \frac{RBV}{m_\alpha m_\beta} / \sum_\alpha \sum_\beta \frac{1}{m_\alpha m_\beta} \tag{1-14}$$

Because a low RBV is indicative of a slip system combination with easy transmission, $\frac{1}{m}$ was used as the weighting factor to further lower the RBV when slip was likely. Similarly the lowest values of RBV was desired in calculating RBV_3 and RBV_1. Threshold values in calculating N_3 and RBV_3 were 0.5 for N, 2.92×10^{-10} for RBV (this is the Burgers vector for Ta), and 0.25 for the Schmid factor. In addition to these parameters, the mean transmission factor of all slip system combinations was considered as a potential transmissivity factor, and was calculated for N, m', and RBV as follows:

$$N_{avg} = \sum_{\alpha}\sum_{\beta} N_{\alpha\beta} \tag{1-15}$$

$$m'_{avg} = \sum_{\alpha}\sum_{\beta} m'_{\alpha\beta} \tag{1-16}$$

$$RBV_{avg} = \sum_{\alpha}\sum_{\beta} RBV_{\alpha\beta} \tag{1-17}$$

2 INFLUENCE OF NOISE GENERATING FACTORS ON CROSS-CORRELATION EBSD MEASUREMENTS OF GNDS

2.1 Background

The advent of cross-correlation ("high-resolution") electron backscatter diffraction (HR-EBSD) has transformed access to high integrity strain gradients [20–22] and related geometrically necessary dislocation (GND) fields [23–25]. However, the presence of strain gradients is often associated with increased noise in the EBSD pattern; sensitivity of the measured strain gradient field to this noise has not been fully characterized. Furthermore, cross-correlation methods often work "offline"—patterns are saved during a microscope scan, and then analyzed afterwards. The cost in terms of EBSD scan time, memory allocation, data transfer time, and computational effort is critically related to the required resolution of the saved images. This paper considers the effects of resolution and noise on the integrity of the GND measurement process, both from microscope-generated and post-processing-generated contributions (for a review of related noise issues, see [54]. An analysis of these effects will allow users to make more informed decisions relating to trade-offs between computational time/resources and data fidelity.

As a vehicle to performing this study, recent developments in the area of high-fidelity dynamically simulated EBSD patterns have enabled the rapid formulation of simulated EBSD scans relating to "perfect" GND fields [55] (process described below). These patterns can then be manipulated to introduce noise, and to determine the effects of binning parameters, image

format/compression, etc. By using ideal EBSD patterns, the desired relationships between measured and actual GND content can be accurately assessed.

By comparing EBSD patterns via cross-correlation from neighboring points in an EBSD scan, the spatial derivative of the elastic distortion tensor can be determined. Both the resolution of the EBSD patterns and noise from various sources will significantly affect the accuracy of the calculated shifts, and the subsequent fidelity of the calculated strain gradient and associated GND field (see section 1.1 for a detailed description of how is GND is calculated using cross-correlation EBSD). Noise sources include the following:

- Poor sample polish, oxide layers, and hydrocarbon deposition, leading to electron scatter as electrons leave the sample [56].
- Dislocation content in the sample (both GND and statistically stored dislocation (SSD)), reducing the periodicity of the lattice and obstructing channeling.
- GBs within the interaction volume, leading to disruption of structure and mixed patterns.
- Microscope environment issues, such as:
    - Microscope settings (current, voltage, beam alignment, working distance, etc.), leading to such things as, large interaction volumes, low electron yield, and poor projection of patterns on the phosphor screen.
    - Detector and camera attributes and settings, such as gain, binning, quality, and position, may contribute noise and distortion.
    - Electron source (tungsten filament cathode, lanthanum hexaboride cathode, or field emission gun (FEG)), influencing the interaction volume, which in turn can increase the number of dislocations contained within the interaction volume and cause a loss in pattern quality.

- Post-processing of EBSD patterns, such as:
    - Background subtraction potentially introduces bias into the results, as it can cause patterns to mistakenly align to features on the detector (such as scratches or pores) by subtracting identical content from each.
    - Image compression reduces the quality of the images.

In addition to these issues, lack of accurate knowledge of the microscope geometry (in particular, the pattern center (PC) —the relative position of the sample interaction volume and detector) has some influence on the calculated strain gradients. However, this has been shown to be a minor effect in normal situations due to the fact that all patterns have related errors, leading to a low requirement on PC accuracy [57,58]. Similarly, optical distortion of the EBSD pattern may influence the pattern fidelity, but will not create large errors for calculated relative distortion between nearby points [57]. Large interaction volumes can also increase noise in EBSD patterns in some situations because more dislocations can be contained within the large interaction volume and these dislocations degrade the pattern quality.

In this paper, the various noise and resolution influences will be treated under four headings:

- Binning
- Image Compression
- Poisson Noise
- Mixed Patterns

By examining simulated patterns relating to known dislocation strain fields (discussed below), different noise factors can be incorporated into the analysis and their effects understood. The effect

of binning and image compression can be quantified. Random noise can be introduced to gain some insights into noise created by low exposure times, dislocation content, surface damage, low electron yield, or some other internal structural entropy. Furthermore, mixed patterns can be simulated to better understand the effect of an interaction volume spread across multiple grains at a GB.

As these different effects are analyzed, various noise index parameters, available from EBSD analysis software, will also be quantified to determine whether these indices are predictors of strain gradient and GND error in crosscorrelation. Although different software packages define different measures of noise, we focus on those employed by EDAX (Draper, UT, USA), which will be the software package used throughout this paper [59]; other software packages have similar metrics. Measures of noise that are output by the EBSD software include the image quality (IQ), confidence index (CI), and Fit parameter [54].

All of these parameters are a rough estimate of how well the software is able to identify the correct orientation of a pattern. The IQ quantifies the intensity of the Hough peaks of the transformed pattern, and thus gives a measure of contrast between the bands in the pattern and the rest of the pattern [60]. CI is a measure of how "confident" the software is about the orientation it has assigned to a specific pattern (see [59] for more information). A Fit value is a measure of the average angular deviation between the detected orientation and the orientation assigned to the pattern from the program (see [59] for more information). They are dependent on many variables found in the EBSD collection software and microscope settings, but can be used as a value to relatively compare patterns.

The impact of resolution and noise has previously been studied to some extent in the context of cross-correlation EBSD. If only the rotation component of the elastic distortion is

considered in the definition of GNDs (as is commonly the case; see [30,36], then the accuracy of the GND calculation is fundamentally related to the measurement of relative orientation, which has been studied in various ways. For example, early studies estimated relative orientation resolution of cross-correlation EBSD around 0.006° [20,22]. This view formed the basis for defining achievable accuracy in GND measurements, such as proposed by [61,62]; in Figure 2-1, the lower limits for measurable GND content are plotted against scan step size for both standard EBSD and HR-EBSD techniques.

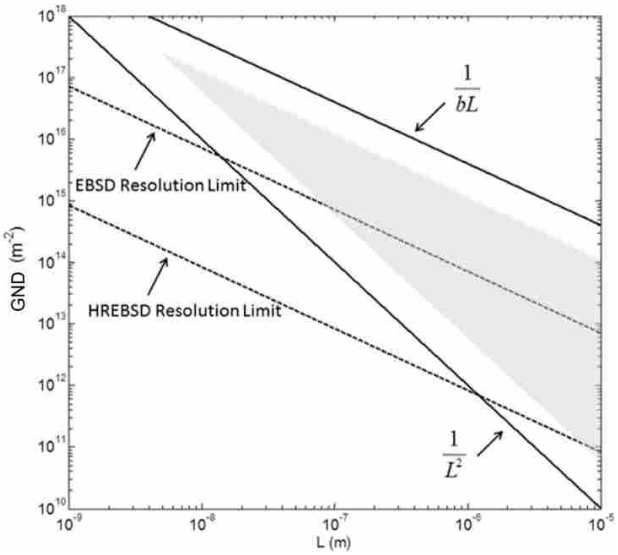

Figure 2-1: Geometrically necessary dislocation (GND) resolution versus step size (L). The dashed lines indicate a lower and upper bounds estimate of GND resolution for an assumed electron backscatter diffraction (EBSD) orientation resolution of 0.5°, and high-resolution EBSD (HR-EBSD) resolution of 0.006°, respectively. The solid lines indicate a lower bound on resolution relating to a single dislocation within the volume bounded by a step, and an upper bound relating to variations in the plastic deformation field; the shaded area is the recommended characterization region according to Kysar et al. [61].

Britton et al. investigated noise factors, such as optical distortion, that particularly affect simulated pattern approaches [57]. It was also determined by Britton et al. [16,63] that a bit depth

of less than 8 bits can significantly reduce precision and binning can increase noise. An extensive study by Tong et al. [64] investigates GB effects by mixing EBSD patterns to simulate a GB. Wright et al. [54] considered methodologies of compensating for noise in EBSD patterns using post-processing techniques; in particular, noise is introduced into real patterns to control the noise level for the study (see also [65] for a general error analysis in EBSD). Most notably, Jiang et al. [19] have studied the effects of binning and step size on measured GND content, albeit on real patterns, thus setting the stage for this study.

2.2 Method

The overall approach taken in this paper was to produce a set of "perfect" dynamically simulated EBSD patterns that correspond to crystal structure variations over a region of a nickel sample with a known GND content. To simulate various noise and image compression effects, the simulated patterns were then subject to the following processes (see Figure 2-2):

- Level of binning of the EBSD pattern was varied from unbinned to 16 × 16 binning.
- Various levels of image compression were applied to the original high-resolution bmp image.
- Poisson noise was inserted into the image at a range of levels.
- Simulated patterns for two different orientations were mixed at varying levels (representing the electron beam interaction volume spanning a GB).

For each of these factors, the resultant GND content over an area of 1,000 data points was calculated from the Nye dislocation density tensor [24], and the IQ, CI, and Fit were determined using OIM software from EDAX [59]. The impact of the binning and compression operations on

the computational time and memory requirements was also recorded. Details of each factor are outlined in a later section.

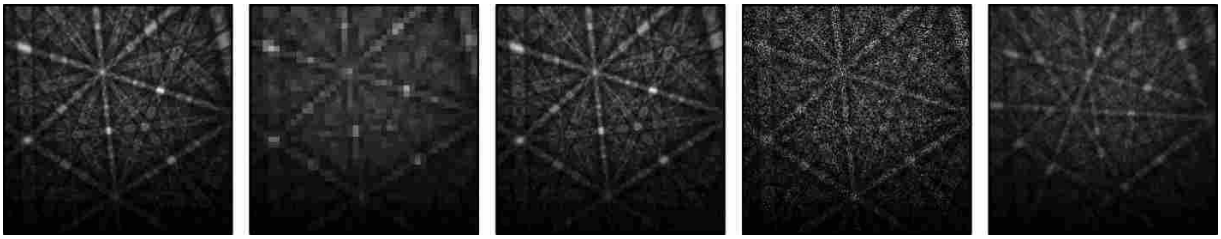

Figure 2-2: Electron backscatter diffraction (EBSD) patterns with varying types of noise. From left to right: no noise, binning, jpeg compression, Poisson noise, and mixing of patterns.

2.2.1 Dislocation Field

In order to produce a predictable Nye tensor, a homogeneous distribution of edge dislocations was assumed for a hypothetical nickel sample, with the Burgers vector, b, pointing in the x-direction, and the line direction, v, pointing along the z-axis (see Figure 2-3) in the ROI. The plane normal to the z-axis is the sample surface for all simulated scans in this paper, that is, the simulated electron beam impinges upon the blue surface shown in Figure 2-3.

In order to provide a specific crystal orientation for the simulated patterns, the (1−1 1)[110] slip system was assumed to be operational, with line direction in the [−1 1 2] direction, in the crystal frame. The crystal was brought into the desired alignment with the global frame using a rotation defined by $\phi_1 = \frac{\pi}{4}, \Phi = -\text{atan}\left(\frac{1}{\sqrt{2}}\right), \phi_2 = 0$ in Euler angles.

Then according to equation (1-1), $\alpha_{13} = \rho$, and all other components of the Nye tensor are zero. As this particular rotation was used, the GND values associated with all simulated

patterns in this study were calculated solely using the α_{13} component of the Nye tensor. Using equation (1-2), and making the common assumption that the strain component of the elastic distortion is negligible, and that, for small rotations, the infinitesimal rotation tensor, ω, is related to the usual misorientation matrix by

$$g \approx I + \omega \tag{2-1}$$

then

$$\alpha_{km} = \epsilon_{jim}\beta^{e}_{kj,i} = \epsilon_{jim}\omega^{e}_{kj,i} + \epsilon_{jim}\varepsilon^{e}_{kj,i} \approx \epsilon_{jim}g_{kj,i} \tag{2-2}$$

where $g_{kj,i}$ is calculated by determining the rotation required to realign the lattice at two points that are separated by dx in the i-direction, and dividing by dx [36]. This rotation was readily calculated accurately using cross-correlation EBSD.

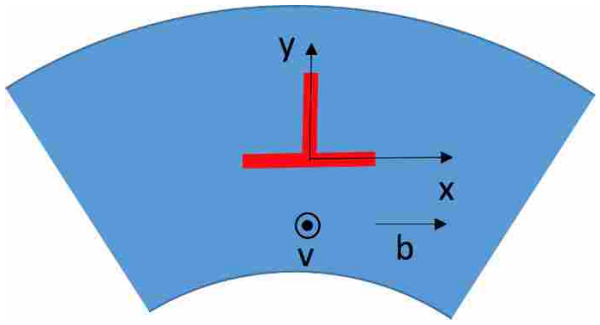

Figure 2-3: Schematic of a dislocation within a geometrically necessary dislocation (GND) field that results in a continuously rotating lattice, as used for this study. The red ⊥ indicates a dislocation within the blue colored bulk material, and b and v represent the Burgers vector and line direction of the dislocation, respectively.

2.2.2 Simulated EBSD Patterns

The simulated EBSD patterns correlating with the lattice and GND field described previously were created using EMsoft 3.0, an open-source software package [66]. The patterns provide a high-fidelity representation of noise-free EBSD patterns (see Figure 2-4 for a representative pattern) that were subsequently injected with the desired noise/filtering. The steps to generate the patterns are described in detail in [55]. They involve: (1) Monte Carlo simulation of the energy, depth, and directional distributions of backscattered electrons for the given crystal lattice; (2) dynamical simulation of the EBSD master pattern, covering all possible backscatter directions with respect to the crystal lattice; and (3) simulation of an electron backscatter pattern (EBSP) for a given detector geometry and sample (grain) orientation. The final patterns generated by EMsoft 3.0 do not take into account the point spread function of the optics that projects the photons onto the charge coupled device (CCD) chip, Poisson noise, or contrast/ brightness scaling that can be applied to the pattern using the EBSD vendor software.

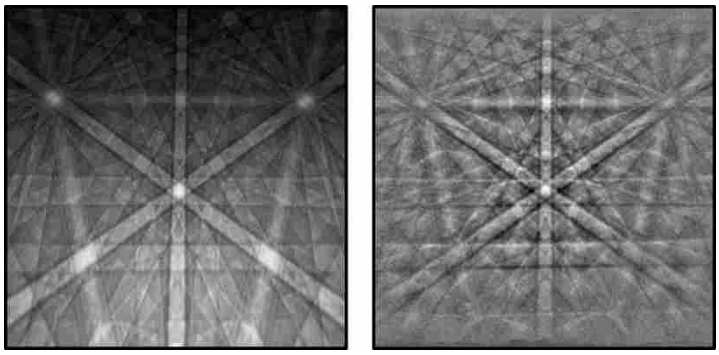

Figure 2-4: Typical simulated pattern of Si using EMsoft 3.0 (left) and an experimental pattern of Si collected from the scanning electron microscope (SEM) (right). The lack of brightness gradient in the experimental pattern is due to background correction applied at the time of collection.

The patterns used in this study were generated with a pixel density equivalent to a high resolution for a typical EBSD detector—640 × 640. The images were saved as bitmaps to ensure no loss of quality in the original images. The microscope settings were typical for EMsoft 3.0 simulations and are as follows: CCD detector size—32mm2, beam current—150 nA, beam dwell time—100 μs, and binning mode—1 × 1. EBSD patterns for pure Ni were generated for a grid of points across a hypothetical sample of size 10 × 0.2 μm using 101 × 3 points, such that the pattern at the origin had the Burgers and line directions aligning with the x and z axes, as described above, and each step of 0.1 μm in the x or y direction correlated with a rotation about the z-axis of 0.144°; thus equating to a GND density of ~1e14m−2. Large rotations have potential to cause inaccuracies in crosscorrelation techniques and several studies have examined methods to alleviate this difficulty [67–69]. By using an extremely small rotation angle between points, 0.144°, this study assumes negligible error due to large rotations. This hypothetical sample was replicated ten times with the step size varying by 0.001μm each time such that a statistically significant amount of data points could be used for data analysis.

2.2.3 Pattern Degradation Approach

Binning is applied in commercial EBSD software to accelerate the pattern collection and analysis (e.g., indexing) of the captured pattern. Typically, images are binned into 1 × 1, 2 × 2, 4 × 4, 8 × 8, or 16 × 16 blocks of pixels, and a new pixel is generated by averaging the intensity of all pixels in the block, and thus replacing the group with a single grayscale intensity [59]. The same approach was applied to the simulated patterns by local averaging of the pixels to produce a new, lower resolution, image at each binning value. In practice, the exposure time is usually reduced as binning is increased because fewer electrons are needed for a decent signal. Exposure

time is the amount of time that the phosphor screen is collecting data for a single point in a scan. With longer exposure times, more electrons are able to impinge upon the phosphor screen and a clearer pattern is produced. The lowering of exposure time as binning increases was not simulated in the study and exposure time was held constant.

Image compression was applied using the MATLAB (Mathworks, Inc., Natwick, MA, USA) "imwrite" function, and applying the default "lossy" compression approach to the bitmap images [70]. The compression level is controlled by the "Quality" flag, which varies from 0 to 100; the highest numbers have the least compression. This "Quality" flag is later used in this paper as a metric to describe compression levels and is written as "Compression Quality." Compression was applied in steps of 10, from 100 to 10. The resultant memory requirements were also recorded as a practical measure of the compression level.

Poisson noise was added to the pattern to reflect noise in electron interactions and camera electronics, in line with previous studies of noise in EBSPs [54,71–73]. Although others have cited Poisson noise as a representative noise type for some factors in the imaging process, its application to specific aspects in EBSD imaging within this paper have been inferred based on statements in the referenced papers. The Poisson noise was introduced using the MATLAB "poissrnd" function, and adjusting the function input variable "λ." This Poisson noise was then multiplied by the original unadulterated image to get the final degraded pattern. λ is a rate parameter which represents the average number of times an event will occur per unit of time. As the value for λ was lowered, the quality of the image decreased. For a clearer understanding of the results, the values of λ were normalized using a parameter, "Poisson Noise Level," which was calculated by dividing the maximum value of λ used in this study by the λ used for a particular instance of noise addition.

To compare trends in noisy simulated patterns with experimental results, ten EBSD scans of a Ta sample were taken with varying exposure times. In order to isolate exposure time as the source of noise, gain was set to 0, 1 × 1 binning was used, and patterns were saved as 8-bit jpeg images. A contrast normalization filter was used so that patterns collected at a low exposure time could still be indexed by the EBSD collection software. Exposure time was varied in order to explore its effects, as well as mimic oxide layer, hydrocarbon deposition, dislocation content, and any other phenomena that would reduce the electron yield on the phosphor screen. Scans of 10 × 10 μm with a step size of 0.1 μm were taken at the same location on the sample for all exposure times using an FEI S-FEG XL 30 microscope (FEI, Hillsboro, OR, USA) and typical settings. Scans were taken from shortest to longest exposure, which could have introduced noise due to hydrocarbon build-up in the later scans. This noise due to hydrocarbon build-up is assumed to be negligible compared with the noise differences associated with the different exposure times. High-quality images of the scans were saved and used for cross-correlation.

Mixed patterns at GBs were simulated by overlaying patterns of two different orientations, with the contribution from each pattern being scaled linearly relative to the distance from the GB. In reality the contribution from the two patterns has been found to vary after the form of a sigmoid function [74]. The patterns from the grain of interest were mixed with a pattern from a nearby grain in a linear fashion. To achieve linear mixing of patterns, the GB was assumed to have a 90° tilt, the interaction volume was assumed to be cube shaped instead of tear-drop shaped for simplicity, and the pattern intensity of a grain in a mixed pattern was assumed to be proportional to the fraction of interaction volume inside that grain (this last assumption is a reasonable reflection of reality, as per Tong et al., 2015). A relatively small step size of 0.1 μm and an unrealistically

large probe diameter of 2.2 μm were assumed in order to maintain a realistic step size for GND detection yet also capture a large transition of patterns at the GB.

The three following GBs were observed in this study:

- A low angle GB, with one side having a GND density of 1e14m−2 and the other having a density of 1e15m−2 (misorientation angle of 4.15°, Burgers vector of 2.45e−10 m, and dislocation spacing of 3.38e−9m).
- A high angle GB, with one side having a GND density of 1e14m−2 and the other having a density of 0m−2.
- A high angle GB, with one side having a GND density of 0m−2 and the other having a density of 0m−2.

Previous studies have examined dislocation build-up at GBs as an important microstructural characteristic [49,75–77]. This study wishes to determine whether pattern mixing at GBs constitutes a form of noise that might be wrongly interpreted as dislocation content. Case (c) investigates how pattern mixing at a GB may manifest itself as dislocation density in a cross-correlation analysis when no GNDs are present. Cases (a) and (b) more specifically consider whether the pattern mixing appears as GND build-up in cases where there is a GND field, but no actual build-up at the GB.

In addition to the simulated patterns, a GB in an annealed Ta sample was scanned with EBSD on an FEI S-FEG XL 30 microscope using typical settings in order to compare the simulated data with experimental. Through etching, it was found that GBs on the front and the back of the specimen near perfectly aligned, leading to the assumption of a columnar grains. The scan was 6.325 × 0.5375 μm and was taken with a step size of 0.025 μm. The orientation of the left grain

(as shown in Figure 2-15), given in Bunge Euler angles (°), is 88.3, 40.1, 230.8, and the orientation for the right grain is 134.9, 38.7, 192.6. Eight-bit jpeg images of the scan were saved and used for cross-correlation.

2.2.4 Pattern Analysis and Cross-Correlation

Once a set of patterns was created for a given degradation type, a suitable data file, was created using the same parameters that were input into the EMsoft package and that file, along with the patterns, were processed using the EDAX software in order to collect noise parameters: IQ, CI, and Fit. Typical and consistent settings were used with all of the EDAX software. The patterns were then fed into an open source cross-correlation EBSD code developed by the authors, OpenXY (Brigham Young University, Provo, UT, USA), to analyze the GND content [78]. Cross-correlation measurements in EBSD were originally introduced by Troost et al. and further developed by Wilkinson et al. [21,22,27]. The exact process used in OpenXY is based upon work by Kacher and Landon [20,79]. An important step in HREBSD for getting the best analysis is pattern filtering [22] and its use is evident in various studies [20,63]. Different filtering techniques and settings were not examined in this study and the default filter settings for OpenXY were used for all data sets analyzed with cross-correlation (default settings were originally determined by optimizing over a series of test cases).

2.3 Results and Discussion

The original unadulterated patterns were analyzed by OpenXY, resulting in a mean GND density of 9.3e13m−2, with a SD of 3.8e11m−2. This was the baseline mean and noise floor for the other tests with degraded images.

2.3.1 Binning

Figure 2-5 displays representative images with varying binning levels. The effect of image binning on the calculated GND density is captured in Figure 2-6. All box and whisker plots shown in this article use the standard rules to determine the size of the box and have a maximum whisker height of 3/2 times that of the box (cross-hairs indicate all data outside of the box and whisker range). A blue line connecting the medians in the box and whisker plots is to aid the reader in seeing plot trends. Statistical values related to the binning results are reported in Table 2-1, along with the resultant memory and computational requirements, IQ, Fit, and CI. Percent error in the table indicates the percent error of the mean GND density from the idealized GND density, 1e14m−2.

As can be seen from Figure 2-6, 2 × 2 binning does not have a large effect on the resultant calculated GND density. However, beyond the 2 × 2 binning, both the mean and standard deviation drift significantly away from those of the original figure. This is not surprising given that binning is effectively the same as reducing the image resolution or increasing the solid angle per pixel in the EBSP. As image resolution is decreased, one would expect the changes in the EBSP to be visible in the cross-correlation results. A study by Jiang et al. [19] showed that experimental binning increased GND content and similar results have been observed by the author in single crystal Si. This is in contrast to the results of this study which show a decrease in mean GND with increased binning. Due to the many factors involved, it is difficult to predict whether GND will go up or down with increased binning, but for this particular set of simulated patterns it was shown that the GND density decreased.

The IQ, CI, and Fit do not appreciably deteriorate although some deterioration is noticeable at higher binning levels. Hence, none of these noise indicating variables are strong indicators of

accuracy of the cross-correlation results in this case. The level of binning has a dramatic effect on both memory requirements and time required to process the data (see the values in Table 2-1). As these both drop markedly with 2 × 2 binning and the accuracy of the GND calculation is not drastically reduced at this level of binning, this may be the optimal level of binning for practical situations.

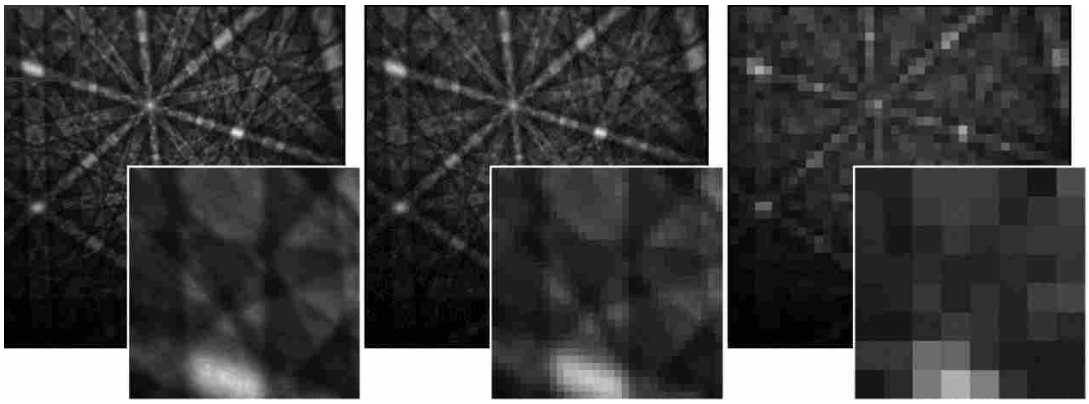

Figure 2-5: Representative images at 1×1 (original resolution of 640×640 pixels), 4×4 and 16×16 binning levels, respectively. The inset figures are enlarged versions of the top-left corner of each image to demonstrate the effect of binning at the region of interest level.

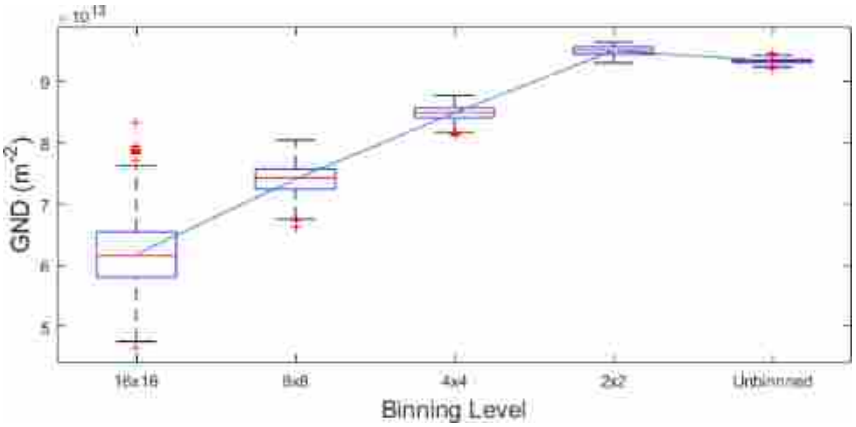

Figure 2-6: Calculated levels of geometrically necessary dislocation (GND) after introducing binning into dynamically simulated patterns.

Table 2-1: Statistical Summary of Introducing Binning into the Dynamically Simulated Images.

Binning Level	GND Mean (m^{-2})	Percent Error (%)	Max GND (m^{-2})	Min GND (m^{-2})	Standard Deviation	Memory (%)	Time (%)	IQ ($\times 10^5$)	CI	Fit
No Binning	9.34×10^{13}	6.6	9.45×10^{13}	9.20×10^{13}	3.81×10^{11}	100	100	1.73	0.97	0.42
2x2	9.50×10^{13}	5	9.64×10^{13}	9.31×10^{13}	6.95×10^{11}	25.2	37.9	1.74	0.97	0.42
4x4	8.49×10^{13}	15.1	8.77×10^{13}	8.12×10^{13}	1.13×10^{12}	6.5	22	1.76	0.97	0.46
8x8	7.41×10^{13}	25.9	8.05×10^{13}	6.62×10^{13}	2.44×10^{12}	1.8	17.2	1.65	0.96	0.47
16x16	6.18×10^{13}	38.2	8.32×10^{13}	4.66×10^{13}	5.58×10^{12}	0.7	15.7	1.32	0.89	0.52

2.3.2 Image Compression

A visualization of the degradation of pattern quality with image compression is shown in Figure 2-7 (see "Pattern Degradation Approach" in this paper for more details on the definition of compression and "Compression Quality"). The impact on GND calculations from compressing the simulated images is captured in Figure 2-8 and Table 2-2. The figure illustrates that significant levels of compression can be achieved without having a large impact on the resultant GND calculations. IQ, CI, and Fit are all negligibly affected by the compression process. Similarly, the time taken to process the images by OpenXY does not change significantly. On the other hand, the memory requirements drop consistently with each level of compression, as captured by the data in the table. Hence, an optimal level of compression is likely to be a "quality" value somewhere between 50 and 90 (between 1/20 and 3/20 of original image memory requirements).

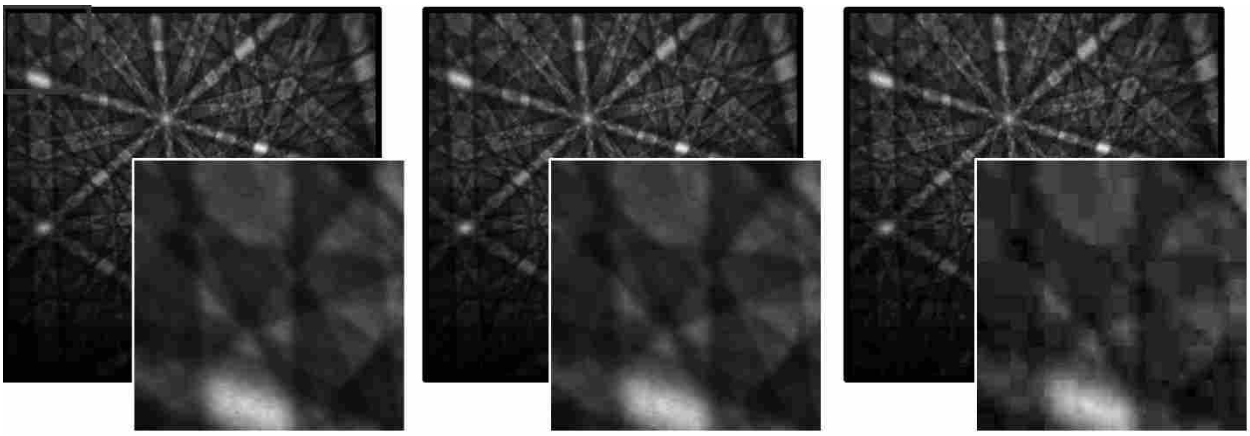

Figure 2-7: Representative images at original resolution and 50 and 10% quality, respectively. The inset figures are enlarged versions of the top-left corner of each image to demonstrate the effect of compression at the region of interest level.

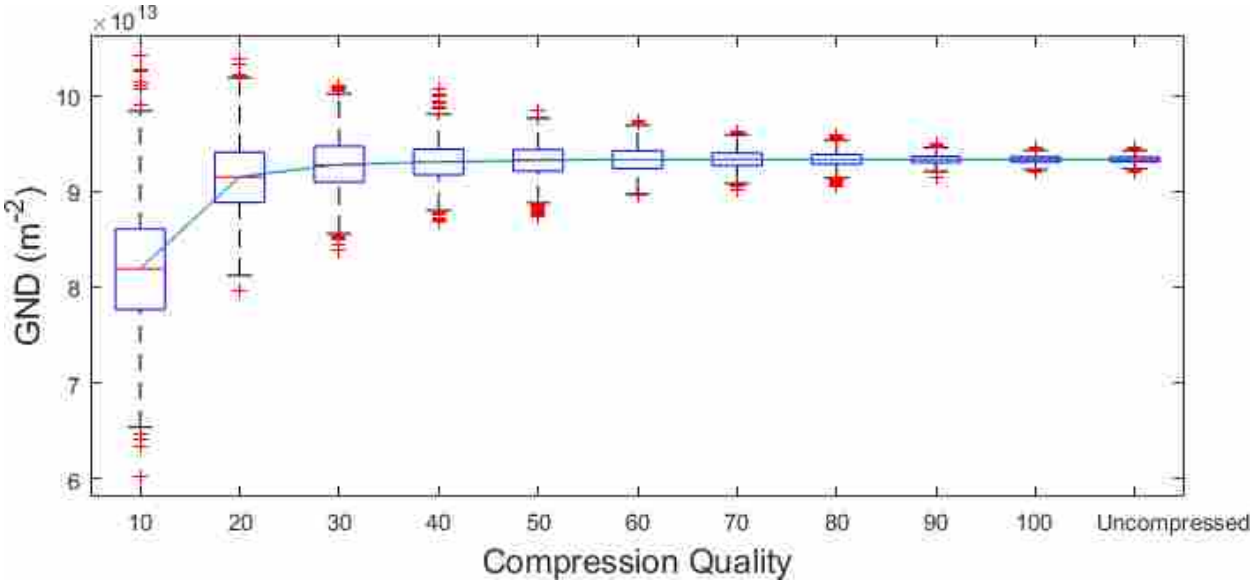

Figure 2-8: Calculated levels of geometrically necessary dislocation (GND) after introducing compression into dynamically simulated patterns.

Table 2-2: Statistical Summary of Introducing Compression into the Dynamically Simulated Images.

Compression Quality	GND Mean (m^{-2})	Percent Error (%)	Max GND (m^{-2})	Min GND (m^{-2})	Standard Deviation	Memory (%)	Time (%)	IQ ($x10^5$)	CI	Fit
Uncompressed	9.34×10^{13}	6.6	9.45×10^{13}	9.20×10^{13}	3.81×10^{11}	100	100	1.73	0.97	0.42
100	9.34×10^{13}	6.6	9.46×10^{13}	9.20×10^{13}	4.00×10^{11}	44.4	100	1.73	0.97	0.43
90	9.34×10^{13}	6.6	9.49×10^{13}	9.15×10^{13}	4.90×10^{11}	15.5	99.4	1.73	0.97	0.43
80	9.34×10^{13}	6.6	9.58×10^{13}	9.05×10^{13}	7.83×10^{11}	10.2	104	1.73	0.97	0.42
70	9.33×10^{13}	6.7	9.63×10^{13}	9.02×10^{13}	9.88×10^{11}	8.1	96.3	1.73	0.97	0.42
60	9.33×10^{13}	6.7	9.73×10^{13}	8.96×10^{13}	1.38×10^{12}	6.7	96.3	1.73	0.97	0.43
50	9.33×10^{13}	6.7	9.85×10^{13}	8.74×10^{13}	1.72×10^{12}	5.9	95.2	1.73	0.97	0.42
40	9.31×10^{13}	6.9	1.01×10^{14}	8.68×10^{13}	2.08×10^{12}	5.1	94.3	1.73	0.97	0.43
30	9.28×10^{13}	7.2	1.01×10^{14}	8.39×10^{13}	2.82×10^{12}	4.3	97.5	1.73	0.97	0.42
20	9.16×10^{13}	8.4	1.04×10^{14}	7.96×10^{13}	3.85×10^{12}	3.4	99.5	1.72	0.97	0.42
10	9.19×10^{13}	8.1	1.04×10^{14}	6.03×10^{13}	6.48×10^{12}	2.3	95.7	1.72	0.97	0.44

2.3.3 Poisson Noise

The consequence of introducing Poisson noise at various levels into the original images is graphically displayed in Figure 2-9. The resultant dramatic effect on the calculated GND density is captured in Figure 2-10 and Table 2-3. The calculated mean GND level is not greatly affected by the noise (at reasonable levels), but the standard deviation rapidly increases as noise is introduced. Interestingly, the IQ, CI, and Fit do not decrease until the highest three levels of noise are applied.

Representative EBSD patterns taken experimentally at various exposure times can be found in Figure 2-11. The effect on the calculated GND density is seen in Figure 2-12 and Table 2-4, and follows a similar trend as the simulated patterns. The percent error values for the experimental patterns are based on the mean GND from the highest exposure time. The larger variance in GND values compared with that of the simulated patterns is most likely due to a greater difficulty in

precisely identifying the orientation during the crosscorrelation process. The IQ, CI, and Fit all decrease much more drastically than for the simulated patterns. The simulated patterns were not being degraded to the same level as experimental patterns, which can be seen by inspecting the pattern with the highest degradation in Figure 2-9 compared with the pattern with the lowest exposure time in Figure 2-11. As the noise from both the simulated patterns and experimental patterns gave such a high standard deviation for the calculated GND, noise of this type could play a significant role in determining the approach one uses in collecting EBSPs.

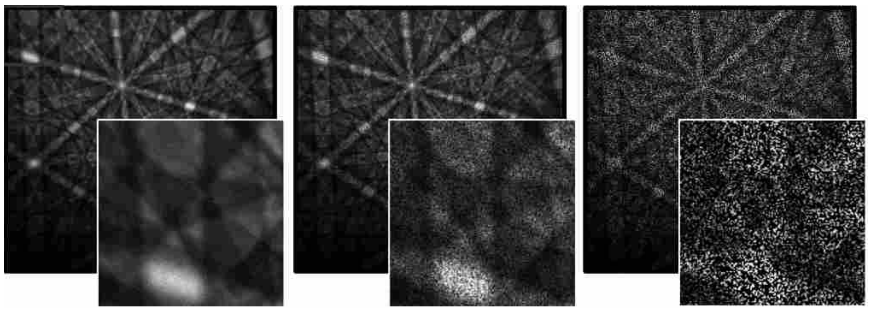

Figure 2-9: Representative images of original image, and images with Poisson noise levels of 16 and 128, respectively. The inset figures are enlarged versions of the top-left corner of each image to demonstrate the effect of Poisson noise at the region of interest level.

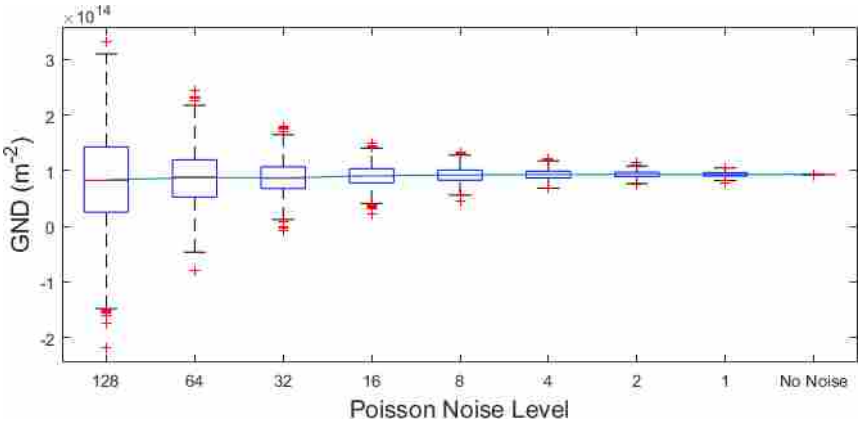

Figure 2-10: Calculated levels of geometrically necessary dislocation (GND) after introducing Poisson noise into dynamically simulated patterns.

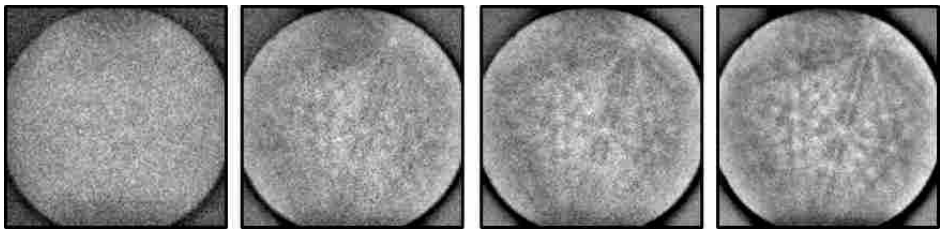

Figure 2-11: Patterns of Ta captured from the microscope at exposure times of 10, 5, 3, and 1 ms, respectively.

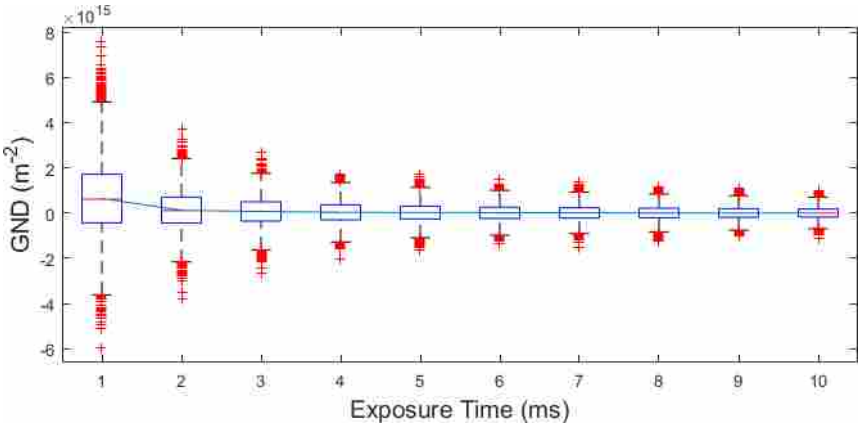

Figure 2-12: Calculated levels of geometrically necessary dislocation (GND) from experimental scans taken at various exposure times.

Table 2-3: Statistical Summary of Introducing Poisson Noise into the Dynamically Simulated Images.

Poisson Noise Level	GND Mean (m^{-2})	Percent Error (%)	Max GND (m^{-2})	Min GND (m^{-2})	Standard Deviation	IQ ($x10^5$)	CI	Fit
No Noise	9.34×10^{13}	6.6	9.45×10^{13}	9.20×10^{13}	3.81×10^{11}	1.73	0.97	0.42
1	9.34×10^{13}	6.6	1.06×10^{14}	7.86×10^{13}	4.30×10^{12}	1.72	0.97	0.43
2	9.33×10^{13}	6.7	1.39×10^{14}	7.42×10^{13}	6.18×10^{12}	1.72	0.97	0.42
4	9.32×10^{13}	6.8	1.22×10^{14}	6.72×10^{13}	9.31×10^{12}	1.71	0.97	0.43
8	9.25×10^{13}	7.5	1.34×10^{14}	4.58×10^{13}	1.34×10^{13}	1.7	0.97	0.43
16	9.08×10^{13}	9.2	1.50×10^{14}	2.30×10^{13}	1.86×10^{13}	1.69	0.97	0.44
32	8.70×10^{13}	13	1.79×10^{14}	-8.45×10^{12}	3.05×10^{13}	1.64	0.97	0.45
64	8.75×10^{13}	12.5	2.44×10^{14}	-8.07×10^{13}	4.94×10^{13}	1.52	0.96	0.47
128	8.37×10^{13}	16.3	3.31×10^{14}	-2.18×10^{14}	8.84×10^{13}	1.2	0.94	0.5

Table 2-4: Statistical summary of experimental patterns with varying exposure times.

Exposure Time (ms)	GND Mean (m^{-2})	Percent Error (%)	Max GND (m^{-2})	Min GND (m^{-2})	Standard Deviation	IQ ($x10^6$)	CI	Fit
10	1.15×10^{13}	0	9.88×10^{14}	-1.10×10^{15}	2.66×10^{14}	6.98	0.91	0.59
9	1.14×10^{13}	0.87	1.08×10^{15}	-9.83×10^{14}	2.87×10^{14}	6.76	0.92	0.58
8	1.39×10^{13}	-20.87	1.17×10^{15}	-1.25×10^{15}	3.13×10^{14}	6.57	0.91	0.61
7	1.88×10^{13}	-63.48	1.38×10^{15}	-1.51×10^{15}	3.43×10^{14}	6.24	0.89	0.65
6	1.67×10^{13}	-45.22	1.52×10^{15}	-1.36×10^{15}	3.71×10^{14}	5.96	0.88	0.66
5	3.06×10^{13}	-166.09	1.72×10^{15}	-1.65×10^{15}	4.14×10^{14}	5.74	0.85	0.92
4	4.11×10^{13}	-257.39	1.72×10^{15}	-2.04×10^{15}	4.91×10^{14}	5.27	0.81	0.79
3	7.79×10^{13}	-577.39	2.69×10^{15}	-2.63×10^{15}	6.32×10^{14}	4.74	0.68	0.93
2	1.30×10^{14}	-1030.43	3.69×10^{15}	-3.81×10^{15}	8.61×10^{14}	4.06	0.38	1.31
1	6.57×10^{14}	-5613.04	7.56×10^{15}	-5.93×10^{15}	1.62×10^{15}	3.32	0.03	2.07

2.3.4 Mixed Patterns

A series of simulated patterns mixing is demonstrated in Figure 2-13. The calculated GND content from the three different GBs that were simulated is summarized in Figure 2-14. Both the GBs that contained GNDs showed a smooth transition from one GND value to another. An increase in GND content is seen at the GB when there is no GND content on either side of the GB. Most likely this increase is not visible in the other two GB due to its comparatively small amplitude.

Resulting GND content, IQ, CI, and Fit from the experimental mixed patterns are shown in Figure 2-15. The four plots in Figure 2-15 are horizontally aligned with the inverse pole figure (IPF) and are the same scale such that a data point in the plots correspond to a point in the IPF directly above. The region affected by this GB was ~2 μm across (for a general in-depth look at interaction volume with application to EBSD see [18]. As the step size for an HR-EBSD scan is generally not much smaller than 1 μm, the GB effected area will only affect a few scan points across the GB and have a minimal effect. There is a GND increase of about 1.5 times the approximated value at the GB and there is a marked degradation in all noise parameters. As the IQ, CI, and Fit for both the simulated high angle GBs (top and middle in Figure 2-14) so closely resembled those of the experimental scan, they were not shown and can be assumed to follow the same trends. The low angle GB had similar IQ behavior as all the others but the CI and Fit remained relatively constant across the GB. With the patterns between the grains being so similar across the simulated low angle GB, the EDAX software was still able to identify the orientations and maintain high-quality levels with the CI and Fit parameters.

Based on the results from the simulated data, one could anticipate a transition from one GND level to another when moving from one grain to another, with a slight increase in GND content at the GB due to the noise of mixed patterns. Experimentally, the GND increase at the GB

is much greater than the simulated GB; this is likely due to other pattern degradation factors coming in to play at the GB besides pattern mixing. This discrepancy between simulation and experimental may show that the simulation methods used in this paper are not adequate at representing a GB for HR-EBSD analysis.

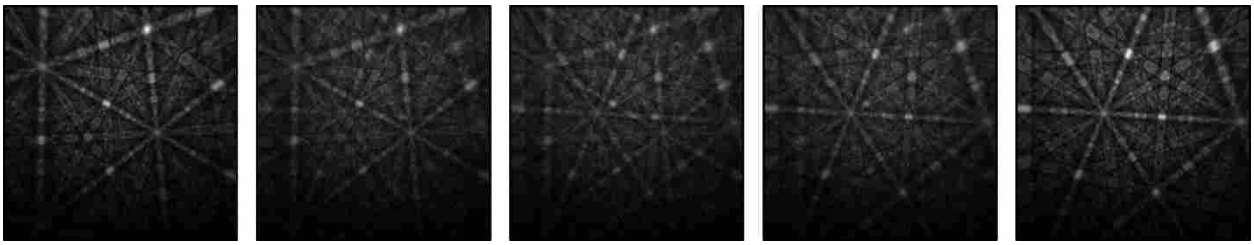

Figure 2-13: A series of dynamically simulated patterns mixing from one orientation to another in a linear fashion. The middle pattern is representative of a scan point directly on a grain boundary, with a 50% pattern contribution from both grains.

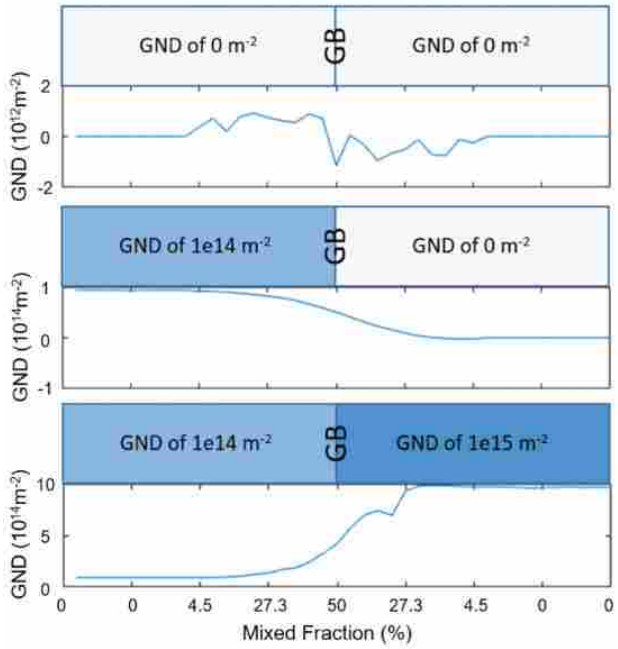

Figure 2-14: Calculated geometrically necessary dislocation (GND) values from three different simulated grain boundaries (GBs). The top two are high angle GBs and the bottom is a low angle GB.

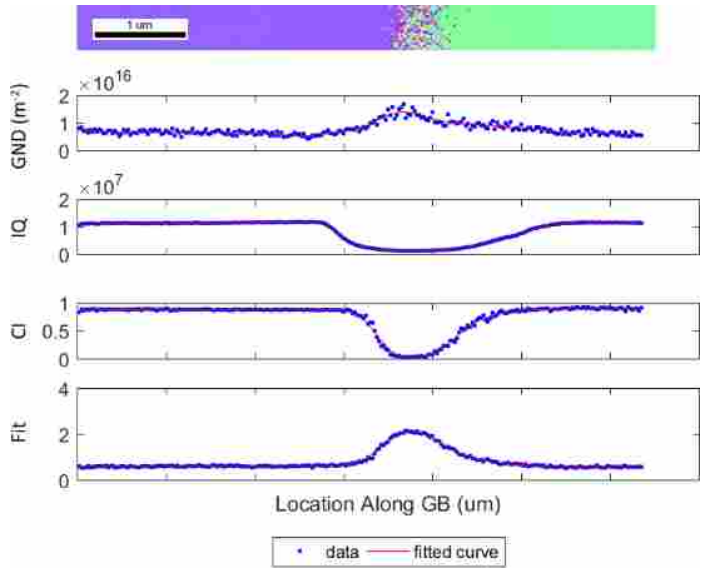

Figure 2-15: Geometrically necessary dislocation (GND) values from OpenXY and image quality (IQ) parameters from DAX software of data from an experimental scan across a grain boundary (GB). CI, confidence index.

2.4 Conclusions

The study of dislocation content in crystalline materials is fundamental to the ability to fully understand and model them. Cross-correlation EBSD has provided a valuable tool for extracting the GND content for such studies. However, offline analysis of high-quality EBSD patterns can be expensive in terms of memory and time and, more importantly, time spent collecting patterns on the microscope is valuable.

The results in this study indicate that the quality of the measured GND content may be allowable at lower levels of binning and compression, such as 2 × 2 binning and a compression quality of 80. IQ, CI, and Fit had a minor correlation with binning level but little to no correlation with compression level. A binning level of 2 ×2 achieves a fourfold reduction in memory requirements, and almost a threefold reduction in run-time without dramatically reducing accuracy. Although compression level does not significantly affect run-time, a compression

"quality" level of 80 can achieve a ninefold reduction in memory requirements without significant reduction in accuracy.

The insertion of Poisson-type noise into the image (e.g., due to exposure time, oxide layers, hydrocarbon deposition, or poor electron yield) does not have a significant effect on the mean GND density content, but the standard deviation of the detected GND content rapidly increases with increased noise levels. These results proved to be similar to experimental results with a varying exposure time. IQ, CI, and Fit in both simulated and experimental patterns did correlate with Poisson-type noise but more closely resembled relative values than a predictor for any set of patterns. Due to the potential for very high GND standard deviation rates, this type of noise can greatly inhibit the accuracy of calculated results and should be avoided.

In characterizing how pattern mixing at a GB affects cross-correlation measurements of GND, it is apparent that simulated mixed patterns were not a good representation of experimental results. Simulated mixed patterns at a GB produced a fairly smooth transition in GND content from one grain to the other, whereas experimental results showed a slight increase in GND content at the GB. This discrepancy can be attributed to the fact that there are many other sources of noise associated with an experimental GB other than the mixing of patterns. To study noise at a GB using simulated patterns, a more in-depth approach would need to be taken. Although the cross-correlation results between simulation and experimental did not reasonably compare, some connections between simulation and experimental concerning IQ, CI, and Fit were able to be made.

High-quality dynamically simulated patterns from EMsoft 3.0 have allowed the characterization of various effects of noise on the measured strain gradient. Simulated patterns have proven to be useful in identifying the particular problems faced in this study, but they could

also be applied to many other types EBSD scenarios to exploit the strengths and pitfalls of cross-correlation techniques.

3 AN INVESTIGATION OF GEOMETRICALLY NECESSARY DISLOCATIONS AND BACK STRESS IN LARGE GRAINED TANTALUM VIA EBSD AND CPFEM

Dislocation slip is the main mode of plastic deformation in metals, and impeding a dislocation's ability to slip is central to many strengthening mechanisms. For example, forest dislocations impede the motion of other dislocations in strain hardening, grain boundaries (GBs) act as barriers in GB strengthening, solute atoms cause lattice distortion in solid solution strengthening, and second phase particles block dislocations in precipitation hardening. Both statistically stored dislocations (SSDs) and geometrically necessary dislocations (GNDs) interact with mobile dislocations in strain hardening, resulting in a local friction-type stress [80–82]. GNDs, which are required in order to maintain lattice continuity within grains, also produce a back stress [83,84] due to the additive nature of their associated stress fields [80].

Back stress is an elastic long-range stress, also referred to as a long-range internal stress, due to the accumulation of GNDs, which are stored in deformation gradients or gradient structures [84,85]; GNDs tend to accumulate at barriers or obstacles, such as the ones previously mentioned [84]. These stresses have long-range interactions with mobile dislocations, thus obstructing further deformation [85,86]. Essentially the effective resolved shear stress which causes dislocation slip is reduced when the back stress acts in the opposite direction [82,85,87]. This hardening effect that back stresses and GNDs have on a material is referred to as kinematic hardening, back stress strengthening, or back stress strain hardening [81,84,85,87]. Because back stress results from the

collective stress fields of GNDs, insights about back stress and its importance can be gleaned through the study of GND evolution.

Ashby demonstrated that when a polycrystal is deformed, local plastic heterogeneity — caused by varying directionality of slip systems in neighboring grains — leads to the requirement for strain gradients, and hence GNDs, in order to maintain compatibility at interfaces [83,88]. This often leads to high levels of GNDs near the GB region. These GNDs must exist due to incompatibility, even without considering a GB obstacle strength that blocks dislocation movement at the interface [83,89].

However, in addition to the existence of incompatibility at GBs, many people have also demonstrated that GBs act as obstacles to dislocation motion [4,37,40,43,49,89], thus complicating the prediction of the GND arrangement that will occur within a grain. Furthermore, intra-grain obstacles such as precipitants, defects, and forest dislocations interfere with dislocation motion and cause dislocation structures, such as micro shear bands, cell boundaries, and dislocations cells, to develop within the grain [89–91]. The strengthening effect associated with these structures increases with strain while the size of these structures decreases with strain [89,92]; thus, increasing strain has a net effect of increased GNDs throughout the grain. With GND evolution being influenced not just by incompatibility, but also by GBs and intra-grain dislocation structures, understanding the accumulation of GNDs and the associated back stresses is a complex problem.

This study explores the evolution of back stress-causing GNDs and the effects of back stress through experimental and simulated methods using large grained tantalum tensile samples. The evolution of GNDs due to strain and rotation gradients was explored via electron backscatter diffraction (EBSD). The resulting GND data was used to evaluate the correlation between GND density pileup at GBs and various geometrically based slip transmission factors. Furthermore, the

GND data from EBSD was used to visualize structures formed by dislocations of the same sign. Finally, a standard crystal plasticity finite element method (CPFEM) and the super dislocation model (SD model), a modified CPFEM which includes back stress and GB interactions, were used to determine how back stress due to GNDs affect the flow stress and hardening rate.

3.1 Background

3.1.1 CPFEM Framework

CPFEM is a well-established computational technique at the macroscopic level which discretizes a polycrystal into finite elements, with many elements per grain. It considers crystallographic orientation, allowing it to account for incompatibility between grains. Furthermore, dislocation activity is frequently modeled in CPFEM through a dislocation density-based single crystal constitutive equation. To reproduce the correct macroscale response, dislocation hardening parameters in the single crystal constitutive equation are commonly fit to the measured stress-strain response of the specific microstructure being simulated.

A recently developed CPFEM, known as the SD model, assumes traditional dislocation behavior within the framework of CPFEM, but also incorporates elastic interactions between populations of dislocations and with grain boundaries, effectively including non-local effects of back stress into the model [93]. Furthermore, the SD model also has an inherent length scale for dislocation evolution, in the form of the magnitude of the net Burgers vector [94]. With this conceptually simple modification to standard CPFEM, the SD model has been shown to accurately predict the following without the addition of arbitrary length scale parameters: Hall-Petch slopes and stress-strain curves in iron [93], the location of high lattice curvature regions in several grains

of an Fe-3% Si sample [93], average dislocation densities in a deformed Fe-3% Si sample [95], Bauschinger behavior in precipitation hardened Al alloys with very fine precipitates (~10-20 nm diameter and ~100-200 nm spacing) [96], and elastic-plastic mechanical behavior, in particular, non-linear transition during unloading and reloading of DP980 using a representative volume element based on measured micro-properties [97].

The power-law form of viscoplastic shear rate, $\dot{\gamma}^{(\alpha)}$, is adopted for the CPFEM and SD model as follows [98]:

$$\dot{\gamma}^{(\alpha)} = \dot{\gamma}_0 \left(\frac{\tau^{(\alpha)}}{g^{(\alpha)}}\right)^{\frac{1}{m}} sign(\tau^{(\alpha)}) \tag{3-1}$$

where $\tau^{(\alpha)}$ is the resolved shear stress on the slip system α, $\dot{\gamma}_0$ is a reference shear rate, m is a strain rate sensitivity, and $g^{(\alpha)}$ is the slip resistance on the slip system α.

In both CPFEM and SD implementations, a dislocation density-based constitutive equation for single crystals is adopted [94]. The initial dislocation density is equally divided on all slip systems in each element; due to the choice of slip systems used, an equal distribution of dislocations results in a net GND content of zero. The slip resistance of slip system, $g^{(\alpha)}$, evolves with plastic shear strain on all slip systems according to

$$g^{(\alpha)} = A\mu b\sqrt{\sum_{\beta=1}^{NS} h_{\alpha\beta}\rho^{(\beta)}} \tag{3-2}$$

where μ is the shear modulus, b is the Burgers vector, $\rho^{(\beta)}$is the dislocation density in slip system β, and NS is the number of slip systems. $h_{\alpha\beta} = n^{(\alpha)}\xi^{(\beta)}$ represents the interaction cosine, where $n^{(\alpha)}$ and $\xi^{(\beta)}$ are the slip plane normal of slip system α and the dislocation line vector of slip system β, respectively. Details of the geometric formulation are described with more detail in [94].

The parameter A is a material constant that ranges from 0.3-0.6 [99,100]; a value of 0.4 was assumed in the SD and CPFEM models for the simulations in this study. The dislocation density $\rho^{(\alpha)}$ on slip system α evolves according to a well-known dislocation density evolution equation [101]:

$$\dot{\rho}^{(\alpha)} = \frac{1}{b}\left(\frac{\sqrt{\sum_{\beta=1}^{NS}\rho^{(\beta)}}}{k_a} - k_b\rho^{(\alpha)}\right)\dot{\gamma}^{(\alpha)} \tag{3-3}$$

where k_a and k_b are single crystal dislocation hardening parameters related to dislocation generation and annihilation, respectively. The hardening parameters in CPFEM and the SD model are fit to experimental stress-strain curves of the material being simulated. In fitting the hardening parameters for the CPFEM, it is critical that the material they are fit to also have the same microstructure as the simulation. This allows the CPFEM to capture the macroscopic behavior of polycrystals; the single crystal hardening parameters, k_a and k_b, in this case do not represent true single crystal behavior, but rather some combination of dislocation hardening, elastic dislocation interactions, and grain boundary effects. Because the SD model explicitly includes elastic dislocation interactions and grain boundary effects within its framework, its hardening parameters are possibly a more accurate reflection of true single crystal hardening parameters; the SD model has demonstrated this by modeling deformation at multiple length scales, e.g. the Hall-Petch slopes [93], while using only one set of single crystal hardening parameters.

In the SD treatment, the GND density for each slip system in each element is treated as a single superdislocation located at the centroid of the element. Mobile dislocation content at the end of each time step is calculated to accommodate the strain gradient and is then redistributed according to Orowan's equation [102] in relation to the shear strain increment throughout the body.

The redistributed mobile dislocation densities, in the form of the magnitude of the superdislocations on each slip system in each element, are used to calculate the elastic interaction forces among them using analytical solutions for the anisotropic elastic fields of parallel dislocation segments [80,93]. These are introduced as back stresses on each slip system, $\tau_b^{(\alpha)}$, resulting in the following modification to equation (3-1):

$$\dot{\gamma}^{(\alpha)} = \dot{\gamma}_0 \left(\frac{\tau_{eff}^{(\alpha)}}{g^{(\alpha)}} \right)^{1/m} sign\left(\tau_{eff}^{(\alpha)} \right) \tag{3-4}$$

where

$$\tau_{eff}^{(\alpha)} = \tau^{(\alpha)} - \tau_b^{(\alpha)} \tag{3-5}$$

For interactions with grain boundaries, the SD subroutine enforces a critical local stress for the absorption of dislocations at a grain boundary [93] or phase boundary as follows:

$$\tau_{obs}^{(\alpha)} = (1 - N^{(\alpha)})\tau^* \tag{3-6}$$

where $\tau_{obs}^{(\alpha)}$ is the obstacle strength for slip system α at which slip across a grain boundary occurs, and τ^* is the maximum obstacle strength. For 304 stainless steel, Shen et al. experimentally found τ^* to be approximately 5 time the macroscopic yield stress, and this estimate was adopted and applied to pure tantalum here [42]. N is a geometrical transmissivity factor of incoming dislocations on slip system α and is determined based on the SWC (Shen, Wagoner, Clark) 2nd Criterion [42]. The obstacle strength is incorporated into slip calculations for grain boundary elements by the following equations:

$$\tau_{eff}^{(\alpha)} > \tau_{obs}^{(\alpha)} \qquad \dot{\gamma}^{(\alpha)} = \dot{\gamma}_0 \left(\frac{\tau_{eff}^{(\alpha)} - \tau_{obs}^{(\alpha)}}{g^{(\alpha)}} \right)^{1/m} sign\left(\tau_{eff}^{(\alpha)} - \tau_{obs}^{(\alpha)} \right) \tag{3-7}$$

$$\tau_{eff}^{(\alpha)} \leq \tau_{obs}^{(\alpha)} \qquad \dot{\gamma}^{(\alpha)} = 0 \tag{3-8}$$

The equilibrium boundary value problem is solved in ABAQUS/Standard with the choice of constitutive models being implemented through user subroutines (UMAT). The solution of the equilibrium equation is implicit, but the coupling at each time step with the user subroutines is explicit. The SD model consists of two such subroutines:

1. A standard CPFEM model implemented in ABAQUS/Standard as outlined in [94].
2. A special meso-scale subroutine that updates dislocation densities on each slip system in each element — along with corresponding local slip resistances — based on Orowan's equation, computes the local back stress among dislocation populations from element to element, and computes the obstacle strength due to GBs or phase boundaries.

The only differences in the SD and CPFEM implementations, apart from different values for the hardening parameters, is the use of the second subroutine, which considers elastic interactions of dislocations, and redistributes dislocation densities according to Orowan's equation in order to accommodate plastic deformation.

3.2 Methods

3.2.1 Experimental Setup

Four hourglass shaped tensile specimens, shown in Figure 3-1, were machined from a rolled sheet of 99.9% pure tantalum obtained from Goodfellow Corporation; detailed information on these specimens and their deformation can be found in [52,103,104]. After heat treating the specimens at 2000 °C and ~10^{-6} Torr for 10 h in a vacuum furnace, the grains were millimeter-

sized, approximately columnar, and found to have negligibly low initial GND content. HR-EBSD found the average GND content to be 4.7×10^{12} m^{-2} using a 1 μm step size, which is approaching the lower bounds of HR-EBSD resolution [61]; this is indicative of a well annealed material. Specimens were polished to a mirror-like finish suitable for EBSD work [105]. The final thickness of specimen 1, 2, 3, and 4 after polishing was 0.94 mm, 0.93 mm, 0.94 mm, and 0.84 mm respectively. A region of interest (ROI) (refer to Figure 3-1), approximately 5 mm x 1.4 mm, was defined by scribe marks on its boundaries to assist with locating the ROI during imaging.

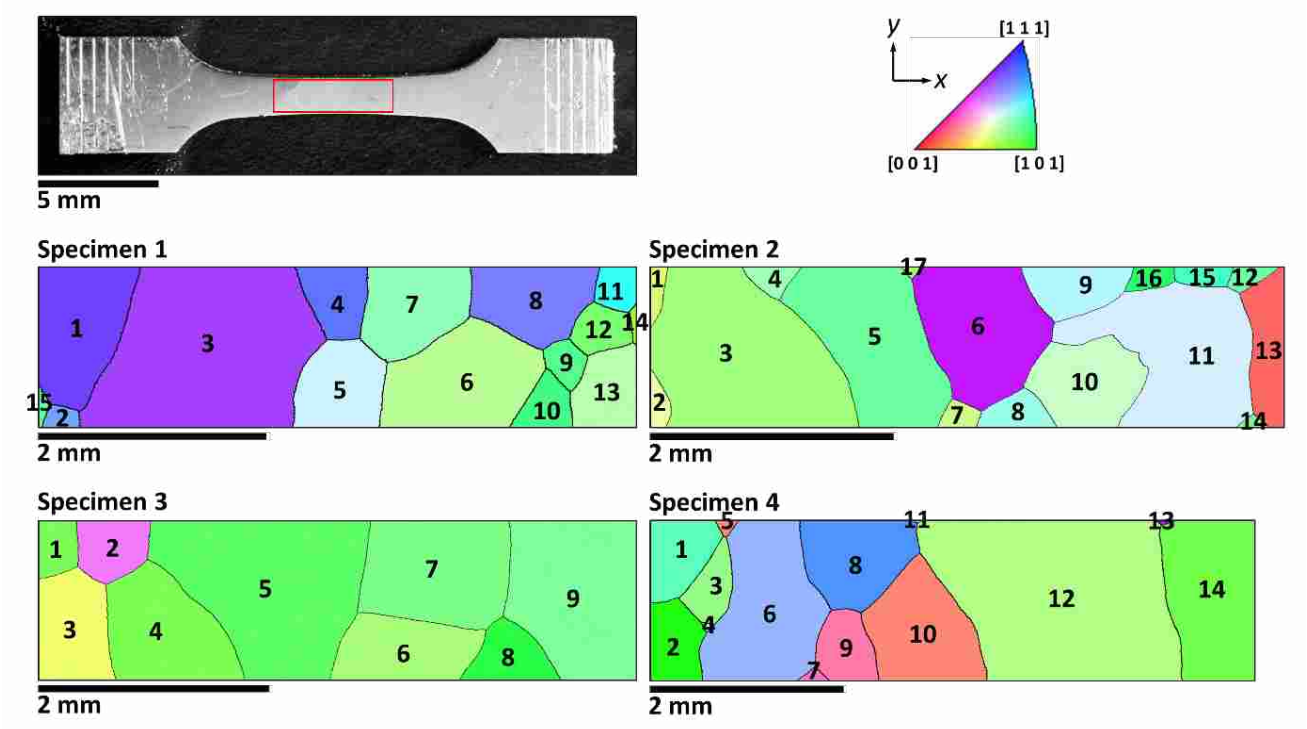

Figure 3-1: Photograph of the tensile specimen geometry used in this study and inverse pole figure (IPF) maps of the specimen ROIs before the samples were strained. The red box in the center of the tensile specimen indicates the location of the ROI. The IPF maps are shown with respect to the x direction and the orientations shown here are the average for each grain. The numbers inside of each grain indicate the grain number. Each grain's average orientation can be found in the Appendix A. Adapted from [42] with permission from Elsevier.

Tensile specimens were strained in several stepwise increments at a nominal strain rate of 10^{-4} s^{-1} for specimens 1 and 2, 10^{-5} s^{-1} for specimen 3, and 10^{-3} s^{-1} for specimen 4. The stress-strain response of each specimen is shown in Figure 3-2, and the samples were strained to the following strain levels: 6.8% strain for specimen 1, 19.2% strain for specimen 2, 5.2% strain for specimen 3, and 10% strain for specimen 4. Tensile tests on specimen 1, 2, and 4 were performed on a custom-built in situ load frame described in [106]. The pull from step 0% to 0.5% on specimen 3 was performed on a servo-hydraulic load frame with a 2000 lbf capacity load cell, while the pull from step 0.5% to 5.2% on specimen 3 was performed on a tabletop Instron 3345 single column universal testing system with a 500 N capacity load cell.

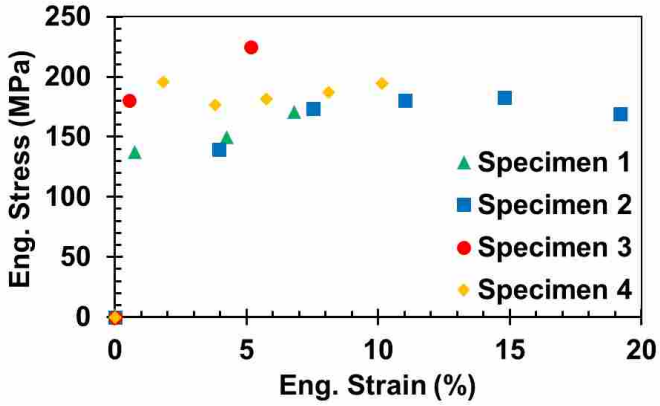

Figure 3-2: Measured stress-strain date for the four tensile specimens. The experimental data points are mapped as individual data points instead of continuous lines because the strain was calculated using digital image correlation (DIC) after straining (see [40–42]. Stress-strain data was collected at four strain levels for specimen 1, ε = 0%, 0.8%, 4.2%, and 6.8%; six strain levels for specimen 2, ε = 0%, 4.0%, 7.5%, 11.0%, 14.8%, and 19.2%; three strain levels for specimen 3, ε = 0%, 0.5%, and 5.2%; and six strain levels for specimen 4, ε = 0%, 2%, 4%, 6%, 8% and 10%. Adapted from [42] with permission from Elsevier.

Initial and final crystal orientations of the four tensile specimens were measured over the ROI by stitching multiple EBSD scans together. Average grain orientations for each specimen are

shown in Figure 3-1 and given in Appendix A. EBSD scans for specimens 1, 2, and 4 were taken using Channel 5 software (Oxford Instruments) on a Zeiss Supra 55VP field emission scanning electron microscope (SEM). The EBSD scan for specimen 3 was taken on an FEI Helios Nanolab 600 SEM using OIM DC 7.2 software (EDAX-TSL). Grain boundaries were defined by a 5° misorientation. EBSD scans were taken on specimen 1 and 3 with a 5 μm step size, and on specimen 2 and 4 with a step size of 4 μm.

All EBSD-based GND measurements in this study were calculated and plotted using OpenXY [78], an open-source software HR-EBSD package developed at Brigham Young University, following the methods described previously in section 1.1. Because EBSD patterns were not saved for specimens 1, 2, and 4, GND estimates were obtained using orientation based GND calculations. GND content was obtained from specimen 3 using HR-EBSD post processing with saved EBSD patterns. HR-EBSD was performed using the standard settings in OpenXY.

3.2.2 Simulation Setup

The entire gage section of tensile specimen 1 was meshed using C3D8 (8-node solid) elements as shown in Figure 3-3. The total number of elements for specimens 1 was 102,040. To better represent heterogeneous deformational behavior in the vicinity of grain boundaries, the following was done: 1) smooth grain boundaries were created using spline fitting and 2) finer mesh (~12 μm edge length) was adopted near grain boundaries while, for computational efficiency, the mesh was coarser for inner grain elements (~14 μm edge length). Although a fine mesh size with roughly cubic elements is preferred to accurately capture deformation patterns, only four through thickness element layers were used for computational efficiency. This number was arrived at via a sensitivity study considering 1, 3, 4, 5, and 7 element layers through the thickness direction; a

nearly negligible effect (<5% difference in average GND density at the surface layer) was observed when increasing the number of elements from 4 to 7. Columnar grains were assumed, as per [52,103,104]. Nodes on the left ends of each specimen were fixed in all directions while a prescribed displacement boundary condition along the positive x-direction was imposed at the nodes on the right ends.

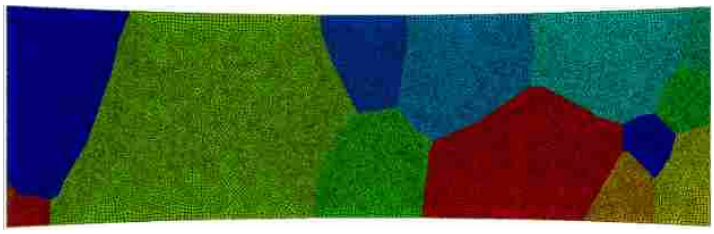

Figure 3-3: FE model of specimen 1

Three types of simulations were conducted on the specimen 1 mesh: the SD model (see section 3.1.1), a CPFEM (see section 3.1.1), and a combination of the SD model and a standard CPFEM, which will be denoted as SD*. Just like the SD model, SD* used single crystal hardening parameters which are thought to better reflect true single crystal behavior compared to those used in CPFEM (see section 3.1.1 for a description of these parameters). Unlike the SD model, SD* did not take into account elastic dislocation interactions with other dislocations or with GBs; i.e., the elastic forces that are responsible for back stress. Essentially SD* is the SD model with back stresses turned off. These three methods are summarized in Table 3-1

Table 3-1: Summary outlining the differences between the three simulation methods

Method	Hardening Parameters	GB Interactions
SD Model	Calibrated with SD Model	Yes
CPFEM	Calibrated with CPFEM	No
SD*	Calibrated with SD Model	No

The value of τ^* used in equation (3-6) for the SD model was taken to be 5 times the macroscopic yield stress of the tantalum oligocrystal sample, as per earlier work in this area [93,95], i.e., 575 MPa. The SD Model introduces no undetermined constants beyond those in a standard CPFEM scheme. That is, the strength and strain-hardening constitutive parameters must be determined in either case from single- multi- or polycrystal stress-strain curves. Several material parameters were adopted from the literature for tantalum as follows: anisotropic elasticity constants of C_{11}=267 GPa, C_{12}=161 GPa, and C_{44}=82.5 GPa and shear modulus of μ=70.7 GPa [104]. The initial dislocation density, dislocation generation parameter, and dislocation annihilation parameter, ρ_0, k_a, and k_b respectively, were fit the experimental stress-strain data. The best-fit parameters are listed in Table 3-2. The values of the three parameters vary between the SD model and CPFEM because the strong effect of elastic dislocation interactions in the SD model are ignored in the CPFEM. In all simulations, the total initial dislocation density ρ_0 was partitioned equally onto the 24 slip systems considered, 12 of type {110}<111> and 12 twelve of type {112}<111>; due to this equal distribution of dislocations, initial GND content was zero.

Table 3-2: Fit parameters used in the SD model, CPFEM, and SD*

Parameter	CPFEM	SD model / SD*
ρ_0 (m^{-2})	3.9×10^{13}	3.8×10^{13}
k_a	4.4	75
k_b (m)	$440b^{(*)}$	12b

*Burgers vector (b = 0.287 nm for Ta)

3.3 Results and Discussion

3.3.1 Experimental Results

GND density maps for all four specimens were created from experimental EBSD data, as described in section 3.2.1, and are presented in Figure 3-4. The maps showed that GNDs tended to cluster into features. Most notably GND pileups were formed at the GBs, but GND bands and intra-grain GND structures were also visible; GND structures were most visible in specimen 2, which underwent the most strain out of the four specimens. Dark blue regions within the GND density maps, shown to have a GND density of 1×10^{12} m^{-2}, indicate points where the diffraction pattern was of too poor of quality for an orientation to be resolved. These regions appeared in specimen 1, 3, and 4 due to surface damage, and in specimen 2 due to high levels of strain.

As previously mentioned, GNDs are necessary at GBs due to strain incompatibility [83]. In addition to incompatibility, the GB interface has been shown to act as a barrier to dislocation transmission [4,107–109]. Geometrically based transmission factors can be calculated to determine the ease or difficulty at which a dislocation could theoretically transmit across a GB. When dislocations intersect with a GB and are blocked, GNDs accumulate and their stresses

compound, developing into a back stress. To determine if the GB character, as expressed through GB transmission factors, correlated with GND pileup and consequently the associated back stresses, five parameters, N_m, λ, m'_m, Δg, and RBV_m, which describe the average transmissivity of GBs were calculated and then compared with the GND density of the GBs (see section 1.2 for a full description of these five parameters).

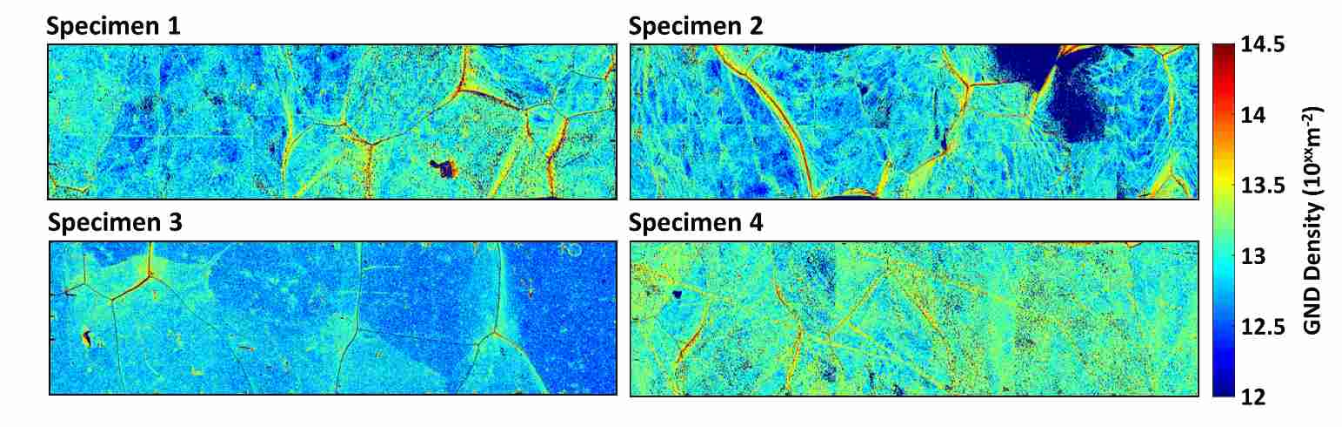

Figure 3-4: GND maps constructed using EBSD data for specimen 1 at 6.8% strain, specimen 2 at 19.2% strain, specimen 3 at 5.2% strain, and specimen 4 at 10% strain. Dark blue regions (1×1012 m-2) in the GND maps indicate points where the diffraction pattern was of too poor of quality for an orientation to be resolved.

Data was taken from GBs in specimen 1, specimen 3, and specimen 4, resulting in a total of 63 data points, one for each GB. Specimen 2 was not used for this GB transmission factor analysis because the sample was highly deformed, causing heterogeneous deformation and a large region of unreliable EBSD points; specimen 2 was, however, still included in visual analyses in this study, along with the other specimens, to demonstrate GND density substructure. Grains 11 and 13 from specimen 4 (see Figure 3-1) were also excluded from this analysis due to their small size at the edge of the sample, making it difficult to analyze a reasonably sized region near their

GBs. The normalized GB GND density, ρ_{GND}^{GB}, was tested for correlations with the transmission factors; it was defined as the average GND density within 25μm of both sides of the GB divided by the average GND density of both grains comprising the GB. By plotting average GND density as a function of the distance from the GB (see Figure 3-5), it was found that a distance of 25μm captured the pileup region of high GND density at the GB, and was therefore used as the definition of the GB region within this analysis. The GB average GND density was normalized by the grain average GND density for two reasons. First, the three samples used in the correlation were at differing strains, and an increase in strain naturally leads to a higher GND density. Second, this prevented GBs from showing a high GND density when in reality the entire grain had a high GND density. The five transmission factors, N_m, λ, m'_m, Δg, and RBV_m, are plotted against the normalized GB GND density, ρ_{GND}^{GB}, in Figure 3-6. The slope and the 95% confidence interval of a linear regression fit are shown as a solid line and dotted lines respectively; these parameters, along with the associated p value of the slope, are summarized in Table 3-3.

Three of the five grain boundary transmission factors evaluated, N_m, λ, and Δg, showed a statistically significant correlation with ρ_{GND}^{GB} — the p value for the slope of each of these transmission factors was less than 0.002. This indicates that there would be less than a 0.2% chance of obtaining a slope as large or larger than the one seen if there was in fact no correlation between the transmission factor and ρ_{GND}^{GB}. Both N_m and λ had a negative correlation with ρ_{GND}^{GB}, which is expected; higher values of these variables represent neighboring slip systems which are closely aligned, and would therefore be expected to have lower GND densities near the GB. Also, as expected, Δg had a positive correlation with ρ_{GND}^{GB}; neighboring grains with a high Δg are misaligned, and would be expected to have higher GND densities near the GB. Furthermore, the bounds on the 95% confidence interval for transmission factors that had a statistically significant

correlation with ρ_{GND}^{GB}, N_m, λ, and Δg, are consistently positive or negative, giving further indication that the correlation does exist. Although, m'_m and RBV_m did not appear to correlate with the GB GND density in this dataset, many studies have found both m' and RBV to be a useful parameters when evaluating individual slip transmission events at the GB [37,46,110,111]. Apart from the correlations of the transmission factors, it is important to point out the spread of data surrounding the fit line of every transmission factor in Figure 3-6. The several statistical correlations with ρ_{GND}^{GB} found in these plots does not translate into these transmission factors being predictors for ρ_{GND}^{GB}; it means that these transmission factors could be used to predict the *mean* ρ_{GND}^{GB} for a given transmissivity factor. The spread in data indicates that the geometric transmission factors explored are poor predictors as to whether an individual GB will experience GND accumulation or not. However, the statistical correlations are good evidence that some of these factors are likely influencing the average GND density of the total GB population within a sample.

Another notable feature of the correlation plots in Figure 3-6 was the five highest ρ_{GND}^{GB} values that appear to be outliers in each plot (see points within blue circle in Figure 3-6); it may look as if the significant correlations are mainly due to these outliers skewing the data. The five highest ρ_{GND}^{GB} values were examined and found to be GBs 5/6, 11/12, and 12/14 in specimen 1 and GBs 2/3 and 2/6 in specimen 3 (see Figure 3-1). The GND density maps in Figure 3-4 reveal that these GBs did indeed have visibly higher GND densities than other GBs in the specimens. No reasonable argument could be made for excluding these results from the analysis; however, to ensure that the correlations were not being skewed or solely determined by these outliers, a regression line was fit to the data with these five GBs excluded. The results are presented in Table 3-3, and they show that the correlations persist in spite of the removal of the outliers. In fact, the p values for the statistically significant transmission factors further decreased, while the p values

for the statistically insignificant values further increased. Future studies seeking to relate GND accumulation to geometric configuration may be aided by including a higher number of GBs or including complex interactions of multiple grains in the surrounding neighborhood. By understanding why one GB may accumulate more GNDs than another, developments in material design can be made which utilize the back stress associated with GNDs.

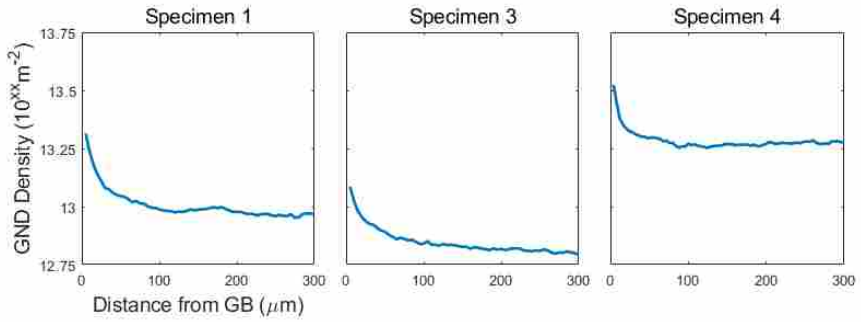

Figure 3-5: Average GND density as a function of the distance from the GB. Plots were created for specimen 1, 3, and 4 at strain levels 6.8% strain, 5.2% strain, and 10% strain respectively.

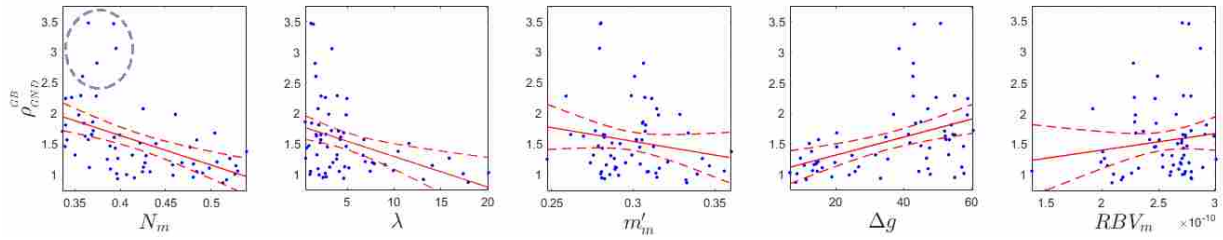

Figure 3-6: Scatter plots comparing the GND density within 25um from the GB and slip transmission factors associated with the ability of a dislocation to pass from one side of the GB to the other. The solid red line is a linear regression fit to the data. The dotted red line is the 95% confidence interval for the fit line. The slope of the fit line, the 95% confidence interval of the fit line, and the p value of the fit line given in Table 3-3. The low p value associated with N_m, λ, and Δg indicate that there is a statistically significant correlation between these transmission factors and ρ_GND^GB. The data was taken from GBs in specimen 1 at 6.8% strain, specimen 3 at 5.2% strain, and specimen 4 at 10% strain. The blue circle in the first plot highlights the outliers discussed in the manuscript. Because all plots in this figure have the same y axis, the same outliers are found in every plot.

Table 3-3: Slope, 95% confidence interval, and p value for the regression line fit to the transmission factors in Figure 3-6. All GBs Included includes all the points used to make the plots in Figure 3-6, while Outliers Removed has the five highest $\boldsymbol{\rho_{GND}^{GB}}$ values removed. The low p value associated with $\boldsymbol{N_m}$, $\boldsymbol{\lambda}$, and $\boldsymbol{\Delta g}$ indicate that there is a statistically significant correlation between these transmission factors and $\boldsymbol{\rho_{GND}^{GB}}$. Even with the outliers removed from the data, these same transmission factors have a statistically significant correlation with $\boldsymbol{\rho_{GND}^{GB}}$, while , $\boldsymbol{m_m'}$ and $\boldsymbol{RBV_m}$ do not.

All GBs Included					Outliers Removed				
Transmission Factor	Slope	95% Confidence Interval		p value	Transmission Factor	Slope	95% Confidence Interval		p value
N_m	-4.8	-7.0	to -2.6	5.4×10^{-5}	N_m	-3.4	-4.9	to -2.0	9.3×10^{-6}
λ	-0.050	-0.081	to -0.019	0.0019	λ	-0.031	-0.051	to -0.010	0.004
m_m'	-4.5	-11.0	to 2.0	0.17	m_m'	-1.4	-5.8	to 2.9	0.51
Δg	0.015	0.0068	to 0.023	4.6×10^{-4}	Δg	0.011	0.0062	to 0.016	3.3×10^{-5}
RBV_m	2.7×10^{9}	-2.2×10^{9}	to 7.5×10^{9}	0.27	RBV_m	1.1×10^{9}	-2.2×10^{9}	to 4.3×10^{9}	0.50

Apart from GND accumulation at the GBs, the GND density maps in Figure 3-4 show that GNDs also accumulated in intragranular features, most notably as bands in the highly strained specimen 2. These features are similar to dislocation cells but at a much larger scale. Dislocation cells are characterized as alternating structures of dense and non-dense dislocation densities. There have been many different sizes and types of cells observed throughout literature [86,112,113]. They are generally on the length scale of 250nm to 2500nm [92,114,115], however larger dislocation cells, up to 55μm, have been reported [116]; the cell size is highly dependent on the resolution with which they are measured [32,117]. The step sizes used in this study — 4um to 5um — were so large that it is impossible to see small dislocation cells [32,117]. It is apparent, however, that dislocation structures emerged in our large grained specimens. Like dislocation cells, the GND density features seen in the large grained specimens appeared to increase in magnitude as the strain increased, making them clearly visible in the highly strained samples. In contrast, it is difficult to distinguish any features from the noise of the background in the less strained samples. Similar to

dislocation pileup at GBs, these cells or bands of high GND density cause an internal back stress that contributes to hardening [86].

To further visualize dislocation structures, and the effect they may have on the back stress and intragranualr stresses of the samples, the sign of the individual components of the Nye tensor, as calculated from EBSD and HR-EBSD data, were examined [117]. The Nye tensor, $\boldsymbol{\alpha}$, quantitatively represents the total GND content thru a second rank tensor. As mentioned in section 1.1, only the α_{i3} components, can be fully determined from surface EBSD methods [24,33]. As can be seen from (1-1), each component of the Nye tensor is composed of GND density from a variety of slip systems, and each slip system contributes to the different components of the Nye tensor in different amounts depending on its orientation. Dislocations of a similar sign contribute to the Nye tensor, while dislocations of opposing sign do not; this is essentially the definition of GNDs vs SSDs. The individual components of the Nye tensor can be either positive or negative depending on the sign of the dislocations that contributed to that component. Figure 3-7 plots the α_{13} component of the Nye tensor from specimen 1 in both the unstrained and strained state. This particular specimen and Nye tensor component were arbitrarily chosen, and other specimens and components of the Nye tensor show similar trends; for completeness, the three known components of the Nye tensor from all four tensile specimens are mapped out in Appendix B. The most notable feature in the maps was the grouping together of dislocations of the same sign — the unstrained sample started out with dislocations of both positive and negative sign homogenously distributed but as the sample deformed, dislocations of the same sign appeared to cluster together. This clustering occurred at high GND density locations and was the cause of the previously mentioned GND structures, i.e. GB pileups and intragranular structures. Additionally, the Nye tensor map allowed for the visualization of GND structures that were difficult to identify in the standard GND

map, appearing only as homogeneous GND density distributions (see regions indicated by red arrows in Figure 3-7). Clustering of dislocations of the same sign is necessary in order to maintain lattice continuity throughout deformation [87], this results in localized orientation changes. When GNDs of the same sign accumulate, the elastic stresses they cause also accumulate, thus producing a potentially large back stress. The increasing size of the same signed features is therefore indicative of an increasing back stress from these features. While the idea that heterogeneous dislocation structures induce a back stress has been previously explored [86,118], plotting the individual components of the Nye tensor and their sign allows for easier visualization and identification of substructure than traditional EBSD based GND density maps. Further studies using this method in conjunction with more interrupted trials could help develop a clearer picture of the evolution of GND density from a homogenous state into a more structured state.

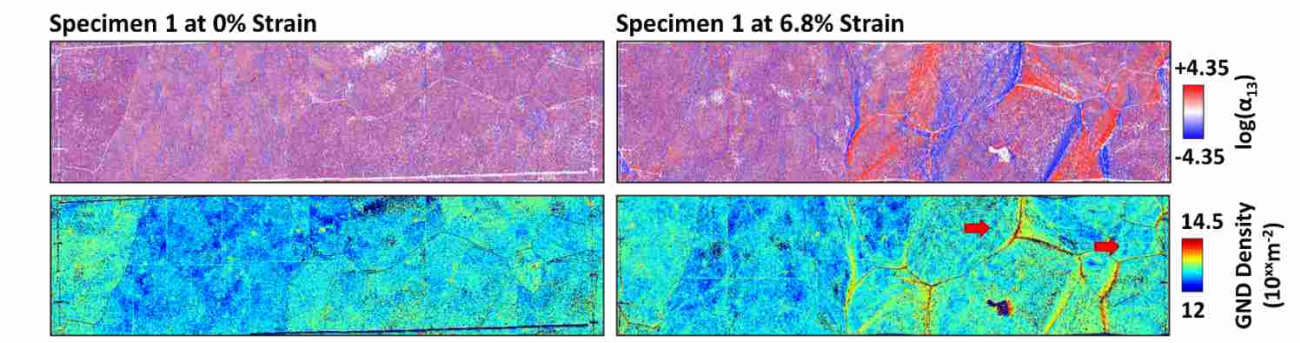

Figure 3-7: The α13 component of the Nye tensor from specimen 1 at 0% strain (upper left) and 6.8% strain (upper right). The strained sample shows GNDs of the same sign grouping together. GND density appears homogeneous in several regions (indicated by red arrows) in the GND density map for specimen 1 at 6.8% strain (lower right), while the α13 map reveal GND structures in these same regions. The combined elastic distortion fields of the GNDs are a source of back stress.

3.3.2 Simulation Results

In order to investigate the back stress at the macroscale, stress-strain curves were analyzed from the experiments and several crystal plasticity-based simulations. As outlined in section 3.2.2, the deformation of specimen 1 was simulated using three simulation methods: a standard CPFEM, the SD model, and SD*. Details regarding the three different methods are found in sections 3.1.1 and 3.2.2, and a summary can be found in Table 3-1. A stress-strain plot of specimen 1 created using results from the experiment and these three simulation methods is presented in Figure 3-8. Both the SD model and CPFEM followed the experimental stress-strain curves, while the SD* stress-strain curve was notably lower than the other two simulation methods. While neither CPFEM nor SD* include backstress, CPFEM is still able to predict the correct stress-strain behavior because its hardening parameters are combination of dislocation hardening, elastic dislocation interactions, and grain boundary effects. The addition of back stress in the SD model give it the necessary hardening to predict the correct stress-strain response while using hardening parameters which are assumed a more accurate reflection of true single crystal hardening parameters than those in the CPFEM. Too low of a stress in the SD* simulation can possibly be attributed to the lack of backstress in both the model and in the hardening parameters.

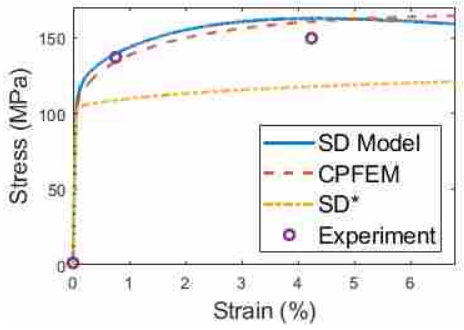

Figure 3-8: Engineering stress and engineering strain response for specimen 1.

Because the only difference between the SD model and SD* was the elastic interactions of dislocations, the difference in stress between these two methods was essentially the back stress, including that caused by GB obstacles to dislocation motion. Therefore, the following equation for back stress was used in this analysis:

$$\sigma_b = \sigma_{SD} - \sigma_{SD^*} \tag{3-9}$$

where σ_{SD} is the flow stress calculated by the SD model and σ_{SD^*} is the flow stress calculated by SD*. The back stress is plotted as a function of the true strain in Figure 3-9 (B). The contribution of back stress to the total flow stress (i.e. the ratio of back stress divided by flow stress) is plotted as a function of engineering strain in Figure 3-9 (A). Ashby found that at small strains GNDs dominate the total dislocation density, but as strain increases they are overcome by SSDs [83]. This initial increase in GNDs is evident as a corresponding initial increase in back stress contribution in Figure 3-9. Throughout the strain, back stress was seen to make up, on average, approximately 25% of the flow stress. After the initial increase in back stress contribution, there was a plateau and even a slight decrease; this can be attributed to the outnumbering of GNDs by SSDs after the initial stages of strain, resulting in the back stress-causing GNDs to have a diminishing impact on hardening. Studies by Feaugas and others using unloading tests found similar back stress trends [85,86,119,120], i.e. a rapid increase in back stress early on, followed by a tapering out (see Fig 10 (B). The value at which the back stress plateaued out, approximately 40 MPa, was well within a reasonable range of back stress; other studies have reported back stresses ranging from 20 MPa to 700 MPa depending on the material and microstructure (various types of steels and coppers were explored) [85,86,119–121], and one study found that coarse grained steel had a lower back stress than a steel with fine grains [85]. A back stress on the lower end of this range is expected, considering the grains were very large and the maximum stress was 162 MPa.

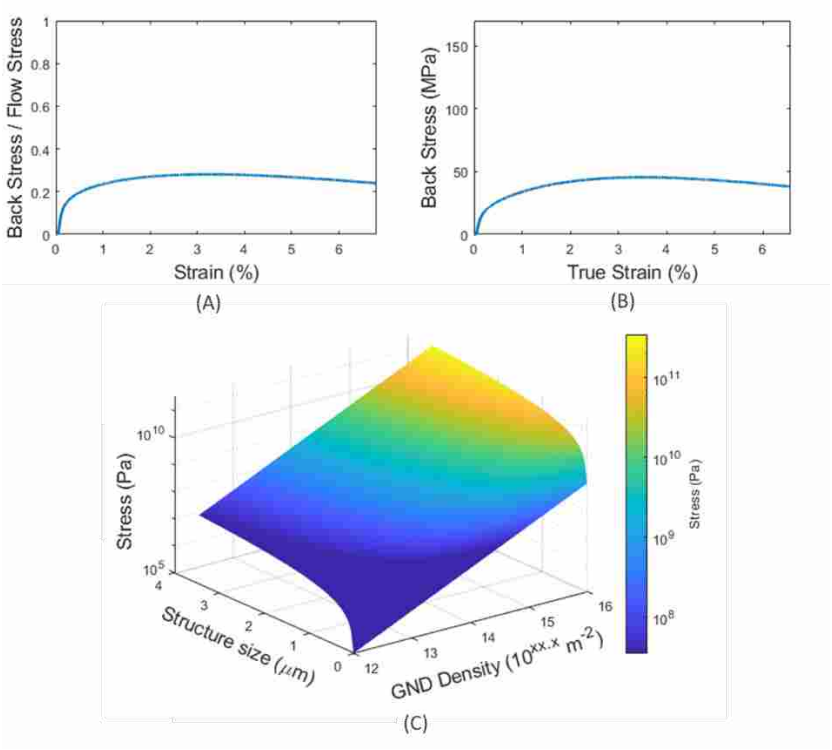

Figure 3-9: (A) Contribution of back stress on flow stress (σb/σf) as a function of strain for specimen 1. (B) Back stress as a function of true strain for specimen 1. (C) Internal stress produced by a uniform distribution of GNDs within a square area.

Additionally, an analytical solution for the stress caused by a uniform distribution of GNDs [36,122] is shown in Figure 3-9 (C). An internal stress of 40 MPa would require a GND structure of 40 nm square with a GND density of $1\times10^{14}m^{-2}$ — a condition which could very well be obtained within a dislocation cell wall or GND band. For reference, cell wall thickness ranging from 8 nm to 3500 nm have been reported in stainless steel and aluminum alloys [86,113,123,124]. Although the macroscopic back stress is generally smaller than the internal stresses and related to the distribution of internal stresses [86], this analysis gives some indication of the internal stress magnitudes that can be produced by dislocation structures like the ones previously discussed; the wide range of values are not meant to be a typical representation of any particular microstructure. The decrease in back stress after the plateau is not a normal feature of back stress and should be

noted. This appears in the plots due to the decrease in stress in the SD model, i.e. necking. While using the true stress to calculate a backstress instead of the engineering stress would both eliminate this decrease in back stress and be more representative of actual back stress values, only the engineering stress was available.

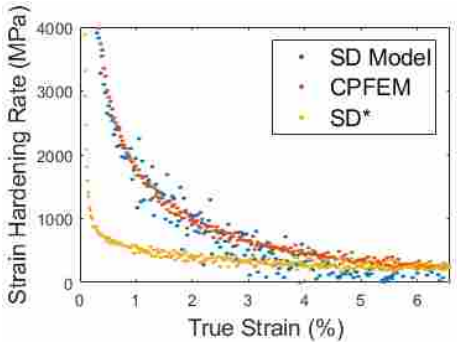

Figure 3-10: Strain hardening rate ($d\sigma_t/d\varepsilon_t$) vs true strain for specimen 1.

Additionally, the strain hardening rate is plotted as a function of true strain for all three simulations in Figure 3-10; the strain hardening rate was defined as

$$\Theta = d\sigma_t/d\varepsilon_t \tag{3-10}$$

where $d\sigma_t$ is the change in true stress, and $d\varepsilon_t$ is the change is true strain. Figure 3-10 shows that the SD model has a higher strain hardening rate compared to SD* for the first several percent strain. This difference was largest at very low strains where the back stress-causing GNDs had the largest effect on hardening. Because SSDs are included in all models, it seems reasonable to assume that the strain hardening rate began to converge for all three models at the later stages of strain as the SSDs dominated the dislocation density, as discussed in the previous paragraph, and caused hardening via a friction stress. It is important to note that while CPFEM and the SD model

both produced the correct strain hardening rate, they likely achieved this through different means. The SD model explicitly models a back stress, while the back stress effects are contained in CPFEM through its hardening parameters.

3.4 Conclusions

The current study examined GND evolution and its impact on back stress and hardening in large grained tantalum samples through experimental and simulated methods. Four large grained tantalum tensile samples were strained, EBSD data was collected, and GND maps of the four specimens were produced. Deformation of one of the specimens was simulated using three different modeling approaches, and the stress-strain response was recorded. Analysis of this work revealed the following conclusions:

- Geometrically based GB transmission factors based on Livingston and Chalmer's N factor, Werner and Prantl's slip transfer number, and GB misorientation show a correlation with GND density within the vicinity of the GB. These correlations support the idea that GBs with misaligned slip systems accumulate higher GND content than those with closely aligned slip systems. Additionally, other factors, such local strain or neighborhood information, are likely needed in determining whether a GB will experience GND pileup.
- As a specimen undergoes deformation, the sign of individual components of the Nye tensor tends to spatially segregate, revealing clusters of the same sign in regions of high GND density. Stresses from dislocation structures of the same sign have a cumulative effect, and can produce a long range stress or back stress. Furthermore, plotting Nye tensor maps visually reveals GND substructure that is lost in EBSD based GND maps or only appears as a homogeneous distribution of GNDs.

- By simulating a CPFEM incorporating dislocation back stress and one that does not, back stress can be isolated from the total flow stress. Back stress was found to account for approximately 25% of the flow stress in the specimen simulated; i.e. the lack of back stress in the SD* simulation caused stress predictions to be 25% too low. The simulations were also a confirmation of Ashby's conclusions that GNDs dominate the initial stages of the stress response and SSDs dominate the latter stages.

4 A STATISTICAL ANALYSIS OF GB TRANSMISSIVITY IN POLYCRYSTALLINE TANTALUM

4.1 Background

The principle mode of plastic deformation in metals is dislocation slip, and a material's strength is often due to its ability to impede dislocation slip. Microstructural features which impede dislocation slip include forest dislocations, grain boundaries (GBs), solute atoms, and second phase particles. Both statistically stored dislocations (SSDs) and geometrically necessary dislocations (GNDs) produce a local friction-type stress as they interact with these features [1–3]. GNDs are also able to produce a back stress [4,5] due to the additive nature of their associated stress fields [1].

Back stresses produced by GNDs are elastic long-range stress which act as an additional resistance to dislocation slip; they are essentially able to reduces the resolved shear stress by producing stresses which act in an opposing direction [3,6,7]. This leads to kinematic hardening. The magnitude of the back stress is related to the density of GNDs [8], therefore better understanding of GND evolution also provides insight into the back stresses involved in hardening.

GNDs frequently accumulate at obstacles to dislocation slip, such as the microstructural features previously mentioned [5]. This study focuses particularly on GBs as obstacles. There are two explanations which describe why GNDs are often found at the GB. While they are both based in the idea that grains which are more similar in orientation tend to not accumulate GNDs, the two perspectives present GND accumulation at the GB via differing phenomena.

The first explanation originates from Ashby who demonstrated that varying crystallographic orientations in neighboring grains leads to non-uniform deformation and the requirement of strain gradients, and hence GNDs, in order to maintain compatibility at interfaces [4,9]; i.e. similar oriented grains do not require a strain gradient, or GNDs, at the GB because they undergo similar deformation. Essentially, GNDs are needed to maintain continuity such that gaps do not form between grains and grains do not overlap.

The second explanation is that dislocations are generated, move toward GBs, are blocked at GBs due to misaligned slip systems, and then accumulate there until the pileup produces enough back stress to transmit the dislocations across the GB. If a GB consists of similarly oriented grains, their slip systems align, the stress required to transmit the dislocations is low, dislocations can easily pass through the GB. Because both of these explanations describing why GNDs pileup at the GB center around the relative orientations of grains, it is difficult to separate the two explanations. This study focuses on the second explanation — dislocations are blocked at the GB, then GNDs accumulate — and particularly, on studying established parameters which describe the ability of a GB to block or transmit dislocations.

Multiple orientation-based transmission factors, or transmissivity parameters, have been described over the years [10,11]. They quantify the difficulty or ease with which a dislocation is transmitted from a slip system in one grain to another slip system in a neighboring grain, and they assume that dislocation transmission from one slip system to another is more difficult when the slip systems are misaligned. In addition to orientation-based transmission factors, it is thought that the geometric morphology of the grains and GB can affect dislocation accumulation at the GB; these will be referred to as geometric-based parameters throughout. Details and background on many orientation-based and geometric-based transmissivity parameters are given in section 1.2.

This paper undertakes a statistical analysis of a large number of grains, GBs, and TJs in order to better understand how grain properties and GB transmissivity parameters affect the GND density in grains, GBs, and TJs. By understanding these effects, microstructure can be better tailored to one's desired properties.

4.2 Methods

4.2.1 Experimental Setup

An hourglass shaped tensile specimen, shown in Figure 4-1, was cut using wire EDM from a plate of 99.997% pure polycrystalline tantalum obtained from HC Stark Inc. The plate was processed using a series of specialized rolling methods and annealing [28]. The specimen was polished to a mirror like finish suitable for EBSD work, and an initial EBSD scan of the sample was taken (see Figure 4-1). Analysis of the data using OIM Analysis 8.0 (EDAX) found the grain sizes to be roughly consistent with a mean of 68 μm and a standard deviation of 31 μm (see Figure 4-3). Further analysis found the distribution of GB misorientation angles relatively uniform with a slight tendency for low disorientations; Figure 4-2 compares the GB misorientation distribution of the material to that of a perfectly uniform distribution. An IPF map of the specimen gauge section in Figure 4-1 (plotted relative to the rolling direction and the tensile direction) revealed that the <110> direction in many of the grains was aligned with the rolling direction; this α-fiber texture typical of processed BCC metals. Complete details of chemistry, processing, and microstructure of the tantalum plate from which this sample was taken used can be found in [28]. HR-EBSD of the unstrained sample revealed a largely uniform GND distribution with an average of 2.3×10^{13} m^{-2}.

The sample was strained to 4% engineering strain at a strain rate of $8.15\times10^{-5}s^{-1}$ using a servo-hydraulic load frame; this level of strain was explored because it yielded sufficient sub-grain dislocation features to perform a statistical analysis but not too many such that the data was noisy. The sample was then mounted in epoxy, ground flat, and then re-polished for EBSD; approximately 60 μm of material was removed throughout grinding and polishing, after which a final EBSD scan was taken.

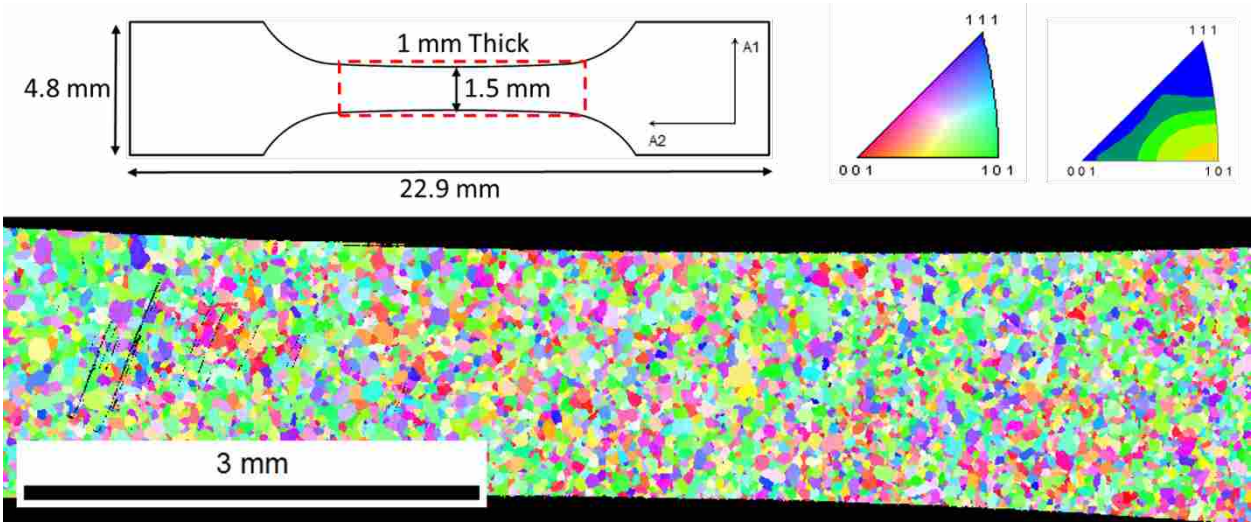

Figure 4-1: (Top Left) Geometry of the tensile specimen used. The dashed red lines indicate where the EBSD scan in the lower portion of the image was taken from. (Bottom) IPF map in the A2 direction (also the tensile direction and rolling direction) constructed from a montaged EBSD scan with a step size of 1 μm. (Top Right) A texture analysis shows that a large portion of the grains have their <110> directions aligned with the A2 direction.

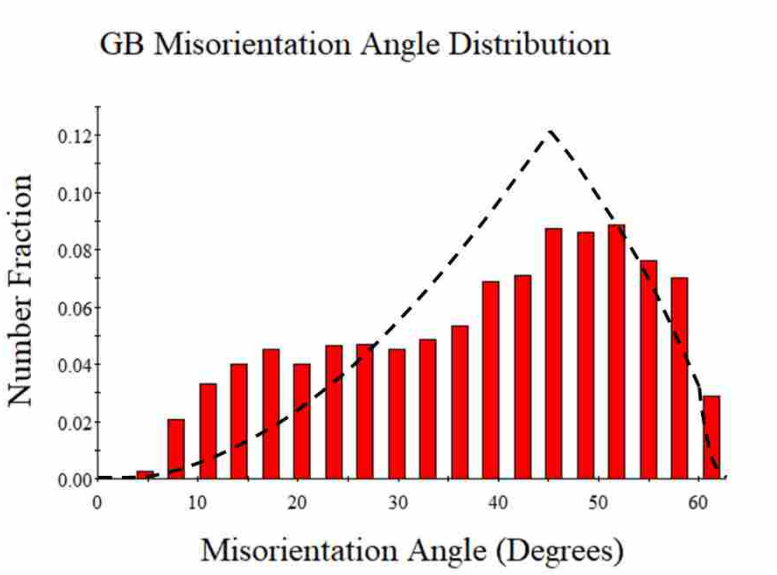

Figure 4-2: GB misorientation distribution of GBs of the tensile specimen. The dashed line is the MacKenzie distribution which represent the probability density of randomly distributed misorientations [29].

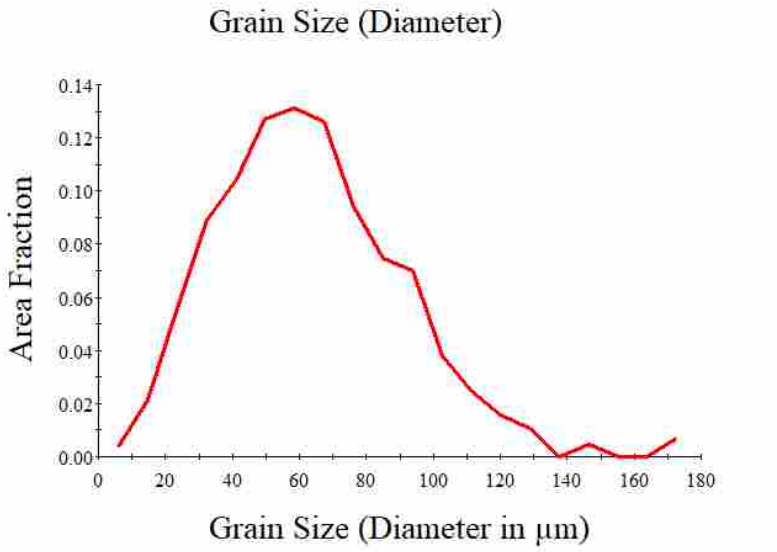

Figure 4-3: Grain size distribution in the tensile specimen.

4.2.2 EBSD Data Collection and GND Calculations

EBSD data was taken at the center of the gauge length of the tensile specimen, and the location of the scan is depicted in Figure 4-4. A 1 μm step size was used; this is an appropriate step size to capture reliable GND densities and spatially resolve sub-grain GND features [30]. EBSD data was collected on a Zeiss Supra 55VP field emission scanning electron microscope (SEM) using Aztec 3.1 (Oxford Instruments) at 20kV accelerating voltage, a 70° tilt, low gain, and with an exposure time of 87.72 ms. These settings produced very good EBSD patterns: over 99% of the scan points in the scan were able to be indexed. Patterns were saved for post processing as 672×512 pixel uncompressed tiff images (see Figure 4-5). EBSD data was minimally cleaned — less than 1% of points were cleaned — in order to clearly define GBs, while raw EBSD data was used to calculate GND densities. GND density measurements were calculated and plotted using OpenXY [31], an open-source software HR-EBSD package developed at Brigham Young University. OpenXY calculates the deformation tensor using cross-correlation methods and then calculates the GND density following the methods described in section [UPDATE]. Cross-correlation was performed using an annular pattern of 50 ROIs at a size of 25% of the EBSD pattern and the standard band pass filter settings in OpenXY [32,33].

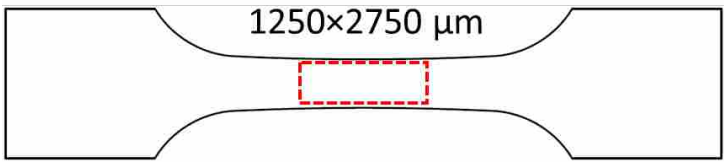

Figure 4-4: Approximate location of ROI on tensile specimen

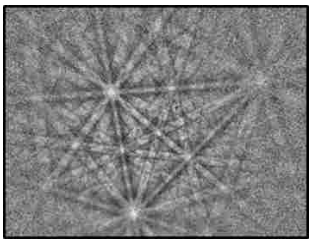

Figure 4-5: This pattern is from the EBSD scan evaluated in this study, and its quality is typical of those used the analysis.

4.2.3 Definitions for Grains, GBs, TJs and Their Associated Parameters

Three distinct regions — grain interior, GB region, and TJ region — were used to define every point on the sample surface. The regions were chosen to not overlap in order to separate which parameters are affecting which regions of the grain. The average GND in the grain interior, GB region, and TJ region were calculated using MATLAB and are identified throughout this paper as the "grain GND", "GB GND", and "TJ GND" respectively. GBs were determined using OIM analysis with a 5° tolerance angle; i.e. neighboring points with a misorientation angle less than 5° were considered to be part of the same grain. The size of the GB region was determined to extended 5 μm into the grain. This GB size was determined by visually inspecting and finding that a large majority of the GB features were within 5μm from the GB; examples of this can be seen in Figure 4-8, particularly in image A3. Similarly, the size of the TJ region was determined to have a radius of 5μm.

All parameters in this study, including GB and TJ parameters, considered 24 slip systems, 12 of type {110}<111> and 12 twelve of type {112}<111>. Additionally, all parameters were calculated using the grain average orientation. OIM Analysis was used to calculate the grain size, shape, position, and Taylor factor for the grain. An in-house MATLAB code was used to define the maximum Schmid factor. The grain parameters presented in Table 4-1 were calculated for all

grains. Any grain that contained less than 25 points was not considered for analysis. The final dataset used in the statistical analysis of grains contained 1989 grains.

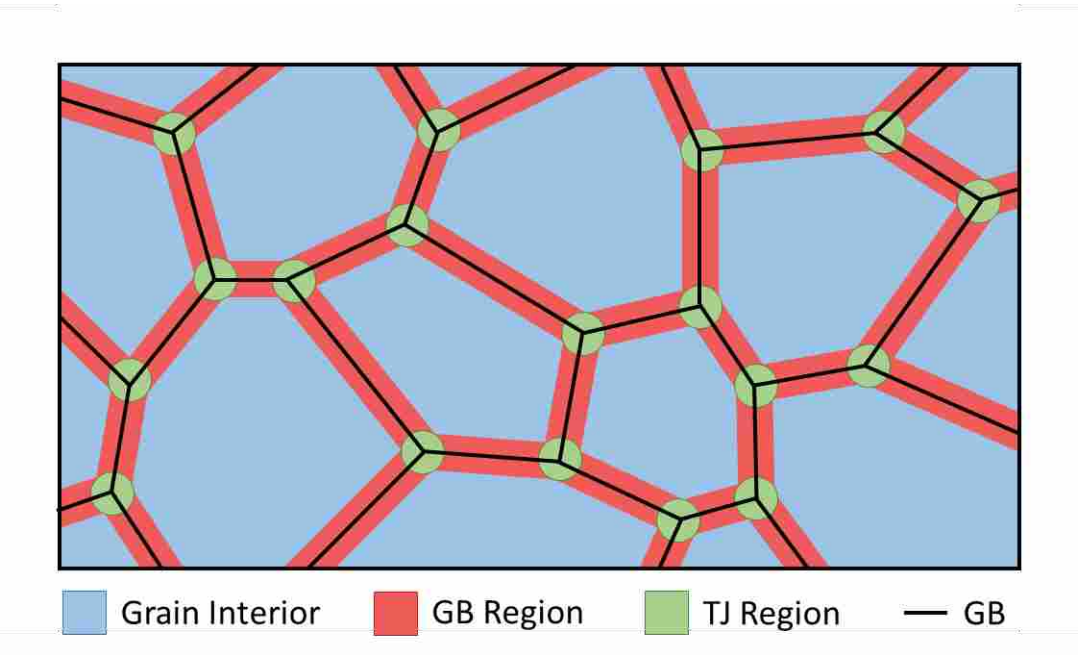

Figure 4-6: Diagram showing how grain interior regions, GB regions, and TJ regions were defined in this study.

Table 4-1: Parameters describing grains.

Parameter	Description
m	Maximum Schmid factor in the grain
M	Average Taylor factor in the grain
gs	Grain size diameter
ar	Aspect ratio
ma	Major axis angle

All GB parameters were calculated in MATLAB, and these parameters are summarized in Table 4-2. Any GB that was found to be too curvy or too short was excluded from this study

because it was felt that some of the GB measurements would be unreliable. Additionally, any GB that was composed of a grain that was smaller than 200 points was not used in analysis; because these grains were so small, the 5μm GB region extended relatively far into the grain's interior, covering a much larger portion of the grain than one would normally consider to be the GB. A total of 3519 GBs were considered for the statistical analysis.

Table 4-2: Parameters used to describe GBs and TJs. When these parameters are describing a TJ, they the average of the GB parameters from the three GBs that intersect to make up the TJ

Parameter	Description
trace_angle_abs	Absolute value of trace angle of GB
m_sum	Sum of the Schmid factors of the two grains making up the GB
m_diff	Difference between the Schmid factors of the two grains making up the GB
M_sum	Sum of the Taylor factors of the two grains making up the GB
M_diff	Difference between the Taylor factors of the two grains making up the GB
N_avg	Average N factor from all slip system combinations
N_m	Average N factor weighted by the Schmid factor
N_3	Average of top 3 N factors with high Schmid factors
N_1	Highest N factors within top 5 Schmid factors
lambda	Slip transfer number
mp_avg	Average of geometric compatibility factor from all slip system combinations
mp_m	Average geometric compatibility factor weighted by the Schmid factor
mp_3	Average of top 3 geometric compatibility factors with high Schmid factors
mp_1	Highest m' factors within top 5 Schmid factors
delta_g	Misorientation angle
rbv_avg	Average residual Burgers vector from all slip system combinations
rbv_m	Average residual Burgers vector weighted by the Schmid factor
rbv_3	Average of top 3 residual Burgers vector with high Schmid factors
rbv_1	Lowest N factors within top 5 Schmid factors
gs_sum	Sum of the grain sizes of the two grains making up the GB
gs_diff	Difference between the grain sizes of the two grains making up the GB
ar_sum	Sum of the aspect ratio of the two grains making up the GB
ar_diff	difference between the aspect ratio of the two grains making up the GB
ma_sum	Sum of the major axis angle of the two grains making up the GB
ma_diff	Difference between the major axis angle of the two grains making up the GB

All TJ parameters were calculated by averaging the GB parameters from the three GBs that intersected to make up the TJ, and these parameters are summarized in Table 4-2. Similar to GBs, any TJ that was touching a grain that was smaller than 200 pixels was not used in this study. Additionally, if any of the GBs comprising the TJ did not extend more than 2μm from the TJ, that TJ was not included in the study. A total of 3207 TJs were used in the statistical analysis.

4.2.4 Statistical Methods

Several statistical parameters were used throughout this study to gauge the correlation between GND density and the character of the grain, GB, or TJ structure. An example which uses the parameters discussed in this paragraph is given in Figure 4-7 and Table 4-3. A description of statistical terms and parameters, as well as one addition parameter, used throughout the analysis and discussion are given here; many details on the statistical parameters used are omitted, and a more thorough explanation should be sought elsewhere if they are not understood ([34,35] are good introductory resources).

- Response variable - Also known as the dependent variable, the response variable generally depends on the explanatory variable. It is usually the y value in a correlation plot. In this study it is the average GND of the feature being studied, i.e. grain GND, GB GND, or TJ GND.
- Explanatory variable - Also known as the independent variable, the explanatory variable is generally used to explain or predict the response variable. It is usually the x value in a correlation plot. In this study it is a parameter describing a grain, GB, or TJ.

- Interquartile Range (IQR) - This is the range of a dataset, excluding the bottom and top quarter of the data. This study uses the IQR of grain, GB, and TJ parameters in order to normalize their impact on GND.
- Simple linear regression - This is a statistical approach to finding a linear relationship between an explanatory variable and a response variable. This is done by fitting a straight line to the data such that the error between the response variable and the fit line is minimized. It yields a slope, intercept, and various goodness of fit parameters.
- Slope - The slope of the linear regression gives the relationship between the explanatory variable and the response variable. In this paper it is a representation of the impact of a parameter describing a grain, GB, or TJ on the grain GND, GB GND, or TJ GND, respectively. Because the many parameters in this study are of different orders of magnitude, their slopes cannot fairly be compared against one another; e.g. rbv_3 has an IQR or 1.16E-10, while gs_sum has an IQR of 2.79E1. To account for this, a relative slope is calculated by normalizing the slope of the linear fit by the IQR, i.e. multiplying the slope by the IQR. This new relative slope gives an estimate of how much the GND density will increase or decrease over the IQR of this dataset.
- Population - The population consists of every possible observation that could be made. For example, if a study is looking at the height of adult males, the population would consist of the heights of all adult males in the world. In this paper the population consists of all grains, GBs, or TJS from similarly processed pure Ta under the same load condition.
- Confidence Interval - The confidence interval of a slope is the range in which the true slope of the population mean likely exists. In this study the population mean is the population mean of grain GND, GB GND, or TJ GND.

- Prediction Interval (PI) - The prediction interval gives a range in which 95% of individual instances — in this case grain GND, GB GND, or TJ GND values — are predicted to fall.
- Impact Factor - The impact factor is the smallest relative slope within the 95% CI. It is a lower bound estimate of how much the grain GND, GB GND, or TJ GND changes with respect to a given grain, GB, or TJ parameter — not just in the grains, GBs, or TJs observed in this data set but in the entire population.
- p-value - The p-value is a measure of the statistical significance of the analysis. A short example is presented here to describe the interpretation of the p-value of the calculated slope in a regression analysis. In this example a linear regression between a GB parameter and GB GND yields a slope and an associated p-value of 0.0005. The p-value for this slope indicates that there is a 0.05% probability of seeing a slope as steep or steeper than the one observed in our data set, if in fact there was no correlation between the GB parameter and the population mean of the GB GND.
- Statistical Significance - A p-value below the predetermined significance level indicates that there is statistical significance; the common value of 0.05 is adopted for the significance level in this study. A short example is presented here to describe the interpretation of statistical significance. In this example a linear regression between a GB parameter and GB GND yields a slope and an associated p-value. If the p-value is above 0.05, the correlation is not statistically significant, and it cannot be said that the GB parameter correlates with GB GND. Any p-value above 0.05 indicates that the null hypothesis — in this case the GB parameter does not correlate with GB GND — cannot be rejected. If the p-value were less than 0.05, the correlation would be statistically significant, and we can conclude that there is a statistically significant correlation between the GB

parameter and GB GND at the 95% confidence level. Any p-value below 0.05 indicates that the null hypothesis can be rejected and alternative hypothesis can be accepted — in this case the GB parameter does correlate with GB GND.

Using a linear regression, correlations between grain GND, GB GND, and TJ GND and all grain, GB, and TJ parameters given in Table 4-1 and Table 4-2 were explored in this study. The data in Figure 4-7 and the values in Table 4-3 serve as an example to help understand the statistical parameters used throughout the analysis in this study. Columns highlighted in green in Table 4-3 are the values reported throughout this text, and columns highlighted in yellow are additional values reported in the appendix. The individual data points, the slope of a linear regression, it's 95% CI, and the PI are plotted on two sets of data, A and B. The fit line represents the predicted population mean of the GND density. Any line that can fit between the dotted lines is within the 95% confidence interval, and has a good chance of representing the population mean of the GND density. The PI gives the range in which 95% of individual instances are predicted to fall. The table shows that although data set B has a much more statistically significant correlation, i.e. lower p-value, with data set B than A, data set A is likely to have a larger impact on GND density, as indicated by a higher impact factor. This demonstrates that it is important to know both the p-value and the impact factor to understand the relationships described in this study. The p-value is a good measurement of the statistical correlation between the datasets, and the impact factor is a good measurement of the practical significance of that correlation. Even if something has a strong statistical correlation, like data set B, it can have a small practical effect on GND, i.e. it may hardly affect the actual value of the GND.

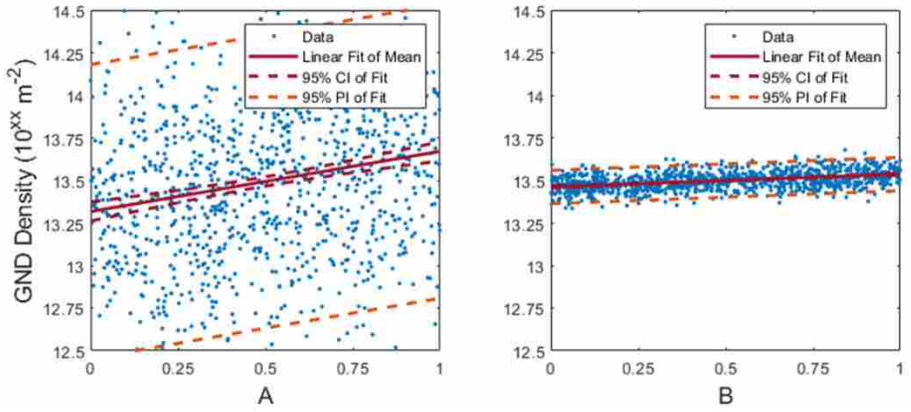

Figure 4-7: Example data demonstrating slopes and confidence intervals found using linear regression.

Table 4-3: Table demonstrating the statistical parameters in Figure 4-7

Parameter	Impact on GND	R^2	p-value of Correlation	Parameter Rank	Slope +/- 95% CI	Relative Slope +/- 95% CI	Interquartile Range
A	0.120	0.048	2.6E-12	1	0.354 +/- 0.098	0.167 +/- 0.046	0.471
B	0.033	0.168	8.6E-42	2	0.076 +/- 0.010	0.039 +/- 0.005	0.512

4.3 Results and Discussion

4.3.1 Subgrain GND Density Features

Before statistical analysis was performed on the data, the GND density was visually inspected to identify prevalent morphological features, some example of which are given in Figure 4-8. The most prevalent morphological features were GND bands which jetted out from the TJs. A clear example of this can be seen in images B3 and C2 of Figure 4-8 (future references to images within this section are referring to Figure 4-8). Many variations of these bands appeared at TJs, but it could not be visually determined which type of bands were most prevalent and what was

causing them. Some variations include bands that are parallel to the GB intersecting the TJ (image B2), bands that appear to come out of the TJ at the same angle as the opposing GB (image B3), bands that occur when the TJ has a low angle (image C1), and bands that occur when the TJ angle is high (image C2). Most bands found were straight lines, but in some occurrences the bands were curved (image B4). While much less prevalent, these bands also appeared at GB, usually when the GB was curved (image A4). Occasionally, the bands also appeared to cut across multiple grains (image C4); though it could just be coincidence that bands at multiple TJs and GBs aligned. Although the phenomenon of GB pileup is universally accepted, not many GBs appeared to show pileup (image A3).

While the features are clearly visible in Figure 4-8, the features were generally less distinct and oftentimes could be classified as somewhere on a continuum between the defined features. For example, images A1 and A2 show a high and low GND level, while this is clear in the example, the value is generally less binary and the level of GND within a grain could fall anywhere within the continuum of high and low. While the fact that GND levels are not binary is obvious, there is sometimes no clear distinction between features; e.g. what may appear as a GB pileup could possibly be GND bands occurring due to the TJ and in a direction parallel with the GB. As previously mentioned, the vast majority of visible GND structures found within this sample were bands that appeared at TJs.

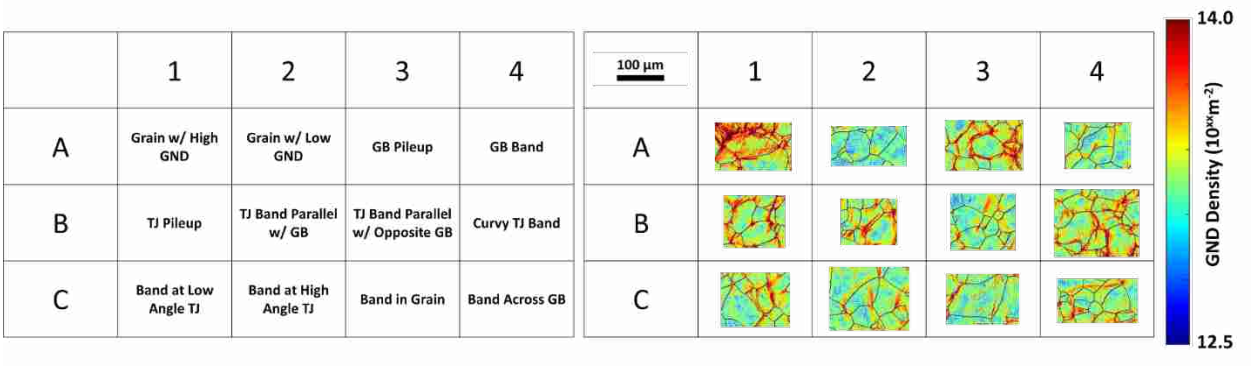

Figure 4-8: Examples of various subgrain GND features.

4.3.2 Influence of Grain Character on GND density

Correlations between grain parameters and grain GND are plotted in Figure 4-9, and associated statistical values are given in Table 4-4 (see section 4.2.4 for a description of the statistical terms used, and see section 4.2.3 for a description of the grain parameters used).

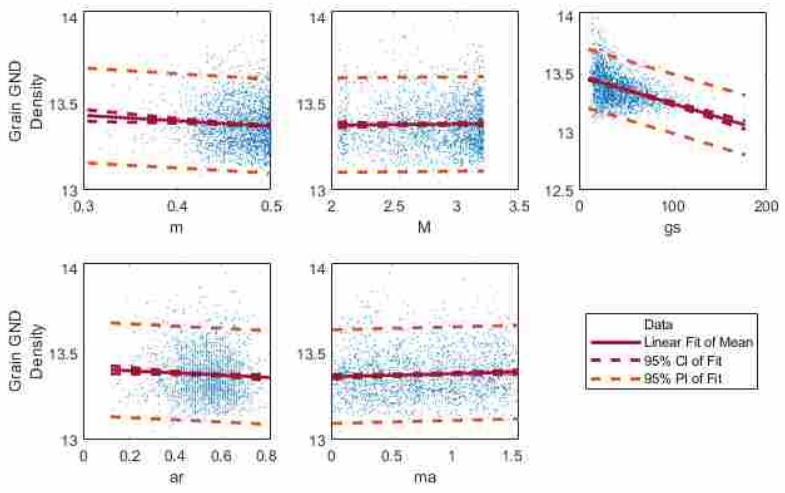

Figure 4-9: Linear regressions fit to various grain parameters.

Table 4-4: Statistical parameters for linear regressions fit to various grain parameters.

Parameter	Impact on GND	R2	p-value of Correlation	Parameter Rank
gs	0.06023	0.13293	1.41E-63	1
m	0.00452	0.00464	2.38E-03	2
ma	0.00227	0.00283	1.76E-02	3
ar	0.00175	0.00280	1.82E-02	4
M	0.00000	0.00021	5.15E-01	5

The wide prediction intervals (PIs) in Figure 4-9 which span nearly the entire range of GND values show that none of the parameters would make good predictors for the grain GND. For reference, 95% of individual instances (grain GND values) are predicted to fall within the region of the PI. Essentially, a very wide range of grain GND values are possible at any given grain parameter value. This fact is also reflected in the low R^2 value.

The impact factor (practical significance) and p-value (statistical significance) are plotted in Figure 4-10 to give a visual representation the strength of the correlations of orientation-based and geometry-based parameter types; the impact factor informs one on how much a given grain parameter likely affect the mean grain GND, and it is related to the lower bound of the CI (see section 4.2.4). The outlying data point in the top right corner is the grain size, and the correlation found that a decreasing grain size lead to an increasing grain GND. The p-value of the correlation between grain size and grain GND was 1.14E-63; p-values for all grain parameters are listed in Table 4-4 (see section 4.2.4 for a description of statistical significance and p-value). This p-value indicates that there is only a 1.14E-61% probability of seeing a correlation as strong or stronger

than the one observed in our data set, if in fact there was no correlation between grain size and the population mean of grain GND. This strong correlation is indicative of the importance of grain size when designing a material.

Additionally, all grain parameters except for the Taylor factor had statistically significant correlations with the grain GND, and the direction of the trends can be seen in Figure 4-9. The parameter with next best p-value after grain size was Schmid factor with a value of 2.38E-3, supporting the conclusions by Carroll et al. that there is likely a correlation between Schmid factor and average strain in a grain [26]; strain gradients likely present in highly strained grains are directly related to GND.

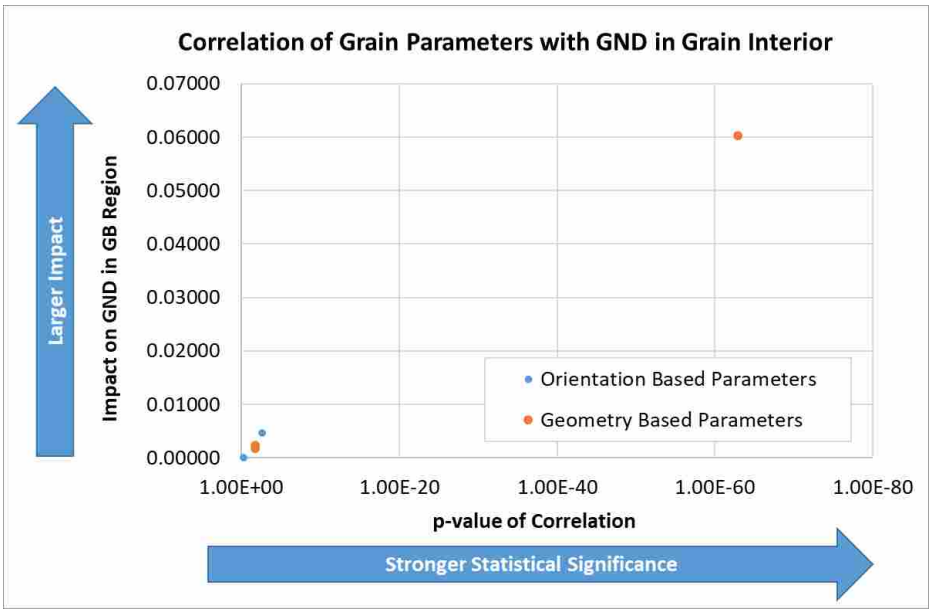

Figure 4-10: Parameters defining the grain are plotted here based on their correlation with grain GND. The upper right geometry-based parameter is the grain size.

4.3.3 Influence of GB Character on GND density

The correlations between GB parameters and GB GND are now explored; these are plotted in Figure 4-11, and associated statistical values are given in Table 4-4. (see section 4.2.4 for a description of the statistical terms used, and see section 4.2.3 for a description of the GB parameters used). The impact factor (practical significance) and p-value (statistical significance) are plotted in Figure 4-12 to give a visual representation the strength of the correlations of orientation-based and geometry-based parameter types.

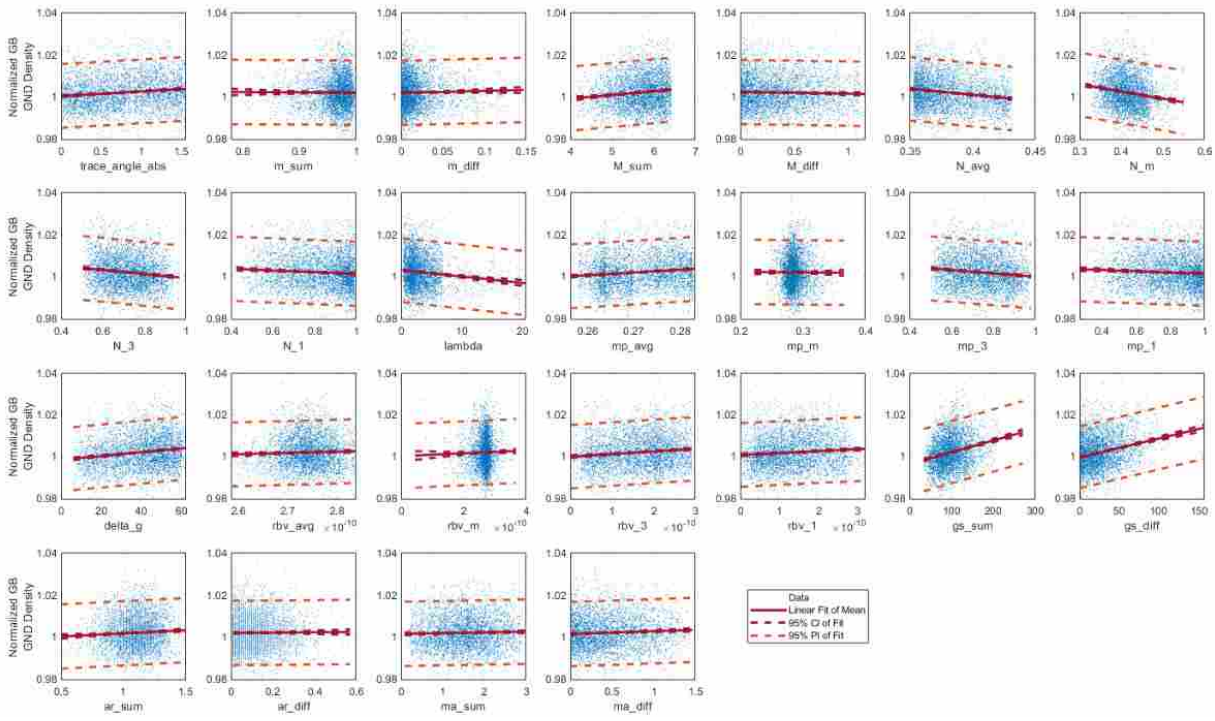

Figure 4-11: Linear regressions fit to various GB parameters.

Table 4-5: Statistical parameters for linear regressions fit to various GB parameters.

Parameter	Impact on GND	R2	p-value of Correlation	Parameter Rank
gs_diff	0.00221	0.06330	6.11E-52	1
gs_sum	0.00207	0.05420	1.61E-44	2
N_avg	0.00172	0.02802	1.56E-23	3
delta_g	0.00164	0.02665	1.90E-22	4
N_m	0.00141	0.02714	7.87E-23	5
trace_angle_abs	0.00127	0.01558	1.08E-13	6
mp_avg	0.00122	0.01412	1.53E-12	7
N_3	0.00111	0.01559	1.06E-13	8
mp_3	0.00107	0.01377	2.90E-12	9
rbv_3	0.00107	0.01394	2.14E-12	10
M_sum	0.00089	0.01230	4.19E-11	11
rbv_1	0.00061	0.00713	5.24E-07	12
lambda	0.00061	0.01456	6.87E-13	13
N_1	0.00048	0.00496	2.91E-05	14
ma_diff	0.00032	0.00355	4.06E-04	15
mp_1	0.00031	0.00336	5.79E-04	16
ar_sum	0.00028	0.00357	3.92E-04	17
rbv_avg	0.00004	0.00133	3.03E-02	18
ar_diff	0.00000	0.00009	5.77E-01	19
ma_sum	0.00000	0.00082	8.87E-02	19
m_sum	0.00000	0.00003	7.45E-01	19
m_diff	0.00000	0.00086	8.27E-02	19
M_diff	0.00000	0.00090	7.44E-02	19
mp_m	0.00000	0.00003	7.53E-01	19
rbv_m	0.00000	0.00053	1.74E-01	19

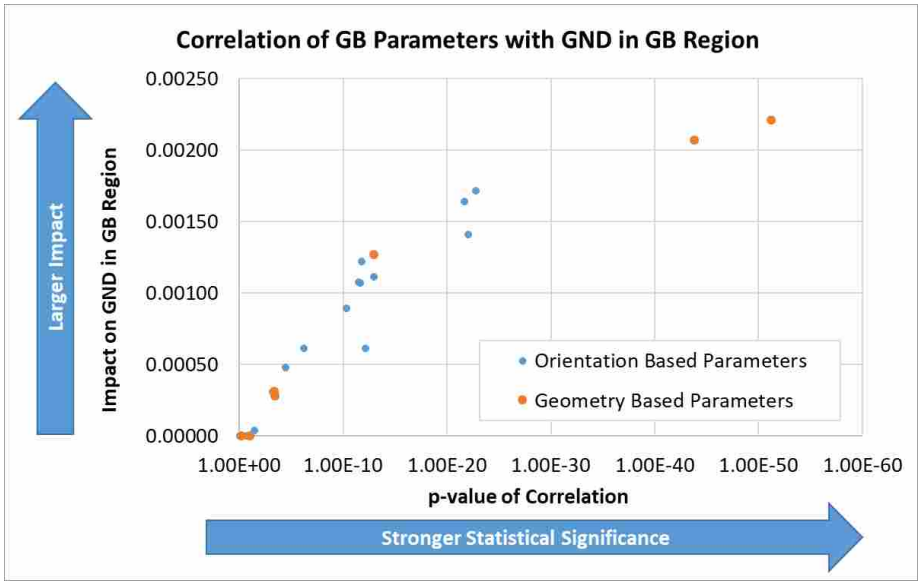

Figure 4-12: Parameters defining the GB are plotted here based on their correlation with GB GND. The two upper right geometry-based parameters are both related to grain size.

Similar to the results of the previous section, wide prediction intervals and low R^2 values are a strong indication that none of the parameters would make good predictors for GB GND, and grain size was the most significant parameter, as can be seen in Figure 4-12 and Table 4-5. Following the two grain size parameters in Figure 4-12, there is a cluster of orientation-based parameters along with a single geometry-based parameter, the trace angle. It was found that a GB trace angle that was perpendicular to the loading direction had higher GND than a GB trace angle that was parallel to the loading direction. As there are many variations of orientation-based parameters, a separate analysis is presented in section 4.3.4 which ranks the various types of orientation-based parameters.

Approximately two thirds of GB parameters had statistically significant correlations with the GB GND; all p-values are listed in Table 4-5 (see section 4.2.4 for a description of statistical significance and p-value); however, one third of the GB parameters that had a p-value above the significance level of 0.05. Many of these parameters that did not have a significant p-value were related to Schmid factor in one way or another, whether they were a direct measure of the Schmid factor, m_sum and m_diff, or were values that were weighted using the Schmid factor, mp_m and rbv_m.

Correlations between TJ parameters and TJ GND were also calculated. They gave very similar results as the correlations between GB GND and GB parameters, and for this reason the associated plots and tables for TJ parameters and TJ GND are reserved as supplementary material in Appendix C. There were, however, some small differences in the ranking of the GB parameters and the TJ parameters, and a discussion of these differences is given in section 4.3.4, along with a more in depth discussion on the ranking of the GB parameters.

4.3.4 Influence of Transmissivity Parameters on GND Density

Ranking was done to determine which GB parameters are impacting the GND within the GB and TJ region the most. Because there were multiple methods for defining a GB using the same type of parameter, e.g. N_{avg}, N_m, N_3, and N_1, the average impact factor of all the various methods of a single GB parameter was taken as a representative value for that parameter. To utilize data from both GBs and TJs, the average ranking of the impact factor from the GB parameters and TJ parameters was taken as the overall raking for the parameters. Additionally, the average impact factor between the GB parameters and TJ parameters was evaluated; this allowed parameters with close rankings to be compared in terms of their relative impact. The results of this ranking is shown in Table 4-6.

Table 4-6: GB parameters were ranked on how much they impacted the GND density near the GB. They are listed in this table from highest impact to lowest impact.

Parameter	Impact on GND (GB)	Parameter Rank (GB)	Impact on GND (TJ)	Parameter Rank (TJ)	Avg. Impact	Avg. Parameter Rank
gs	0.00214	1	0.00288	1	0.00251	1
delta_g	0.00164	2	0.00195	2	0.00180	2
N	0.00118	3	0.00155	3	0.00137	3
lambda	0.00061	4	0.00092	5	0.00077	4.5
M	0.00043	6	0.00126	4	0.00084	5
mp	0.00060	5	0.00054	6	0.00057	5.5
rbv	0.00042	7	0.00047	7	0.00044	7
maa	0.00013	8	0.00014	8	0.00014	8
ar	0.00001	9	0.00012	9	0.00006	9
m	0.00000	10	0.00000	10	0.00000	10

The ranking for the GB parameters generally aligned well with the TJ parameters, suggesting the assumption that the TJ GND is a reflection of how dislocations interact with the GB is likely a fair assumption. As to be expected based on the previous analysis, grain size had

the largest impact on GND. The second most impactful GB parameter was the misorientation between the two grains. Interestingly, it was the most simplistic parameters, grain size and misorientation, that had the largest impact on GND.

While the grain size has the largest impact on GND within the vicinity of the GB for this microstructure, the range of grain sizes observed here is modest, and it is possible to achieve much lower or higher grain sizes than the ones in this dataset. Furthermore, it is likely that the correlation extends beyond the grain sizes observed here, similar to the Hall Petch affect, which finds a correlation between a wide range of grain sizes and yield stress [36,37]. In contrast, all the orientation-based parameters, and practically all other geometry-based parameters, are bounded by upper and lower limits; even though aspect ratio does not have an upper bound, it becomes increasingly difficult to raise as the value increases. This means that even if the correlations extended beyond the range found in this data set, there is less design space to adjust these values.

Additionally, the geometry-based parameters, especially grain size, can readily be controlled with processing methods as simple as rolling and annealing. The orientation-based parameters on the other hand are more difficult to control. One way to attempt to control these parameters is by controlling the crystallographic texture of the material, which has a relationship to the misorientation distribution [38]. Additionally, annealing methods have been shown to be useful in controlling the misorientation distribution [39]. While there is the possibility of some control over the misorientation, Schmid factor, and Taylor factor using these methods, the best approach for controlling the other GB factors is likely to control the misorientation and rely upon its relationship with the other GB factors to positively influence them [21,40,41]. Because grain size is the easiest to control and its value can be extended past the range seen in this sample,

effectively increasing its impact factor, it is recommended that those seeking to control GND within the vicinity of the GB begin by working to control the grain size.

Table 4-6 also helps answer the question posed in the introduction: why do dislocation often appear at the GB? As was discussed, pileup may occur due to incompatibility or due to the lack of GB transmissivity. The relatively low impact of the Schmid factor, m, and the Taylor factor, M, may be an indication that incompatibility play less of a role on GB GND content than transmissivity, as they are commonly used in predicting the likelihood of deformation; differing levels of deformation result in incompatibility. On the other hand, all other parameters in Table 4-6 are generally associated with transmissivity. While Table 4-6 paints a clear picture of the importance of transmissivity at the GB, incompatibility cannot be dismissed. Results in section 4.3.2 found that the Schmid factor had a weak ability to predict GND content — and therefore strain gradients — and a study by Carroll et al. suggest a modest correlation at best between Schmid factor and strain [42]. Thus, the Shmid factor and Taylor factor parameters at the GB may not be an accurate reflection of strain differences and incompatibility at the GB. One major issue with using the Schmid factor or Taylor factor to estimate deformation is that they rely on the global stress state and not the stress state within the individual grain. Predicting this local stress state involves the local interaction many grains, and currently requires simulated methods of the surrounding microstructure, such as CPFEM, to achieve any reasonable estimate.

4.3.5 Representative GB Transmission Factors for Maximum Influence

Because N, m', and RBV are defined for a single slip system combination at the GB and before deformation it is not known which slip systems will be active, four methods outlined in section 1.2 (method_m, method_3, method_1, and method_avg) were used to calculate a

representative or likely transmission factors for these three parameters. Following the same approach described in section 4.3.4, the four methods for calculating a representative GB transmission factor were ranked according to their impact on GND near the GB (see Table 4-7). The average impact factor between the three parameters of the same method, eg. N_3, m_3', and RBV_3, was used a representative impact factor for the method, eg. method _3.

Unlike the ranking of the parameter types in section 4.3.4, the rankings for the methods were not consistent between the GB parameters and the TJ parameters; none of the methods had the same ranking when comparing GB parameter rankings and TJ parameters ranking. However, two methods had relatively high impact factors, method_3 and method_avg, and two methods had relatively low impact factors, method_m and mehtod_1. This suggests that method_3 and method_avg are a better representation of how likely the GB character is to impact GND accumulation.

Table 4-7: Four methods for calculating a representative GB transmission factor are ranked on how much they likely impact GND in the GB region

Parameter	Impact on GND (GB)	Method Rank (GB)	Impact on GND (TJ)	Method Rank (TJ)	Avg. Impact	Avg. Method Rank
method_3	0.00109	1	0.00111	2	0.00110	1.5
method_avg	0.00099	2	0.00131	1	0.00115	1.5
method_m	0.00038	4	0.00067	3	0.00053	3.5
method_1	0.00047	3	0.00033	4	0.00040	3.5

4.4 Conclusion

A statistical analysis was performed on 1989 grains, 3519 GBs, and 3207 TJs in in polycrystalline pure Ta to determine what is impacting the GND density in the grain interior, region near the GB, and region near the TJ. The following conclusions were made:

- While there is some ambiguity when identifying sub-grain GND features (e.g. a strain band may be difficult to differentiate from GB pileup if it occurs near the GB), several distinct types of sub-grain GND features were able to be visually identified in this material, with bands of high GND content near TJs being the most prevalent.
- Large prediction intervals and R^2 values indicated that none of the parameters characterizing grains, GBs, or TJs, could be used to predict the GND density of an individual grain, GB, or TJ.
- However, correlations with strong statistical significance were found between many of the grain, GB, and TJ parameters and the mean GND. This is indicative that there is likely a correlation between the grain, GB, and TJ parameters and the population mean of the grain GND, GB GND, and TJ GND. Although there is strong evidence that correlations exist, the amount by which these parameters influence the mean GND was generally minimal.
- By a significant margin, grain size was the parameter that had the largest impact on the grain GND, GB GND, and TJ GND. Additionally, from a practical standpoint, grain size is the easiest parameter to control during manufacturing and it has a wide range of possible values. Conversely, the majority of the other parameters are difficult to control during manufacturing and have a narrow upper and lower bound on their range.
- GB parameters were ranked on their impact on GND density near the GB, and from most impactful to least impactful they were found to be grain size, misorientation angle, N, λ,

Taylor factor, m', RBV, major axis angle, aspect ratio, and Schmid factor. Due to the relative ease in controlling grain size compared to other parameters and its high impact on GND, it likely the first parameter that should be controlled when attempting to control GND.

- In ranking four methods for calculating a representative transmissivity factors for a GB using N, m', and RBV, it was determined that method_3 (proposed by Bieler et al. [12]) and method_avg were had the largest impact on GND near the GB. Method_m and method_1 (both proposed by Bieler et. al. [12,27]) had less of an impact.

5 CONCLUSION

Studies of dislocation density evolution are fundamental to improved understanding in various areas of deformation mechanics. The accumulation of dislocations causes strain hardening, which strengthens material through friction-type stresses between dislocations [80–82]. Additionally, as GNDs accumulate throughout deformation, the additive nature of their associated stress fields [80] produces a back stress [83,84]. Dislocation-grain boundary interactions and other factors which cause the accumulation of GNDs are explored in this dissertation via HR-EBSD, providing a better understanding of dislocation accumulation and structure. Thus, forwarding material design capabilities at the meso scale.

Chapter 2 tackles the problem of understanding the various types of noise in EBSD patterns that affect HR-EBSD results by setting up a set of simulated patterns that mimic real patterns corresponding to a known GND field. The patterns were subsequently degraded in terms of resolution and noise, and the GND densities calculated from the degraded patterns using cross-correlation ESBD were compared with the known values. Some confirmation of validity of the computational degradation of patterns by considering real pattern degradation was also undertaken. The results demonstrated that the EBSD technique is not particularly sensitive to lower levels of binning and image compression, but the precision is sensitive to Poisson-type noise. Some insight was also gained concerning effects of mixed patterns at a grain boundary on measured GND content.

Chapter 3 explores the evolution of GNDs and their effects on back stress through experimental and computational methods. Four large-grained tantalum tensile specimens were strained in uniaxial tension, electron backscatter diffraction (EBSD) data was collected, and geometrically necessary dislocation (GND) maps of the four specimens in the unloaded state were produced. EBSD-based GND maps revealed several types of features with high GND content which caused back stress in the specimens. Correlations between five geometrically-based grain boundary (GB) transmission factors and the GB GND content were evaluated, and statistically significant correlations were found for transmission factors based on Livingston and Chalmer's N factor, Werner and Prantl's slip transfer number, and GB misorientation. The sign of individual components of the Nye tensor were used to visually and quantitatively identify clustering of GNDs of the same sign, thus giving additional evidence of increasing back stress due to deformation. Deformation of one of the specimens was simulated using multiple CPFEM based modeling approaches and predicted stress-strain responses were compared. The super dislocation model (SD model) — a crystal plasticity finite element method (CPFEM) which incorporates elastic dislocation interactions — was able to isolate impact of back stress on the overall flow stress. The SD model predicted correct stresses when compared with experimental data; however, when the elastic interactions in the SD model were turned off, stress predictions were 25% too low. Thus, demonstrating the importance of incorporating back stress into the model.

Chapter 5 further explores the correlations uncovered in chapter 4 through a statistical analysis of 1989 grains, 3519 GBs, and 3207 TJs. A polycrystalline tensile sample was strained to 4% strain; EBSD data was collected for a large region of the gauge section; HR-EBSD was used to calculated GND density; parameters defining characteristics of the grains, GBs, and TJs were extracted; and correlations were uncovered using statistical analysis. It was found that although

correlations with strong statistical significance existed between many of the grain, GB, and TJ parameters and the mean GND, these correlations had large prediction intervals and could not be used for GND predictions at individual grains, GBs, or TJs. The strongest correlations between GND and the parameters studied related to the grain size. Additionally the correlations between GND near GBs and parameters describing a GB were ranked, and from most impactful to least impactful they were found to be grain size, misorientation angle, N, λ, Taylor factor, m', RBV, major axis angle, aspect ratio, and Schmid factor. Knowledge of these correlations allow for more informed material design and better understanding of the evolution of GND density.

REFERENCES

[1] R.W. Hertzberg, R.P. Vinci, J.L. Hertzberg, Deformation and Fracture Mechanics of Engineering Materials, 5th ed., John Wiley & Sons, Inc., Hoboken, NJ, USA, 2013.

[2] E.O. Hall, The deformation and ageing of mild steel III Discussion of results, Proc. Phys. Soc. Sect. B. 64 (1951) 747. doi:10.1088/0370-1301/64/9/303.

[3] N.J. Petch, The Cleavage Strengths of Polycrystals, J. Iron Steel Inst. 174 (1953) 25–28.

[4] Z. Shen, R.H. Wagoner, W.A.T. Clark, Dislocation and grain boundary interactions in metals, Acta Metall. 36 (1988) 3231–3242. doi:10.1016/0001-6160(88)90058-2.

[5] B.J. Pestman, J.T.M. de Hosson, V. Vitek, F.W. Schapink, Interaction Between Latyice Dislocations and Grain Boundaries, Scr. Metall. 23 (1989) 1431–1435. doi:10.1016/0036-9748(89)90072-0.

[6] D.J. Dingley, R.C. Pond, On the interaction of crystal dislocations with grain boundaries, Acta Metall. 27 (1979) 667–682. doi:10.1016/0001-6160(79)90018-X.

[7] K.G. Davis, E. Techtsoonian, A. Lu, Slip Band Continuity Across Grain Boundaries in Aluminum, Acta Metall. 14 (1966) 1677–1684.

[8] D.M. Martin, T.D. McGee, The Interaction of Dislocations and Boundaries, Acta Met. 17 (1969) 929–932.

[9] M.S. Hooshmand, M.J. Mills, M. Ghazisaeidi, Atomistic modeling of dislocation interactions with twin boundaries in Ti, Model. Simul. Mater. Sci. Eng. 25 (2017).

[10] N. V. Malyar, J.S. Micha, G. Dehm, C. Kirchlechner, Dislocation-twin boundary interaction in small scale Cu bi-crystals loaded in different crystallographic directions, Acta Mater. 129 (2017) 91–97. doi:10.1016/j.actamat.2017.02.067.

[11] Y. Gao, Z. Jin, Interactions between lattice dislocation and Lomer -type low-angle grain boundary in nickel, Comput. Mater. Sci. 138 (2017) 225–235. doi:10.1016/j.commatsci.2017.06.025.

[12] I. Basu, V. Ocelík, J.T.M. De Hosson, Measurement of spatial stress gradients near grain boundaries, Scr. Mater. 136 (2017) 11–14. doi:10.1016/j.scriptamat.2017.03.036.

[13] M. Hamid, H. Lyu, B.J. Schuessler, P.C. Wo, H.M. Zbib, Modeling and Characterization of Grain Boundaries and Slip Transmission in Dislocation Density-Based Crystal Plasticity, Crystals. 7 (2017) 152. doi:10.3390/cryst7060152.

[14] B.L. Adams, Orientation imaging microscopy: Emerging and future applications, Ultramicroscopy. 67 (1997) 11–17. doi:10.1016/S0304-3991(96)00103-9.

[15] S.I. Wright, M.M. Nowell, R. De Kloe, P. Camus, T. Rampton, Electron imaging with an EBSD detector, Ultramicroscopy. 148 (2015) 132–145. doi:10.1016/j.ultramic.2014.10.002.

[16] T.B. Britton, J. Jiang, R. Clough, E. Tarleton, A.I. Kirkland, A.J. Wilkinson, Assessing the precision of strain measurements using electron backscatter diffraction--part 2: experimental demonstration., Ultramicroscopy. 135 (2013) 136–41. doi:10.1016/j.ultramic.2013.08.005.

[17] B.L. Adams, J. Kacher, EBSD-based microscopy: Resolution of dislocation density, Comput. Mater. Contin. 14 (2009) 183–194. http://li.mit.edu/Stuff/RHW/Upload/1.pdf (accessed January 8, 2016).

[18] D. Chen, J.C. Kuo, W.T. Wu, Effect of microscopic parameters on EBSD spatial resolution, Ultramicroscopy. 111 (2011) 1488–1494. doi:10.1016/j.ultramic.2011.06.007.

[19] J. Jiang, T.B. Britton, A.J. Wilkinson, Measurement of geometrically necessary dislocation density with high resolution electron backscatter diffraction: effects of detector binning and step size., Ultramicroscopy. 125 (2013) 1–9. doi:10.1016/j.ultramic.2012.11.003.

[20] J. Kacher, C. Landon, B.L. Adams, D. Fullwood, Bragg's Law diffraction simulations for electron backscatter diffraction analysis, Ultramicroscopy. 109 (2009) 1148–1156. doi:10.1016/j.ultramic.2009.04.007.

[21] K.Z. Troost, P. Van Der Sluis, D.J. Gravesteijn, Microscale elastic-strain determination by backscatter Kikuchi diffraction in the scanning electron microscope, Appl. Phys. Lett. 62 (1993) 1110–1112. doi:10.1063/1.108758.

[22] A.J. Wilkinson, G. Meaden, D.J. Dingley, High-resolution elastic strain measurement from electron backscatter diffraction patterns: New levels of sensitivity, Ultramicroscopy. 106 (2006) 307–313. doi:10.1016/j.ultramic.2005.10.001.

[23] C.J. Gardner, B.L. Adams, J. Basinger, D.T. Fullwood, EBSD-based continuum dislocation microscopy, Int. J. Plast. 26 (2010) 1234–1247. doi:10.1016/j.ijplas.2010.05.008.

[24] T.J. Ruggles, D.T. Fullwood, Estimations of bulk geometrically necessary dislocation density using high resolution EBSD, Ultramicroscopy. 133 (2013) 8–15. doi:10.1016/j.ultramic.2013.04.011.

[25] a J. Wilkinson, E.E. Clarke, T.B. Britton, P. Littlewood, P.S. Karamched, High-resolution electron backscatter diffraction: an emerging tool for studying local deformation, J. Strain Anal. Eng. Des. 45 (2010) 365–376. doi:10.1243/03093247JSA587.

[26] T.J. Ruggles, T.M. Rampton, A. Khosravani, D.T. Fullwood, The effect of length scale on the determination of geometrically necessary dislocations via EBSD continuum dislocation microscopy, Ultramicroscopy. 164 (2016) 1–10. doi:10.1016/j.ultramic.2016.03.003.

[27] a. J. Wilkinson, G. Meaden, D.J. Dingley, High resolution mapping of strains and rotations using electron backscatter diffraction, Mater. Sci. Technol. 22 (2006) 1271–1278.

doi:10.1179/174328406X130966.

[28] B.S. El-Dasher, B.L. Adams, A.D. Rollett, Viewpoint: Experimental recovery of geometrically necessary dislocation density in polycrystals, Scr. Mater. 48 (2003) 141–145. doi:10.1016/S1359-6462(02)00340-8.

[29] N.-H. Schmidt, N. Olesen, Computer-aided determination of crystal-lattice orientation from electron-channeling patterns inthe SEM, Can. Mineral. 27 (1989) 15–22.

[30] J.. Nye, Some geometrical relations in dislocated crystals, Acta Metall. 1 (1953) 153–162. doi:10.1016/0001-6160(53)90054-6.

[31] E. Kroner, Continuum theory of dislocations and self-stressees, (1958). doi:10.1007/978-3-662-30257-6_31.

[32] C. Moussa, M. Bernacki, R. Besnard, N. Bozzolo, Statistical analysis of dislocations and dislocation boundaries from EBSD data, Ultramicroscopy. 179 (2017) 63–72. doi:10.1016/j.ultramic.2017.04.005.

[33] W. Pantleon, Resolving the geometrically necessary dislocation content by conventional electron backscattering diffraction, Scr. Mater. 58 (2008) 994–997. doi:10.1016/j.scriptamat.2008.01.050.

[34] P.D. Littlewood, T.B. Britton, A.J. Wilkinson, Geometrically necessary dislocation density distributions in Ti-6Al-4V deformed in tension, Acta Mater. 59 (2011) 6489–6500. doi:10.1016/j.actamat.2011.07.016.

[35] J. Wheeler, E. Mariani, S. Piazolo, D.J. Prior, P. Trimby, M.R. Drury, The weighted Burgers vector: A new quantity for constraining dislocation densities and types using electron backscatter diffraction on 2D sections through crystalline materials, J. Microsc. 233 (2009) 482–494. doi:10.1111/j.1365-2818.2009.03136.x.

[36] T.J. Ruggles, D.T. Fullwood, J.W. Kysar, Resolving geometrically necessary dislocation density onto individual dislocation types using EBSD-based continuum dislocation microscopy, Int. J. Plast. 76 (2016) 231–243. doi:10.1016/j.ijplas.2015.08.005.

[37] T.R. Bieler, P. Eisenlohr, C. Zhang, H.J. Phukan, M.A. Crimp, Grain boundaries and interfaces in slip transfer, Curr. Opin. Solid State Mater. Sci. 18 (2014) 212–226. doi:10.1016/j.cossms.2014.05.003.

[38] J. Luster, M.A. Morris, Compatibility of deformation in two-phase Ti-Al alloys: Dependence on microstructure and orientation relationships, Metall. Mater. Trans. A. 26 (1995) 1745–1756. doi:10.1007/BF02670762.

[39] E. Werner, W. Prantl, SLIP TRANSFER ACROSS GRAIN AND PHASE BOUNDARIES, Acta Mater. 38 (1990) 533–537.

[40] J.D. Livingston, B. Chalmers, Multiple slip in bicrystal deformation, Acta Metall. 5 (1957) 322–327. doi:10.1016/0001-6160(57)90044-5.

[41] L.C. Lim, R. Raj, The role of residual dislocation arrays in slip induced cavitation, migration and dynamic recrystallization at grain boundaries, Acta Metall. 33 (1985) 2205–2214.

doi:10.1016/0001-6160(85)90182-8.

[42] Z. Shen, R.H. Wagoner, W.A.T. Clark, Dislocation pile-up and grain boundary interactions in 304 stainless steel, Scr. Metall. 20 (1986) 921–926. doi:10.1016/0036-9748(86)90467-9.

[43] W.A.T. Clark, R.H. Wagoner, Z.Y. Shen, T.C. Lee, I.M. Robertson, H.K. Birnbaum, On the criteria for slip transmission across interfaces in polycrystals, Scr. Metall. Mater. 26 (1992) 203–206. doi:10.1016/0956-716X(92)90173-C.

[44] H. Yu, C. Li, Y. Xin, A. Chapuis, X. Huang, Q. Liu, The mechanism for the high dependence of the Hall-Petch slope for twinning/slip on texture in Mg alloys, Acta Mater. 128 (2017) 313–326. doi:10.1016/j.actamat.2017.02.044.

[45] H. Yu, Y. Xin, A. Chapuis, X. Huang, R. Xin, Q. Liu, The different effects of twin boundary and grain boundary on reducing tension-compression yield asymmetry of Mg alloys, Sci. Rep. 6 (2016) 4–11. doi:10.1038/srep29283.

[46] L. Patriarca, W. Abuzaid, H. Sehitoglu, H.J. Maier, Slip transmission in bcc FeCr polycrystal, Mater. Sci. Eng. A. 588 (2013) 308–317. doi:10.1016/j.msea.2013.08.050.

[47] D.M. Bond, M.A. Zikry, A Predictive Framework for Dislocation-Density Pile-Ups in Crystalline Systems With Coincident Site Lattice and Random Grain Boundaries, J. Eng. Mater. Technol. 139 (2016) 021023. doi:10.1115/1.4035494.

[48] J. Kacher, B.P. Eftink, B. Cui, I.M. Robertson, Dislocation interactions with grain boundaries, Curr. Opin. Solid State Mater. Sci. 18 (2014) 227–243. doi:10.1016/j.cossms.2014.05.004.

[49] E. Bayerschen, A.T. McBride, B.D. Reddy, T. Böhlke, Review on slip transmission criteria in experiments and crystal plasticity models, J. Mater. Sci. 51 (2016) 2243–2258. doi:10.1007/s10853-015-9553-4.

[50] P.R.M. Van Beers, G.J. McShane, V.G. Kouznetsova, M.G.D. Geers, Grain boundary interface mechanics in strain gradient crystal plasticity, J. Mech. Phys. Solids. 61 (2013) 2659–2679. doi:10.1016/j.jmps.2013.08.011.

[51] A. Ma, F. Roters, D. Raabe, On the consideration of interactions between dislocations and grain boundaries in crystal plasticity finite element modeling - Theory, experiments, and simulations, Acta Mater. 54 (2006) 2181–2194. doi:10.1016/j.actamat.2006.01.004.

[52] J.D. Carroll, B.G. Clark, T.E. Buchheit, B.L. Boyce, C.R. Weinberger, An experimental statistical analysis of stress projection factors in BCC tantalum, Mater. Sci. Eng. A. 581 (2013) 108–118. doi:10.1016/j.msea.2013.05.085.

[53] T.R. Bieler, R. Alizadeh, M. Peña-Ortega, J. Llorca, An analysis of (the lack of) slip transfer between near-cube oriented grains in pure Al, Int. J. Plast. 118 (2019) 269–290. doi:10.1016/j.ijplas.2019.02.014.

[54] S.I. Wright, M.M. Nowell, S.P. Lindeman, P.P. Camus, M. De Graef, M.A. Jackson, Introduction and comparison of new EBSD post-processing methodologies, Ultramicroscopy. 159 (2015) 81–94. doi:10.1016/j.ultramic.2015.08.001.

[55] P.G. Callahan, M. De Graef, Dynamical Electron Backscatter Diffraction Patterns. Part I: Pattern Simulations, Microsc. Microanal. 19 (2013) 1255–1265. doi:10.1017/S1431927613001840.

[56] J. Jiang, J. Yang, T. Zhang, F.P.E. Dunne, T. Ben Britton, On the mechanistic basis of fatigue crack nucleation in Ni superalloy containing inclusions using high resolution electron backscatter diffraction, Acta Mater. 97 (2015) 367–379. doi:10.1016/j.actamat.2015.06.035.

[57] T.B. Britton, C. Maurice, R. Fortunier, J.H. Driver, A.P. Day, G. Meaden, D.J. Dingley, K. Mingard, A.J. Wilkinson, Factors affecting the accuracy of high resolution electron backscatter diffraction when using simulated patterns., Ultramicroscopy. 110 (2010) 1443–53. doi:10.1016/j.ultramic.2010.08.001.

[58] D. Fullwood, M. Vaudin, C. Daniels, T. Ruggles, S.I. Wright, Validation of kinematically simulated pattern HR-EBSD for measuring absolute strains and lattice tetragonality, Mater. Charact. 107 (2015) 270–277. doi:10.1016/j.matchar.2015.07.017.

[59] OIM Analysis, (2010).

[60] S.I. Wright, M.M. Nowell, EBSD Image Quality Mapping, Microsc. Microanal. 12 (2006) 72–84.

[61] J.W. Kysar, Y. Saito, M.S. Oztop, D. Lee, W.T. Huh, Experimental lower bounds on geometrically necessary dislocation density, Int. J. Plast. 26 (2010) 1097–1123. doi:10.1016/j.ijplas.2010.03.009.

[62] D.T. Fullwood, B.L. Adams, J. Basinger, T.J. Ruggles, A. Khosravani, C. Sorensen, J. Kacher, Microstructure Detail Extraction via EBSD: An Overview, Strains Dislocation Gradients from Diffr. (2014) 1–400. doi:10.1142/9781908979636_0012.

[63] T.B. Britton, J. Jiang, R. Clough, E. Tarleton, A.I. Kirkland, A.J. Wilkinson, Assessing the precision of strain measurements using electron backscatter diffraction - part 1: Detector assessment, Ultramicroscopy. 135 (2013) 126–135. doi:10.1016/j.ultramic.2013.08.005.

[64] V. Tong, J. Jiang, A.J. Wilkinson, T. Ben Britton, The effect of pattern overlap on the accuracy of high resolution electron backscatter diffraction measurements, Ultramicroscopy. 155 (2015) 62–73. doi:10.1016/j.ultramic.2015.04.019.

[65] F. Ram, S. Zaefferer, T. Jäpel, D. Raabe, Error analysis of the crystal orientations and disorientations obtained by the classical electron backscatter diffraction technique, J. Appl. Crystallogr. 48 (2015) 797–813. doi:10.1107/S1600576715005762.

[66] EMsoft, (2015).

[67] T.B. Britton, A.J. Wilkinson, High resolution electron backscatter diffraction measurements of elastic strain variations in the presence of larger lattice rotations, Ultramicroscopy. 114 (2012) 82–95. doi:10.1016/j.ultramic.2012.01.004.

[68] T.B. Britton, A.J. Wilkinson, Measurement of residual elastic strain and lattice rotations with high resolution electron backscatter diffraction, Ultramicroscopy. 111 (2011) 1395–1404. doi:10.1016/j.ultramic.2011.05.007.

[69] C. Maurice, J.H. Driver, R. Fortunier, On solving the orientation gradient dependency of high angular resolution EBSD, Ultramicroscopy. 113 (2012) 171–181. doi:10.1016/j.ultramic.2011.10.013.

[70] MATLAB, (2014).

[71] P. Cizmar, A.E. Vladár, B. Ming, M.T. Postek, Simulated SEM images for resolution measurement, Scanning. 30 (2008) 381–391. doi:10.1002/sca.20120.

[72] P.T. Pinard, M. Lagacé, P. Hovington, D. Thibault, An Open-Source Engine for the Processing of Electron Backscatter Patterns : EBSD-Image, Micorscopy Microanal. (2011) 1–12.

[73] S.U. Park, D. Wei, M. De Graef, M. Shah, J. Simmons, A.O. Hero, EBSD image segmentation using a physics-based forward model, 2013 IEEE Int. Conf. Image Process. ICIP 2013 - Proc. (2013) 3780–3784. doi:10.1109/ICIP.2013.6738779.

[74] C. Sorensen, J.A. Basinger, M.M. Nowell, D.T. Fullwood, Five-parameter grain boundary inclination recovery with ebsd and interaction volume models, Metall. Mater. Trans. A Phys. Metall. Mater. Sci. 45 (2014) 4165–4172. doi:10.1007/s11661-014-2345-7.

[75] T. Benjamin Britton, A.J. Wilkinson, Stress fields and geometrically necessary dislocation density distributions near the head of a blocked slip band, Acta Mater. 60 (2012) 5773–5782. doi:10.1016/j.actamat.2012.07.004.

[76] Y. Guo, T.B. Britton, A.J. Wilkinson, Slip band-grain boundary interactions in commercial-purity titanium, Acta Mater. 76 (2014) 1–12. doi:10.1016/j.actamat.2014.05.015.

[77] B. Larrouy, P. Villechaise, J. Cormier, O. Berteaux, Grain boundary-slip bands interactions: Impact on the fatigue crack initiation in a polycrystalline forged Ni-based superalloy, Acta Mater. 99 (2015) 325–336. doi:10.1016/j.actamat.2015.08.009.

[78] OpenXY, (2015).

[79] C.D. Landon, B.L. Adams, J. Kacher, High-Resolution Methods for Characterizing Mesoscale Dislocation Structures, J. Eng. Mater. Technol. 130 (2008) 021004. doi:10.1115/1.2840961.

[80] J.P. Hirth, J. Lothe, Theory of Dislocations, Krieger Publishing Company, 1982.

[81] N.A. Fleck, M.F. Ashby, J.W. Hutchinson, The role of geometrically necessary dislocations in giving material strengthening, 48 (2003) 179–183.

[82] D. Kuhlmann-Wilsdorf, C. Laird, Dislocation behavior in fatigue II. Friction stress and back stress as inferred from an analysis of hysteresis loops, Mater. Sci. Eng. 37 (1979) 111–120. doi:10.1016/0025-5416(79)90074-0.

[83] M.F. Ashby, The deformation of plastically non-homogeneous materials, Philos. Mag. 21 (1970) 399–424. doi:10.1080/14786437008238426.

[84] I.A. Ovid'ko, R.Z. Valiev, Y.T. Zhu, Review on superior strength and enhanced ductility of metallic nanomaterials, Prog. Mater. Sci. 94 (2018) 462–540. doi:10.1016/j.pmatsci.2018.02.002.

[85] M. Yang, Y. Pan, F. Yuan, Y. Zhu, X. Wu, Back stress strengthening and strain hardening in gradient structure, Mater. Res. Lett. 4 (2016) 145–151. doi:10.1080/21663831.2016.1153004.

[86] X. Feaugas, On the origin of the tensile flow stress in the stainless steel AISI 316L at 300K : back stress and effective stress. Acta materialia, 47 :3617–3632. 1999, Acta Mater. 47 (1999) 3617–3632.

[87] E. Ma, T. Zhu, Towards strength–ductility synergy through the design of heterogeneous nanostructures in metals, Mater. Today. 20 (2017) 323–331. doi:10.1016/j.mattod.2017.02.003.

[88] N. a. Fleck, G.M. Muller, M.F. Ashby, J.W. Hutchinson, Strain gradient plasticity: Theory and experiment, Acta Metall. Mater. 42 (1994) 475–487. doi:10.1016/0956-7151(94)90502-9.

[89] N. Hansen, R.F. Mehl, New discoveries in deformed metals, Metall. Mater. Trans. A Phys. Metall. Mater. Sci. 32 (2001) 2917–2935. doi:10.1007/s11661-001-0167-x.

[90] D. Kuhlmann-Wilsdorf, N. Hansen, Geometrically necessary, incidental and subgrain boundaries, Scr. Metall. Mater. 25 (1991) 1557–1562. doi:10.1016/0956-716X(91)90451-6.

[91] D.A. Hughes, N. Hansen, D.J. Bammann, Geometrically necessary boundaries, incidental dislocation boundaries and geometrically necessary dislocations, Scr. Mater. 48 (2003) 147–153.

[92] S.S. Firouzabadi, M. Kazeminezhad, Cell-structure and flow stress investigation of largely strained non-heat-treatable Al-alloys using dislocation based model, Mater. Sci. Eng. A. 739 (2019) 167–172. doi:10.1016/j.msea.2018.10.007.

[93] H. Lim, M.G. Lee, J.H. Kim, B.L. Adams, R.H. Wagoner, Simulation of polycrystal deformation with grain and grain boundary effects, Int. J. Plast. 27 (2011) 1328–1354. doi:10.1016/j.ijplas.2011.03.001.

[94] M.G. Lee, H. Lim, B.L. Adams, J.P. Hirth, R.H. Wagoner, A dislocation density-based single crystal constitutive equation, Int. J. Plast. 26 (2010) 925–938. doi:10.1016/j.ijplas.2009.11.004.

[95] H. Lim, S. Subedi, D.T. Fullwood, B.L. Adams, R.H. Wagoner, A Practical Meso-Scale Polycrystal Model to Predict Dislocation Densities and the Hall-Petch Effect, Mater. Trans. 55 (2014) 35–38. doi:10.2320/matertrans.MA201305.

[96] W. Gan, H.J. Bong, H. Lim, R.K. Boger, F. Barlat, R.H. Wagoner, Mechanism of the Bauschinger Effect in “Hard Pin” Al-Ge-Si Alloys, Mater. Sci. Eng. A. Submitted (2016) 353–372. doi:10.1016/j.msea.2016.12.020.

[97] H.J. Bong, H. Lim, M.G. Lee, D.T. Fullwood, E.R. Homer, R.H. Wagoner, An RVE procedure for micromechanical prediction of mechanical behavior of dual-phase steel, Mater. Sci. Eng. A. 695 (2017) 101–111. doi:10.1016/j.msea.2017.04.032.

[98] D. Peirce, R.J. Asaro, A. Needleman, An analysis of nonuniform and localized deformation

in ductile single crystals, Acta Metall. 30 (1982) 1087–1119. doi:10.1016/0001-6160(82)90005-0.

[99] G. Schoeck, R. Frydman, The contribution of the dislocation forest to the flow stress, Phys. Status Solidi. (1972).

[100] J. Gubicza, N.Q. Chinh, J.L. Lábár, S. Dobatkin, Z. Hegedűs, T.G. Langdon, Correlation between microstructure and mechanical properties of severely deformed metals, J. Alloys Compd. 483 (2009) 271–274. doi:10.1016/j.jallcom.2008.07.200.

[101] U.F. Kocks, Laws for Work-Hardening and Low-Temperature Creep, J. Eng. Mater. Technol. 98 (1976) 76–85.

[102] E. Orowan, Problems of plastic gliding, Proc. Phys. Soc. 52 (1940) 8–22. doi:10.1088/0959-5309/52/1/303.

[103] H. Lim, J.D. Carroll, C.C. Battaile, B.L. Boyce, C.R. Weinberger, Quantitative comparison between experimental measurements and CP-FEM predictions of plastic deformation in a tantalum oligocrystal, Int. J. Mech. Sci. 92 (2015) 98–108. doi:10.1016/j.ijmecsci.2014.12.010.

[104] H. Lim, J.D. Carroll, C.C. Battaile, T.E. Buchheit, B.L. Boyce, C.R. Weinberger, Grain-scale experimental validation of crystal plasticity finite element simulations of tantalum oligocrystals, Int. J. Plast. 60 (2014) 1–18. doi:10.1016/j.ijplas.2014.05.004.

[105] B.L. Boyce, B.G. Clark, P. Lu, J.D. Carroll, C.R. Weinberger, The morphology of tensile failure in tantalum, Metall. Mater. Trans. A Phys. Metall. Mater. Sci. 44 (2013) 4567–4580. doi:10.1007/s11661-013-1814-8.

[106] C.C. Battaile, L.N. Brewer, J.M. Emery, B.L. Boyce, Quantifying Uncertainty from Material Inhomogeneity, 2009.

[107] S. Chen, Q. Yu, The role of low angle grain boundary in deformation of titanium and its size effect, Scr. Mater. 163 (2019) 148–151. doi:10.1016/j.scriptamat.2018.10.054.

[108] S. Mohan, R. Li, H.B. Chew, Local stress analysis of partial dislocation interactions with symmetrical-tilt grain boundaries containing E-structural units, Philos. Mag. 98 (2018) 2345–2366. doi:10.1080/14786435.2018.1486049.

[109] D.W. Adams, D.T. Fullwood, R.H. Wagoner, E.R. Homer, Atomistic survey of grain boundary-dislocation interactions in FCC nickel, Comput. Mater. Sci. 164 (2019) 171–185. doi:10.1016/j.commatsci.2019.04.007.

[110] S. Hémery, P. Nizou, P. Villechaise, In situ SEM investigation of slip transfer in Ti-6Al-4V: Effect of applied stress, Mater. Sci. Eng. A. 709 (2018) 277–284. doi:10.1016/j.msea.2017.10.058.

[111] W.Z. Abuzaid, M.D. Sangid, J.D. Carroll, H. Sehitoglu, J. Lambros, J. Abuzaid, Wael Z., Sangid, Michael D., Carrol, Jay D., Sehitoglu, Huseyin, Lambros, Slip transfer and plastic strain accumulation across grain boundaries in Hastelloy X, J. Mech. Phys. Solids. 60 (2012) 1201–1220. doi:10.1016/j.jmps.2012.02.001.

[112] I. Gutierrez-Urrutia, D. Raabe, Multistage strain hardening through dislocation substructure and twinning in a high strength and ductile weight-reduced Fe-Mn-Al-C steel, Acta Mater. 60 (2012) 5791–5802. doi:10.1016/j.actamat.2012.07.018.

[113] P.J. Hurley, F.J. Humphreys, The application of EBSD to the study of substructural development in a cold rolled single-phase aluminium alloy, Acta Mater. 51 (2003) 1087–1102. doi:10.1016/S1359-6454(02)00513-X.

[114] S. Wang, A. Nagao, P. Sofronis, I.M. Robertson, Hydrogen-modified dislocation structures in a cyclically deformed ferritic-pearlitic low carbon steel, Acta Mater. 144 (2018) 164–176. doi:10.1016/j.actamat.2017.10.034.

[115] I. Gutierrez-Urrutia, D. Raabe, Dislocation and twin substructure evolution during strain hardening of an Fe-22 wt.% Mn-0.6 wt.% C TWIP steel observed by electron channeling contrast imaging, Acta Mater. 59 (2011) 6449–6462. doi:10.1016/j.actamat.2011.07.009.

[116] C.C. Merriman, D.P. Field, P. Trivedi, Orientation dependence of dislocation structure evolution during cold rolling of aluminum, Mater. Sci. Eng. A. 494 (2008) 28–35. doi:10.1016/j.msea.2007.10.090.

[117] D. Wallis, L.N. Hansen, T. Ben Britton, A.J. Wilkinson, Geometrically necessary dislocation densities in olivine obtained using high-angular resolution electron backscatter diffraction, Ultramicroscopy. 168 (2016) 34–45. doi:10.1016/j.ultramic.2016.06.002.

[118] H. Mughrabi, Dislocation wall and cell structures and long-range internal stresses in deformed metal crystals, Acta Metall. 31 (1983) 1367–1379. https://ac.els-cdn.com/000161608390007X/1-s2.0-000161608390007X-main.pdf?_tid=f0b40460-c4a2-4967-a19e-fad9f807d7fd&acdnat=1544113059_afdf3cc0857f1ec46eb17416968c6fc6%0Ahttps://ac.els-cdn.com/000161608390007X/1-s2.0-000161608390007X-main.pdf?_tid=c6a522b3-.

[119] Y. Wang, M. Yang, X. Ma, M. Wang, K. Yin, A. Huang, C. Huang, Improved back stress and synergetic strain hardening in coarse-grain/nanostructure laminates, Mater. Sci. Eng. A. 727 (2018) 113–118. doi:10.1016/j.msea.2018.04.107.

[120] Y. Wang, F. Guo, Q. He, L. Song, M. Wang, A. Huang, Y. Li, C. Huang, Synergetic deformation-induced extraordinary softening and hardening in gradient copper, Mater. Sci. Eng. A. 752 (2019) 217–222. doi:10.1016/j.msea.2019.03.020.

[121] J.A. Benito, R. Cobo, W. Lei, J. Calvo, J.M. Cabrera, Stress-strain response and microstructural evolution of a FeMnCAl TWIP steel during tension-compression tests, Mater. Sci. Eng. A. 655 (2016) 310–320. doi:10.1016/j.msea.2016.01.004.

[122] M. Lazar, Dislocations in the field theory of elastoplasticity, Comput. Mater. Sci. 28 (2003) 419–428. doi:10.1016/j.commatsci.2003.08.003.

[123] P.W.J. Mckenzie, R. Lapovok, Y. Estrin, The influence of back pressure on ECAP processed AA 6016: Modeling and experiment, Acta Mater. 55 (2007) 2985–2993. doi:10.1016/j.actamat.2006.12.038.

[124] R.S. Yassar, O. AbuOmar, E. Hansen, M.F. Horstemeyer, On dislocation-based artificial neural network modeling of flow stress, Mater. Des. 31 (2010) 3683–3689.

doi:10.1016/j.matdes.2010.02.051.

[125] T.E. Buchheit, E.K. Cerreta, L. Diebler, S. Chen, R. Joseph, Characterization of Tri-lab Tantalum (Ta) Plate, (2014).

[126] J.K. MACKENZIE, Second Paper on Statistics Associated With the Random Disorientation of Cubes, Biometrika. 45 (1958) 229–240. doi:10.1093/biomet/45.1-2.229.

[127] T.J. Ruggles, G.F. Bomarito, R.L. Qiu, J.D. Hochhalter, New levels of high angular resolution EBSD performance via inverse compositional Gauss–Newton based digital image correlation, Ultramicroscopy. 195 (2018) 85–92. doi:10.1016/j.ultramic.2018.08.020.

[128] M.J. McLean, W.A. Osborn, In-situ elastic strain mapping during micromechanical testing using EBSD, Ultramicroscopy. 185 (2018) 21–26. doi:10.1016/j.ultramic.2017.11.007.

[129] F. Ramsey, D. Schafer, The statistical sleuth: a course in methods of data analysis, Cengage Learning, 2012.

[130] W.C. Navidi, Statistics for engineers and scientists, McGraw-Hill Higher Education New York, NY, USA, 2008.

[131] S. Mironov, Y.S. Sato, H. Kokawa, Friction-stir processing, in: H. Garbacz, I.P. Semenova, S. Zherebtsov, M. Motyka (Eds.), Nanocrystalline Titan., Elsevier, 2019: pp. 55–69. doi:https://doi.org/10.1016/B978-0-12-814599-9.00004-3.

[132] A.D. Rollett, Materials Processing and Texture, John Wiley & Sons, 2008.

[133] R. Xin, Y. Liang, C. Ding, C. Guo, B. Wang, Q. Liu, Geometrical compatibility factor analysis of paired extension twins in extruded Mg-3Al-1Zn alloys, Mater. Des. 86 (2015) 656–663. doi:10.1016/j.matdes.2015.07.130.

[134] Q. Huang, R. Xin, Correlation between Boundary Misorientation and a Geometric Parameter for Cross-Boundary Twins in Mg Alloys, Adv. Eng. Mater. 19 (2017) 1–6. doi:10.1002/adem.201600614.

[135] R. Takahashi, A Hybrid Bishop-Hill Model for Microstructure Sensitive Design, (2012).

APPENDIX A. CRYSTALLOGRAPHIC ORIENTATIONS OF LARGE GRAINED TANATALUM SPECIMENS

Table 4 – Average initial crystal orientations for the three tantalum specimens (Bunge Euler angles given in degrees). Each grain's Euler angle is given in the x and y reference frame shown in Figure 3-1.

Specimen 1											
Grain	ϕ_1	Φ	ϕ_2	Grain	ϕ_1	Φ	ϕ_2	Grain	ϕ_1	Φ	ϕ_2
1	273.3	135.1	316.7	6	104.5	119.3	309.6	11	288.0	135.3	315.9
2	97.7	132.7	312.9	7	114.1	139.4	312.5	12	305.4	131.4	322.8
3	105.6	151.4	315.8	8	73.5	144.8	311.1	13	136.4	128.5	320.0
4	92.5	154.1	312.4	9	286.0	129.3	304.6	14	230.8	136.2	312.5
5	162.8	128.2	316.3	10	293.8	127.2	315.9	15	117.5	134.1	316.7
Specimen 2											
Grain	ϕ_1	Φ	ϕ_2	Grain	ϕ_1	Φ	ϕ_2	Grain	ϕ_1	Φ	ϕ_2
1	142.4	130.8	329.2	7	348.2	155.9	319.4	13	15.1	163.1	295.4
2	170.8	135.3	325.6	8	106.0	126.2	316.7	14	54.3	130.2	320.7
3	11.6	155.3	314.5	9	21.8	140.0	322.2	15	196.9	135.2	329.2
4	168.4	128.0	317.2	10	346.0	137.1	317.1	16	186.7	135.8	320.9
5	52.8	127.5	319.2	11	338.8	140.1	311.2	17	43.7	129.3	305.9
6	149.3	127.2	314.2	12	191.7	129.1	316.6				
Specimen 3											
Grain	ϕ_1	Φ	ϕ_2	Grain	ϕ_1	Φ	ϕ_2	Grain	ϕ_1	Φ	ϕ_2
1	187.7	23.8	135.8	4	186.6	24.3	137.2	7	195.5	23.8	128.2
2	336.4	46.9	41.3	5	187.5	35.5	133.7	8	60.1	52.8	310.3
3	193.4	13.4	141.4	6	196.9	16.1	130.7	9	18.2	24.3	305.6
Specimen 4											
Grain	ϕ_1	Φ	ϕ_2	Grain	ϕ_1	Φ	ϕ_2	Grain	ϕ_1	Φ	ϕ_2
1	253.2	42.8	126.2	6	41.7	56.4	311.4	11	248.9	36.1	130.6
2	119.1	53.0	227.5	7	203.7	33.4	141.0	12	310.1	44.5	46.5
3	226.7	52.4	139.6	8	76.7	38.7	317.7	13	259.0	27.3	133.0
4	230.9	48.9	132.5	9	226.3	23.9	146.3	14	61.1	44.8	305.2
5	22.7	11.5	352.0	10	252.2	15.4	113.6				

APPENDIX B. SIGNED MAPS OF THE EBSD-VISIBLE COMPONENTS OF THE NYE TENSOR

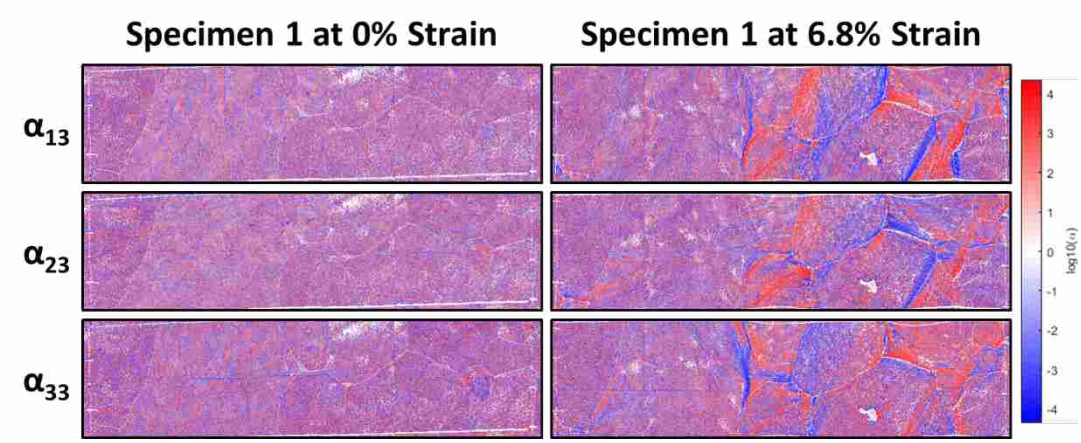

Fig. 12 – The 13, 23, and 33 components of the Nye tensor — the three components available via EBSD — from specimen 1 at 0% strain (left) and 6.8% strain (right).

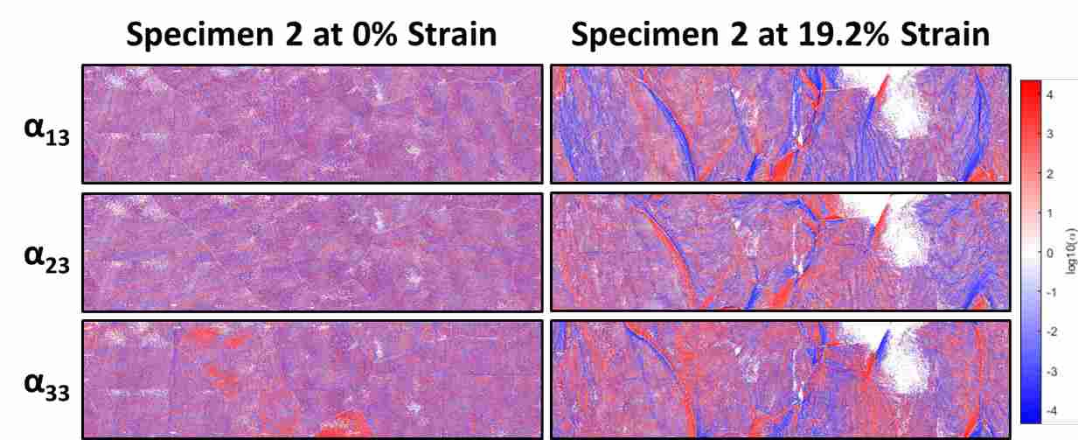

Fig. 13 – The 13, 23, and 33 components of the Nye tensor — the three components available via EBSD — from specimen 2 at 0% strain (left) and 19.2% strain (right).

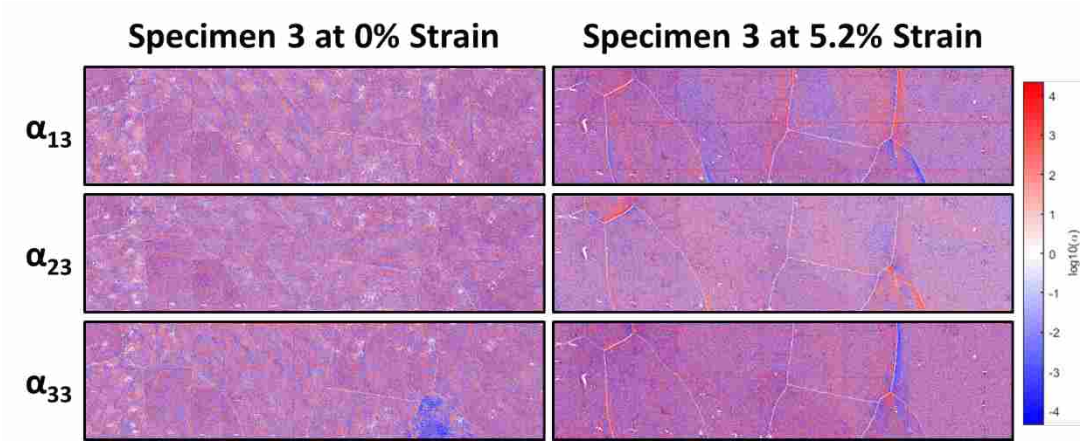

Fig. 14 – The 13, 23, and 33 components of the Nye tensor — the three components available via EBSD — from specimen 3 at 0% strain (left) and 5.2% strain (right).

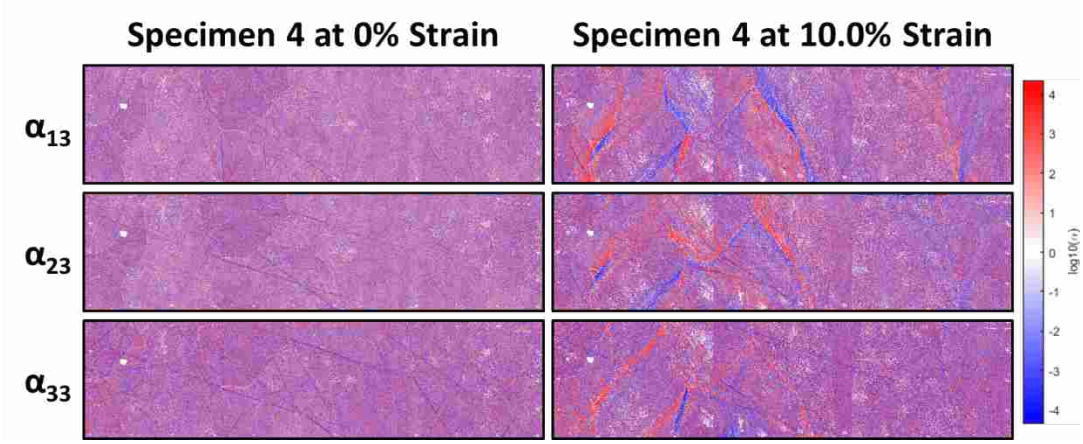

Fig. 15 – The 13, 23, and 33 components of the Nye tensor — the three components available via EBSD — from specimen 4 at 0% strain (left) and 10% strain (right).

APPENDIX C. ADDITIONAL STATISTICAL DATA FOR GRAIN, GB, AND TJ ANALYSIS

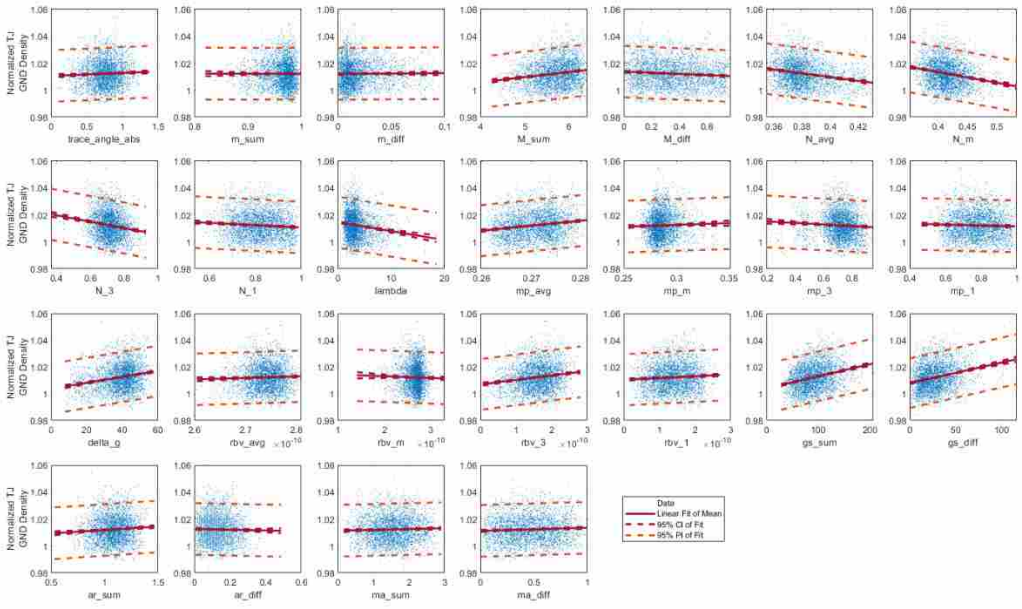

Figure 5-1: Linear regressions fit to various TJ parameters.

Table 5-1: Statistical parameters for linear regressions fit to various TJ parameters.

Parameter	Impact on GND	R2	p-value of Correlation	Parameter Rank
gs_sum	0.00294	0.06695	3.20E-50	1
gs_diff	0.00282	0.06575	2.54E-49	2
N_m	0.00216	0.04317	1.31E-32	3
mp_avg	0.00198	0.02665	1.36E-20	4
N_avg	0.00197	0.04519	4.31E-34	5
delta_g	0.00195	0.04248	4.16E-32	6
M_sum	0.00169	0.02523	1.45E-19	7
rbv_3	0.00157	0.02431	6.66E-19	8
N_3	0.00151	0.02380	1.55E-18	9
lambda	0.00092	0.01897	4.74E-15	10
M_diff	0.00082	0.00758	7.89E-07	11
N_1	0.00057	0.00540	3.09E-05	12
ar_sum	0.00044	0.00457	1.28E-04	13
rbv_1	0.00042	0.00400	3.37E-04	14
ma_diff	0.00029	0.00284	2.52E-03	15
mp_3	0.00025	0.00347	8.49E-04	16
gb_1_2_3_trace_angle	0.00011	0.00188	1.40E-02	17
ma_sum	0.00000	0.00115	5.49E-02	18
ar_diff	0.00000	0.00038	2.72E-01	18
mp_1	0.00000	0.00113	5.66E-02	18
rbv_avg	0.00000	0.00109	6.13E-02	18
mp_m	0.00000	0.00090	8.89E-02	18
rbv_m	0.00000	0.00053	1.93E-01	18
m_diff	0.00000	0.00007	6.36E-01	18
m_sum	0.00000	0.00000	9.80E-01	18

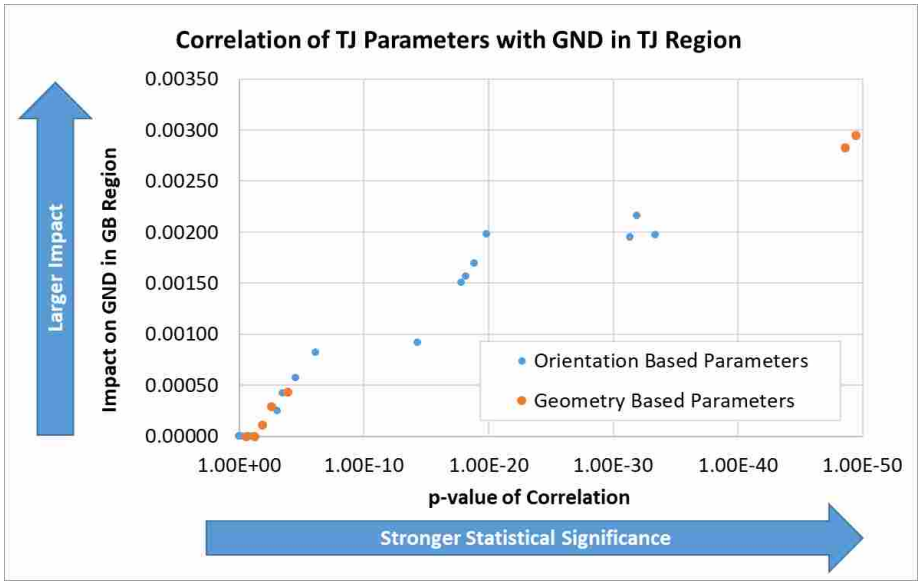

Figure 5-2: Parameters defining the TJ are plotted here based on their correlation with TJ GND. The two upper right geometry-based parameters are both related to grain size.

Table 5-2: Additional statistical parameters for the linear regressions fits to various grain parameters.

Parameter	Impact on GND	R2	p-value of Correlation	Parameter Rank	Slope +/- 95% CI	Relative Slope +/- 95% CI	Interquartile Range	Parameter Type
gs	0.06023	0.13293	1.41E-63	1	-2.4E-03 +/- 2.7E-04	-0.06786 +/- 0.00763	2.86E+01	Geometric
m	0.00452	0.00464	2.38E-03	2	-3.1E-01 +/- 2.0E-01	-0.01271 +/- 0.00819	4.05E-02	Orientation
ma	0.00227	0.00283	1.76E-02	3	1.7E-02 +/- 1.4E-02	0.01305 +/- 0.01077	7.57E-01	Geometric
ar	0.00175	0.00280	1.82E-02	4	-6.4E-02 +/- 5.3E-02	-0.01026 +/- 0.00852	1.60E-01	Geometric
M	0.00000	0.00021	5.15E-01	5	6.0E-03 +/- 1.8E-02	0.00320 +/- 0.00963	5.29E-01	Orientation

Table 5-3: Additional statistical parameters for the linear regressions fits to various GB parameters.

Parameter	Impact on GND	R2	p-value of Correlation	Parameter Rank	Slope +/- 95% CI	Relative Slope +/- 95% CI	Interquartile Range	Parameter Type
gs_diff	0.00221	0.06330	6.11E-52	1	9.1E-05 +/- 1.2E-05	0.00254 +/- 0.00032	2.79E+01	Geometric
gs_sum	0.00207	0.05420	1.61E-44	2	5.6E-05 +/- 7.8E-06	0.00240 +/- 0.00033	4.26E+01	Geometric
N_avg	0.00172	0.02802	1.56E-23	3	-5.7E-02 +/- 1.1E-02	-0.00213 +/- 0.00041	3.71E-02	Orientation
delta_g	0.00164	0.02665	1.90E-22	4	9.1E-05 +/- 1.8E-05	0.00205 +/- 0.00041	2.25E+01	Orientation
N_m	0.00141	0.02714	7.87E-23	5	-3.4E-02 +/- 6.8E-03	-0.00176 +/- 0.00035	5.11E-02	Orientation
trace_angle_abs	0.00127	0.01558	1.08E-13	6	2.2E-03 +/- 5.7E-04	0.00173 +/- 0.00045	7.94E-01	Geometric
mp_avg	0.00122	0.01412	1.53E-12	7	1.3E-01 +/- 3.7E-02	0.00168 +/- 0.00047	1.27E-02	Orientation
N_3	0.00111	0.01559	1.06E-13	8	-9.7E-03 +/- 2.5E-03	-0.00151 +/- 0.00040	1.56E-01	Orientation
mp_3	0.00107	0.01377	2.90E-12	9	-7.9E-03 +/- 2.2E-03	-0.00149 +/- 0.00042	1.88E-01	Orientation
rbv_3	0.00107	0.01394	2.14E-12	10	1.3E+07 +/- 3.5E+06	0.00148 +/- 0.00041	1.16E-10	Orientation
M_sum	0.00089	0.01230	4.19E-11	11	1.8E-03 +/- 5.3E-04	0.00127 +/- 0.00038	7.11E-01	Orientation
rbv_1	0.00061	0.00713	5.24E-07	12	9.3E+06 +/- 3.6E+06	0.00101 +/- 0.00039	1.09E-10	Orientation
lambda	0.00061	0.01456	6.87E-13	13	-3.1E-04 +/- 8.4E-05	-0.00084 +/- 0.00023	2.72E+00	Orientation
N_1	0.00048	0.00496	2.91E-05	14	-4.1E-03 +/- 1.9E-03	-0.00090 +/- 0.00042	2.21E-01	Orientation
ma_diff	0.00032	0.00355	4.06E-04	15	1.3E-03 +/- 7.5E-04	0.00071 +/- 0.00039	5.25E-01	Geometric
mp_1	0.00031	0.00336	5.79E-04	16	-2.9E-03 +/- 1.6E-03	-0.00071 +/- 0.00041	2.48E-01	Orientation
ar_sum	0.00028	0.00357	3.92E-04	17	3.0E-03 +/- 1.7E-03	0.00063 +/- 0.00035	2.10E-01	Geometric
rbv_avg	0.00004	0.00133	3.03E-02	18	6.4E+07 +/- 5.8E+07	0.00038 +/- 0.00034	5.90E-12	Orientation
ar_diff	0.00000	0.00009	5.77E-01	19	7.9E-04 +/- 2.8E-03	0.00010 +/- 0.00036	1.30E-01	Geometric
ma_sum	0.00000	0.00082	8.87E-02	19	3.5E-04 +/- 4.1E-04	0.00033 +/- 0.00038	9.37E-01	Geometric
m_sum	0.00000	0.00003	7.45E-01	19	-1.4E-03 +/- 8.5E-03	-0.00004 +/- 0.00025	2.91E-02	Orientation
m_diff	0.00000	0.00086	8.27E-02	19	9.7E-03 +/- 1.1E-02	0.00018 +/- 0.00020	1.86E-02	Orientation
M_diff	0.00000	0.00090	7.44E-02	19	-8.3E-04 +/- 9.1E-04	-0.00035 +/- 0.00038	4.19E-01	Orientation
mp_m	0.00000	0.00003	7.53E-01	19	-2.7E-03 +/- 1.7E-02	-0.00004 +/- 0.00024	1.47E-02	Orientation
rbv_m	0.00000	0.00053	1.74E-01	19	6.6E+06 +/- 9.5E+06	0.00012 +/- 0.00017	1.80E-11	Orientation

Table 5-4: Additional statistical parameters for the linear regressions fits to various TJ parameters.

Parameter	Impact on GND	R2	p-value of Correlation	Parameter Rank	Slope +/- 95% CI	Relative Slope +/- 95% CI	Interquartile Range	Parameter Type
gs_sum	0.00294	0.06695	3.20E-50	1	9.1E-05 +/- 1.2E-05	0.00338 +/- 0.00044	3.71E+01	Geometric
gs_diff	0.00282	0.06575	2.54E-49	2	1.6E-04 +/- 2.0E-05	0.00325 +/- 0.00042	2.09E+01	Geometric
N_m	0.00216	0.04317	1.31E-32	3	-8.0E-02 +/- 1.3E-02	-0.00258 +/- 0.00042	3.24E-02	Orientation
mp_avg	0.00198	0.02665	1.36E-20	4	3.7E-01 +/- 7.7E-02	0.00250 +/- 0.00052	6.81E-03	Orientation
N_avg	0.00197	0.04519	4.31E-34	5	-1.4E-01 +/- 2.3E-02	-0.00234 +/- 0.00037	1.66E-02	Orientation
delta_g	0.00195	0.04248	4.16E-32	6	2.2E-04 +/- 3.7E-05	0.00234 +/- 0.00038	1.04E+01	Orientation
M_sum	0.00169	0.02523	1.45E-19	7	3.8E-03 +/- 8.3E-04	0.00216 +/- 0.00046	5.63E-01	Orientation
rbv_3	0.00157	0.02431	6.66E-19	8	3.4E+07 +/- 7.4E+06	0.00201 +/- 0.00044	5.97E-11	Orientation
N_3	0.00151	0.02380	1.55E-18	9	-2.4E-02 +/- 5.2E-03	-0.00194 +/- 0.00043	8.20E-02	Orientation
lambda	0.00092	0.01897	4.74E-15	10	-6.6E-04 +/- 1.7E-04	-0.00123 +/- 0.00031	1.85E+00	Orientation
M_diff	0.00082	0.00758	7.89E-07	11	-4.3E-03 +/- 1.7E-03	-0.00136 +/- 0.00054	3.14E-01	Orientation
N_1	0.00057	0.00540	3.09E-05	12	-8.6E-03 +/- 4.0E-03	-0.00108 +/- 0.00051	1.26E-01	Orientation
ar_sum	0.00044	0.00457	1.28E-04	13	5.1E-03 +/- 2.6E-03	0.00089 +/- 0.00046	1.73E-01	Geometric
rbv_1	0.00042	0.00400	3.37E-04	14	1.3E+07 +/- 7.2E+06	0.00093 +/- 0.00051	7.03E-11	Orientation
ma_diff	0.00029	0.00284	2.52E-03	15	2.3E-03 +/- 1.5E-03	0.00082 +/- 0.00053	3.53E-01	Geometric
mp_3	0.00025	0.00347	8.49E-04	16	-5.6E-03 +/- 3.3E-03	-0.00060 +/- 0.00035	1.06E-01	Orientation
gb_1_2_3_trace_angle	0.00011	0.00188	1.40E-02	17	2.2E-03 +/- 1.8E-03	0.00054 +/- 0.00043	2.42E-01	Geometric
ma_sum	0.00000	0.00115	5.49E-02	18	6.3E-04 +/- 6.4E-04	0.00047 +/- 0.00048	7.49E-01	Geometric
ar_diff	0.00000	0.00038	2.72E-01	18	-2.8E-03 +/- 4.9E-03	-0.00026 +/- 0.00046	9.33E-02	Geometric
mp_1	0.00000	0.00113	5.66E-02	18	-3.2E-03 +/- 3.3E-03	-0.00051 +/- 0.00052	1.56E-01	Orientation
rbv_avg	0.00000	0.00109	6.13E-02	18	1.1E+08 +/- 1.1E+08	0.00042 +/- 0.00044	3.82E-12	Orientation
mp_m	0.00000	0.00090	8.89E-02	18	2.6E-02 +/- 3.0E-02	0.00030 +/- 0.00035	1.16E-02	Orientation
rbv_m	0.00000	0.00053	1.93E-01	18	-1.3E+07 +/- 1.9E+07	-0.00021 +/- 0.00032	1.67E-11	Orientation
m_diff	0.00000	0.00007	6.36E-01	18	4.5E-03 +/- 1.9E-02	0.00007 +/- 0.00031	1.67E-02	Orientation
m_sum	0.00000	0.00000	9.80E-01	18	-1.7E-04 +/- 1.4E-02	0.00000 +/- 0.00037	2.71E-02	Orientation